

**Universitätsklinikum Tübingen**  
**Abteilung für Diagnostische und Interventionelle Radiologie**  
**Sektion für Experimentelle Radiologie**

**Assessment of morphological and functional properties  
of the genitourinary system using high resolution MRI**

Inaugural-Dissertation  
zur Erlangung des Doktorgrades  
der Humanwissenschaften

der Medizinischen Fakultät  
der Eberhard Karls Universität  
zu Tübingen

vorgelegt von

Paar geb. Will, Susanne Adelgunde Monica

2016

Dekan: Professor Dr. I. B. Autenrieth

1. Berichterstatter: Professor Dr. Dr. F. Schick

2. Berichterstatter: Professor Dr. K. Scheffler

Tag der Disputation: 04.11.2016





## Contents

List of Abbreviations .....	3
List of Symbols.....	4
1 Introduction .....	5
2 Basic Principles .....	9
2.1 Magnetic Resonance Imaging.....	9
2.1.1 Spin.....	9
2.1.2 Nuclear Magnetic Resonance .....	11
2.1.3 Longitudinal and Transverse Relaxation.....	13
2.1.4 Spatial Encoding.....	17
2.1.5 MR Sequences .....	20
2.1.6 Diffusion Imaging .....	25
2.2 Post Processing Algorithms .....	28
2.2.1 Image Registration.....	28
2.2.2 Image Segmentation .....	30
2.2.3 Distortion Correction.....	33
3 Material and Methods.....	35
3.1 Genitourinary Tract.....	37
3.1.1 Kidneys.....	37
3.1.2 Bladder and Sphincter .....	38
3.2 Visualization of Urethral Sphincter .....	40
3.2.1 MRI Acquisition.....	40
3.2.2 Histological Preparation .....	43
3.3 Segmentation of the Internal Renal Structures .....	45
3.3.1 MRI Acquisition.....	45
3.3.2 Image Registration.....	46
3.3.3 Automatic Segmentation Algorithm.....	47
3.3.4 Evaluation.....	51
3.4 Characterization of Distortion Corrected Images from DTI.....	53
3.4.1 MRI Acquisition.....	53
3.4.2 Registration and Segmentation.....	55
3.4.3 Distortion Correction.....	56

3.4.4	Image Analysis .....	58
3.4.1	Multiband Technique.....	59
4	Results .....	61
4.1	Visualization of Urethral Sphincter .....	61
4.2	Segmentation of the Internal Renal Structures .....	64
4.3	Characterization of Distortion Corrected Images from DTI.....	72
5	Discussion.....	79
5.1	Visualization of Urethral Sphincter .....	79
5.2	Segmentation of the Internal Renal Structures .....	82
5.3	Characterization of Distortion Corrected Images from DTI.....	86
6	Outlook and Future Work.....	89
7	Abstract.....	93
8	Zusammenfassung .....	95
9	References .....	97
	Erklärung zum Eigenanteil .....	104
	List of Publications .....	105
	Danksagung .....	107

## List of Abbreviations

2D	Two-Dimensional
ADC	Apparent Diffusion Coefficient
BW	Bandwidth
BMI	Body Mass Index
CNR	Contrast-to-Noise Ratio
CT	Computed Tomography
DAQ	Data Acquisition
DCE	Dynamic Contrast-Enhanced
DTI	Diffusion Tensor Imaging
DWI	Diffusion-Weighted Imaging
EPI	Echo Planar Imaging
FA	Fractional Anisotropy
FcM	Fuzzy c-Means algorithm
F>>H	Feet-Head
FID	Free-Induction Decay
FLASH	Fast Low Angle Shot
FoV	Field-of-View
FSE	Fast Spin Echo
Gd-DTPA	Gadolinium-Diethylene-Triamine Pentaacetic Acid
GRE	Gradient Echo
GUI	Graphical User Interface
HASTE	Half-Fourier Angle-shot Turbo Spin Echo
HD-UPP	High Definition Urethral Pressure Profile
HE	Hematoxylin-Eosin
H>>F	Head-Feet
kM	k-Means Algorithm
MB	Multiband
MD	Mean Diffusivity
MRI	Magnetic Resonance Imaging
MSC	Mesenchymal Stem Cells
NMR	Nuclear Magnetic Resonance
NSF	Nephrogenic Systemic Fibrosis
PB	Prussian Blue
ROI	Region Of Interest
R >> L	Right-Left
RF	Radio Frequency
RARE	Rapid Acquisition with Relaxation Enhancement
SE	Spin Echo
SNR	Signal-to-Noise Ratio
SPIO	Superparamagnetic Iron Oxide
SPM	Statistical Parametric Mapping
Voxel	Volume Element
T <sub>1</sub> -/ T <sub>2</sub> -w	T <sub>1</sub> - and T <sub>2</sub> -weighted

## List of Symbols

$\vec{I}$	Spin
$\hbar$	Reduced Planck's constant
$I$	Spin quantum number
$\vec{\mu}_m$	Magnetic moment
$\gamma$	Gyromagnetic ratio
$\vec{M}$	Magnetization vector
$\omega_0$	Larmor frequency
$B_0$	Magnetic field strength
$\Delta E$	Energy difference
$T$	Temperature
$k_B$	Boltzmann constant
$\Theta$	Flip angle
$M_z$	Longitudinal magnetization
$M_{xy}$	Transverse magnetization
$T_R$	Repetition time
$T_E$	Echo time
$T_1, T_2$	Relaxation times
$\Delta\omega$	Bandwidth
$G_x$	Frequency encoding/ readout gradient
$G_y$	Phase encoding gradient
$G_z$	Slice selective gradient
$r$	Location
$t$	Time
$\eta$	Viscosity
$R_H$	Hydrodynamic radius
$S/S_0$	Signal attenuation
$D$	Diffusion coefficient
$\lambda_1, \lambda_2, \lambda_3$	Eigenvalues
$\vec{e}_1, \vec{e}_2, \vec{e}_3$	Eigenvectors
$u(x)$	Displacement
$I_M(x+u(x))$	Moving image
$I_R(x)$	Reference image
$M_i$	Currently processed mask
$M_{i-1}$	Previous mask
$ve$	Volume error
$oe$	Overlap error
$V_M / V_A$	Manually and automatically segmented volume
$vo$	Volume overlap/ Jaccard index
$dice$	Dice's coefficient
$R^2$	Determination coefficient

## 1 Introduction

The genitourinary tract plays a functional role in the human body. The blood is filtered inside the kidneys and necessary substances as electrolytes, sugars or water are returned to the body. The resulting urine is then diverted out of the body through the bladder. This process is controlled through the urethral sphincter. Meaningful examinations of the different compartments of the genitourinary tract are obligatory for reliable diagnosis of diseases.

Age related stress incontinence is partially related to a loss of muscular function. The direct replacement of the muscular cells by implantation of stem cells represents a possible therapeutic attempt, which has been proven to be an effective concept [1]. In order to improve the physiological function of the urethral sphincter, different aspects of cell-based treatments have been investigated in literature [2,3]. A detailed overview of the cell behavior in vivo is essential to understand the biological processes and is important for the development of novel cell-based therapies. In the context of sphincter regeneration, the stem cells have to be applied in a small anatomic region. This requires an in vivo imaging method which is robust and sensitive alike, while allowing anatomical correlation. These features are essentially fulfilled by imaging labeled stem cells using Magnetic Resonance Imaging (MRI).

Another important part for the genitourinary system is the kidney. Automatic classification of anatomical renal structures and quantitative assessment of their MR properties are considered to be crucial for early detection and monitoring of renal diseases such as glomerular nephritis or hydronephrosis [4]. Furthermore, the segmentation of the internal renal structures cortex, medulla, and pelvis are applicable for functional and morphological assessments. It is known, that the renal cortex volume tends to decrease over time in chronically injured kidneys. The precise measurement of the cortical volume and additional functional analysis could be helpful biomarkers for follow-up examinations in patients with chronic kidney diseases or transplanted kidneys [5].

The three most common imaging modalities used for volumetric analysis are ultrasound, computed tomography (CT) and MRI. Techniques like dual-energy CT show especially valuable results in renal oncologic imaging [6-9]. For follow-up examinations in benign renal diseases the considerable radiation exposure should always be taken into account. Therefore, a simple estimation of the kidney volume is obtained by renal length measurements using ultrasound. However, this method has shown a tendency to underestimate the renal volume [10,11]. MRI provides spatially highly resolved anatomical images and therefore represents a more precise imaging modality for volumetric measurements. Automatic volumetry and assessment of functional properties require reliable segmentation of the tissue types of interest. Segmentation is performed using either native or contrast enhanced MR images [12,13]. In the last years, dynamic contrast-enhanced measurements (DCE-MRI) [14-16] e.g. using Gadolinium-Diethylene-Triamine Pentaacetic Acid (Gd-DTPA) have been used for the quantification of renal volume. The use of contrast agent leads to a considerable contrast between renal cortex and medulla within the first minutes after injection. In vivo measurements in animals [17] and humans [18, 19] have demonstrated a good differentiation between the entire kidneys and surrounding tissue. Even if the contrast agent helps to improve the contrast behavior between the renal compartments, a reliable segmentation still needs at least two images recorded in different perfusion phases [14]. A well-known drawback of using contrast agent – especially in patients with kidney insufficiency – is its tendency to cause nephrotoxic effects or even nephrogenic systemic fibrosis (NSF) [20].

For this reason, an approach working without application of contrast agent is preferred. The main problem is MRI datasets acquired without contrast agent [19, 21, 22] usually result in a limited contrast between the inner structures of the kidneys as well as to surrounding tissue. Thus, the potential and accuracy of non-contrast enhanced MRI measurements in the context of an automatic renal segmentation has to be proven. A precise determination of the entire volume of internal organs is rarely executed in clinical practice, as manual segmentation over a large number of slices is very time consuming. Automatic segmentation algorithms with different methods like thresholding [17], clustering [23, 24], region growing [25] and contour detection [26,27] or their combinations are preferred for this task.

For separation of the internal renal structures (cortex, medulla and pelvis), MR techniques providing a sufficient contrast between these compartments are required. Further, the identification of the entire kidneys needs MR images which offer a high contrast between kidneys and surrounding tissue (liver, spleen, gastrointestinal tract). In clinical routine, abdominal imaging typically comprises two-dimensional (2D) T<sub>1</sub>- and T<sub>2</sub>-weighted (T<sub>1</sub>-/T<sub>2</sub>-w) sequences.

Besides morphological imaging, examination of functional parameters is an essential part for the evaluation of organs. Functional MRI using diffusion [28, 29], perfusion [19] and blood oxygen level-dependent techniques [15, 17, 23] has been proven to be useful analyzing tools for abdominal examination. Diffusion-weighted imaging (DWI) and diffusion tensor imaging (DTI) have been applied successfully in the past for tissue characterization and lesion detection [25, 24]. Especially, DTI has already proven its capabilities for analysis of renal composition and function [27]. However, internal renal structures as medulla and cortex are not easily to differentiate in both, diffusion-weighted images and calculated parameter maps. For this reason a transfer of segmented areas from high-resolution morphological images [26], with suitable visualization of the anatomy, to DTI images would be helpful.

Due to inevitable geometric distortions in echo-planar DTI, a direct transfer of the segmented areas in high quality anatomical images to functional imaging is not adequate. Acquiring datasets in different breath-hold scans lead to displacements of the kidneys and the resulting breathing related artifacts have to be compensated. Further artifacts are relevant for measurements in the kidneys compared to examinations of the brain (where DWI is used for assessment of ischemic areas and DTI for fiber tracking), since static field inhomogeneities caused by susceptibility effects of tissues and surrounding air are more pronounced in the abdomen. In addition, distortions are also caused by eddy currents. Distortion correction methods like magnetic field mapping [30], non-linear registration [31] or reversal phase encoding approaches [32, 33], mostly applied in brain studies, have been suggested to remove these artifacts.

The basics of MR imaging and the commonly used sequences with their applications are briefly described at first in this thesis. Afterwards, the image post-processing methods, which have been used in this work, are presented in two subsections.

The *Material and Methods* section starts with an overview of the anatomy of the urogenital tract and focuses on the kidney and the urethral sphincter. The main sections include three parts, where the optimization of sequence parameters to represent the thin structure of the urethral sphincter in an animal model is shown in the first part. High-resolution datasets illustrate the anatomy of the urethra as well as the localization of the injected stem cells.

Further optimization of image contrast in human abdominal datasets regarding the delineation of the kidney from surrounding tissue and the classification of the internal renal structures are presented in the second part. The subsequent automatic segmentation algorithm is based on these non-contrast enhanced images. The developed algorithm is executed on images acquired at field strengths of 1.5T and 3T.

The third part describes a fusion of the segmented areas with functional datasets. Therefore a distortion correction algorithm for abdominal echo planar diffusion-weighted images was developed and evaluated.

The description of further potential of the presented algorithms regarding future application in clinic will finalize this thesis.

## 2 Basic Principles

### 2.1 Magnetic Resonance Imaging

Magnetic resonance imaging (MRI) is a non-invasive technique that enables visualization of anatomical structures and organs with an excellent soft tissue contrast as well as investigation of functional parameters of tissues without using ionizing radiation.

The following chapter introduces the physical principle of nuclear magnetic resonance (NMR). The basics of MR are described by two physical theories, quantum mechanics and classical electrodynamics. First, the property of the spin is explained by the quantum-mechanical considerations. Second, the behavior of the magnetization within a sample inside the MR tomography will be explained using the classical description. Finally, image acquisition techniques including contrast generation and spatial encoding are outlined.

#### 2.1.1 Spin

MRI had its beginning in 1973 with the first attempts of Lauterbur [34] and Mansfield [35], based on the work of NMR pioneers Bloch [36] and Purcell [37] 1946 (Nobel prize in physics in 1952). Nuclear magnetic resonance is based on the fact that atomic nuclei possessing a mechanical angular momentum  $I$  (spin), also possess a magnetic momentum  $\mu$ . A strong external magnetic field aligns the spin in parallel or antiparallel orientation. Due to its abundant occurrence in biological tissue, the  $^1\text{H}$  nucleus is the commonly used nucleus in clinical MRI. The particles are divided in fermions ( $\vec{I}=1/2$ ; electron, proton and neutron) and bosons ( $\vec{I}=1$ ; photon). The spin  $\vec{I}$  depends on the nuclear spin quantum number  $I$  and the reduced Planck's constant  $\hbar$  ( $1.055 \cdot 10^{-34}$  Js)

$$\vec{I} = \sqrt{I(I+1)} \hbar \quad (2.1)$$

$$\hbar = h/2\pi \quad (2.2)$$

where  $h$  is Planck's constant ( $6.626 \cdot 10^{-34}$  Js) .

The atomic nuclei give rise to a magnetic moment  $\vec{\mu}_m$  parallel to the spin  $\vec{I}$  which is given by

$$\vec{\mu}_m = \gamma \vec{I} \quad (2.3)$$

where  $\gamma$  is the gyromagnetic ratio ( $2.68 \cdot 10^8$  rad s<sup>-1</sup>T<sup>-1</sup> for <sup>1</sup>H protons, corresponding to 42.6 MHz/T) which depends on the studied nucleus [38-40].

The atoms with effective nuclear spin visible in MRI have an odd number of protons and/or neutrons. Further common atomic nuclei used in magnetic resonance are <sup>13</sup>C, <sup>19</sup>F, <sup>23</sup>Na and <sup>31</sup>P. The gyromagnetic ratio, the nuclear magnetic resonance frequency or Larmor frequency, and the natural occurrence of the atomic nuclei are represented in Table 1.

Without external applied magnetic field the spins of the hydrogen nuclei are arranged randomly inside a sample, thus the sum of all magnetic moments ( $\vec{M}$ ) on average is zero.

**Table 1:** Most commonly used nuclei for NMR [31]. The highest relative sensitivity and highest natural occurrence results for <sup>1</sup>H, which is the reason for hydrogen nuclei being most commonly used in MR imaging.

Isotop	Spin	Gyromagnetic ratio [10 <sup>7</sup> rad T <sup>-1</sup> s <sup>-1</sup> ]	NMR frequency for 1T [MHz]	Natural occurrence [%]
<sup>1</sup> H	1/2	26.76	42.58	99.985
<sup>2</sup> H	1	4.11	6.54	0.015
<sup>3</sup> He	1/2	-20.38	32.43	1.4 · 10 <sup>-4</sup>
<sup>7</sup> Li	3/2	10.40	16.55	92.580
<sup>13</sup> C	1/2	6.73	10.71	1.108
<sup>14</sup> N	1	1.93	3.08	99.630
<sup>15</sup> N	1/2	-2.71	4.32	0.370
<sup>17</sup> O	5/2	-3.63	5.77	0.037
<sup>19</sup> F	1/2	25.17	40.05	100.000
<sup>23</sup> Na	3/2	7.08	11.27	100.000
<sup>31</sup> P	1/2	10.83	17.24	100.000
<sup>129</sup> Xe	1/2	-7.40	11.78	26.440

Since the spins represent microscopic magnets, an externally applied field  $B_0$  aligns the nuclei either parallel (lower energy) or anti-parallel (higher energy) to the external field.

As the orientation parallel to  $B_0$  is energetically favorable, there is a slight surplus of parallel spins (about 5 out of 1.000.000 at 1.5T), resulting in a measurable so called macroscopic magnetization.

The relative distribution of the spins, which are oriented parallel ( $N_p$ ) and antiparallel ( $N_a$ ) to the field, depends on the energy difference  $\Delta E$  and the absolute temperature  $T$ . In thermal equilibrium, the distribution is given by Boltzmann statistics

$$\frac{N_p}{N_a} = e^{\Delta E / (k_B T)} \quad (2.4)$$

where  $k_B$  represents the Boltzmann constant ( $1.38 \cdot 10^{-23} \text{ JK}^{-1}$ ). Theoretically by an increase of the applied magnetic field  $B_0$  and a decrease of the temperature, the ratio  $N_p/N_a$  is increased. However, practically a change of the temperature during in vivo imaging is not feasible [39].

The energy difference between the two split levels is proportional to the external magnetic field.

$$\Delta E = \hbar \omega = \gamma \hbar B_0 \quad (2.5)$$

The precession movement  $\omega$  results from the interplay between external magnetic field  $B_0$ , the magnetic moment  $\mu$  of the nuclear spins and the intrinsic angular momentum  $I$  of the atomic nucleus. This movement is comparable to a spinning top and is called precession. The magnetic moment vector for a spin rotates with the same frequency, the Larmor frequency  $\omega_0$ , which is described by the following equation

$$\omega_0 = \gamma B_0 \quad (2.6)$$

The Larmor frequency is the characteristic resonance frequency of the spins which depends on the strength of the external magnetic field  $B_0$  and the gyromagnetic ratio  $\gamma$ , depending on the nuclei.

### 2.1.2 Nuclear Magnetic Resonance

For imaging of a macroscopic body a classical description is used. Not the individual atomic nucleus has to be considered, but rather the net magnetization vector  $\vec{M}$  of the spins is observed corresponding to the sum of all magnetic moments of identical nuclei within a certain volume [39]. If the direction of the magnetization vector is not in accordance with the one of the external magnetic field a torque acts on the vector. The existing vector reacts with a precession movement (see Figure 1), leading to a rotation of the angular momentum around the direction of the applied magnetic field  $B_0$  (here in z-direction).

In the presence of an external static magnetic field and a Radio Frequency (RF) electromagnetic field, the transition between the two energy states is achieved by equation 2.5. The Larmor frequency is calculated for a given nucleus. For example, the spins of hydrogen protons precess at field strength of 3Tesla with a Larmor frequency of about 128 MHz.

To flip the magnetization vector  $\vec{M}$  aligned along the z axis into the xy plane, a circularly polarized RF field  $\vec{B}_1$  is applied. Here, the resonance principle is used, i.e. the RF excitation occurs with a frequency equal to the spin precession (Larmor) frequency. The flip angle  $\theta$  is determined by the amplitude of the RF pulse, the pulse duration and the gyromagnetic ratio.

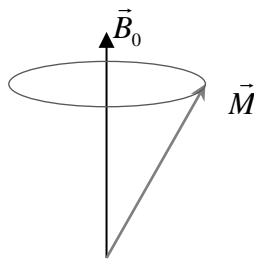


**Figure 1:** Precession of the magnetization vector  $\vec{M}$  around the direction of the external magnetic field  $B_0$  with the Larmor frequency  $\omega_0$ .

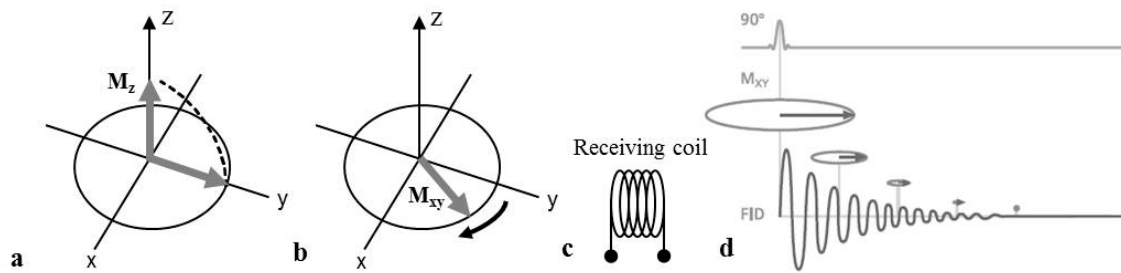


**Figure 2:** (a) Net magnetization  $M_z$  is flipped by the flip angle  $\theta$ . (b) In the transverse plane the magnetization vector  $M_{xy}$  precesses with the Larmor frequency and induces an electrical voltage. This signal is detectable in MRI using a receiving coil (c) and illustrated as free induction decay (FID) (d).

The flip angle  $\theta$  is an important parameter of the excitation process as it determines the amount of longitudinal magnetization  $M_z$  which is flipped into the transverse plane and thus  $M_{xy}$  (see Figure 2a).

Since the measured MR signal is proportional to  $|M_{xy}|$ , a RF pulse with flip angle of  $90^\circ$  causes the strongest MR signal. After RF irradiation the magnetization vector precesses with the Larmor frequency in the  $xy$ -plane and induces an electrical voltage, which can be measured using a receiving coil. This voltage signal decreases exponentially over time and is called free induction decay (FID; see Figure 2d). After full relaxation the net magnetization reaches the equilibrium state.

### 2.1.3 Longitudinal and Transverse Relaxation

In MR the term relaxation describes the process of the magnetization recovery back to the equilibrium state after RF excitation. This phenomenon is based on two types of physical processes: the spin-lattice interaction causes so called longitudinal relaxation (also known as spin-lattice relaxation) and the spin-spin interaction is the origin for dephasing of transverse relaxation (or spin-spin relaxation). These processes are running with different relaxation time constants and determine the relaxation behavior of the longitudinal and transverse magnetization components  $M_z$  and  $M_{xy}$ . The large difference between relaxation times of different tissues is the main reason for the image contrast in MRI.

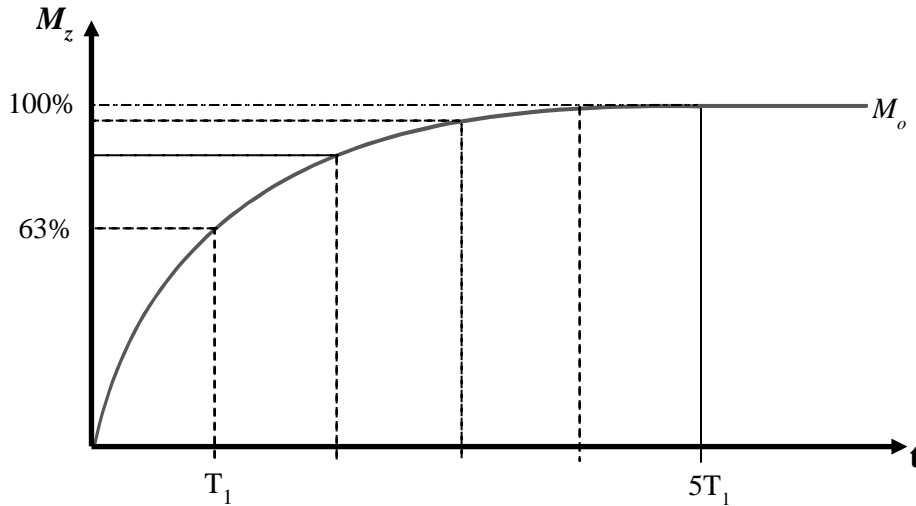


**Figure 3:** Longitudinal magnetization  $M_z$  after RF excitation with flip angle of  $90^\circ$ . After the time  $T_1$  about 63% of the original magnetization  $M_0$  is recovered and after  $5T_1$  nearly 100% are restored.

#### *Longitudinal relaxation*

After the RF pulse is turned off, the spins or rather the entire spin system return from a higher into a lower energetic state. This process is referred as spin-lattice relaxation because the spins give the absorbed energy back to their environment (lattice).

Similarly, the net magnetization  $M$  returns back to the ground state  $M_0$  (see Figure 3). The longitudinal magnetization  $M_z$  at the time  $t$  after an excitation RF pulse with flip angle of  $90^\circ$  is described by the formula:

$$M_z(t) = M_0 \left(1 - e^{-\frac{t}{T_1}}\right) \quad (2.7)$$

$M_0$  is the initial magnetization or the ground state of the magnetization [41].  $T_1$  describes the time where about 63% of the original magnetization is recovered and is termed: longitudinal relaxation time.

#### *Transverse relaxation*

Immediately after a RF excitation pulse, all spins precess coherently with the same Larmor frequency. This condition is not stable for an extended period of time, since the spins lose their phase coherence due to local interaction between their magnetic moments. The decoherence of the spins causes the decay of transverse magnetization and this process is called spin-spin relaxation. The time course of transverse magnetization is described by the following equation

$$M_{xy}(t) = M_0 \cdot e^{-\frac{t}{T_2}} \quad (2.8)$$

$T_2$  describes the time where the transverse magnetization vector decreases to 37% of its original magnitude. An additional reason for the loss of phase coherence between the spins enclosed in a finite volume is the magnetic field inhomogeneity. The spins at different locations precess with different frequencies, leading to a dispersion of the phase angles. The superposition of both effects results in a faster decay of transverse magnetization and is described by a time constant  $T_2^*$  [41]

$$\frac{1}{T_2^*} = \frac{1}{T_2} + \frac{1}{T_2'} \quad (2.9)$$

The loss of transverse magnetization due to magnetic field inhomogeneity  $T_2'$  is recoverable, whereas the intrinsic  $T_2$  losses are not recoverable because they are caused by local, random field variations. Each tissue type has diverse  $T_1$  and  $T_2$  relaxation times (see Table 2). Different weightings generate variable image contrasts in MRI.

**Table 2:**  $T_1$ - and  $T_2$ - times for some important tissues at 1.5T. [33, 34]

<b>Tissue</b>	<b><math>T_1</math> [ms]</b>	<b><math>T_2</math> [ms]</b>
Grey matter	950	100
White matter	600	80
Cerebrospinal fluid	4500	2200
Muscle	900	50
Adipose tissue	250	60
Blood	1200	100-200
Renal cortex	1060	70
Renal medulla	1400	75

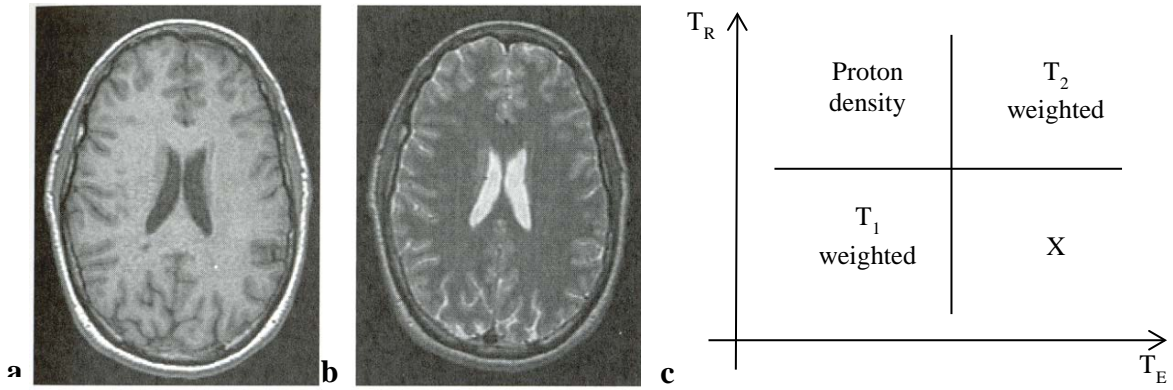


**Figure 4:** An axial image of a human brain with (a) T<sub>1</sub>- and (b) T<sub>2</sub>-weighted contrast. The diagram (c) shows the influence of T<sub>R</sub> and T<sub>E</sub> to obtain images with different contrast. [4]

Figure 4 shows the differences between T<sub>1</sub>- and T<sub>2</sub>- weighted images; while in T<sub>1</sub>-weighted images fluid appears as hypo intense regions, in T<sub>2</sub>-weighted images fluid regions such as CSF are shown as bright areas. The relation between the different relaxation times for biological tissues is usually T<sub>2</sub>' < T<sub>2</sub> < T<sub>1</sub>.

*Bloch equations*

The mathematical characterization of the NMR phenomenon is provided by Felix Bloch and summarized in the empirical vector equation referred as the Bloch equations [42]

$$\frac{dM_x}{dt} = \gamma(M_y B_0 + M_z B_1 \sin(\omega t)) - \frac{M_x}{T_2} \quad (2.10)$$

$$\frac{dM_y}{dt} = \gamma(M_z B_1 \cos(\omega t) - M_x B_0) - \frac{M_y}{T_2} \quad (2.11)$$

$$\frac{dM_z}{dt} = -\gamma(M_x B_1 \sin(\omega t) + M_y B_1 \cos(\omega t)) - \frac{M_z - M_0}{T_1} \quad (2.12)$$

These equations are the fundamental base for the description of magnetization precession in the presence of a RF pulse (with amplitude B<sub>1</sub> and frequency ω) and relaxation processes.

The complete set of solutions for the Bloch equation in absence of the RF field  $B_1$  is rewritten in the rotating frame as

$$M_x(t) = (M_x(0)\cos(\Delta\omega t) + M_y(0)\sin(\Delta\omega t))e^{-t/T_2} \quad (2.13)$$

$$M_y(t) = (M_y(0)\cos(\Delta\omega t) - M_x(0)\sin(\Delta\omega t))e^{-t/T_2} \quad (2.14)$$

$$M_z(t) = M_z(0)e^{-t/T_1} + M_0(1 - e^{-t/T_1}) \quad (2.15)$$

where  $\Delta\omega$  is the offset frequency between RF frequency and Larmor frequency.

### 2.1.4 Spatial Encoding

In MRI, macroscopic volumes are excited and the signal is measured by receiving coils. To obtain the signal contribution, gradient fields have to be applied during certain time intervals in an imaging sequence. Gradient fields are small, temporally and spatially variable magnetic fields superimposed to the static magnetic field  $B_0$  (see Figure 5). They provide a spatial variation of the magnetic field's  $B_x$ -,  $B_y$ - and  $B_z$ -component. For the subsequent sections the following relation between the two coordinate systems, the logical and the physical coordinate system, is used:

Frequency encoding direction	≡	x-axis
Phase encoding direction	≡	y-axis
Slice selection direction	≡	z-axis

The signal contribution from a single voxel can be calculated, if the data acquisition technique is known.

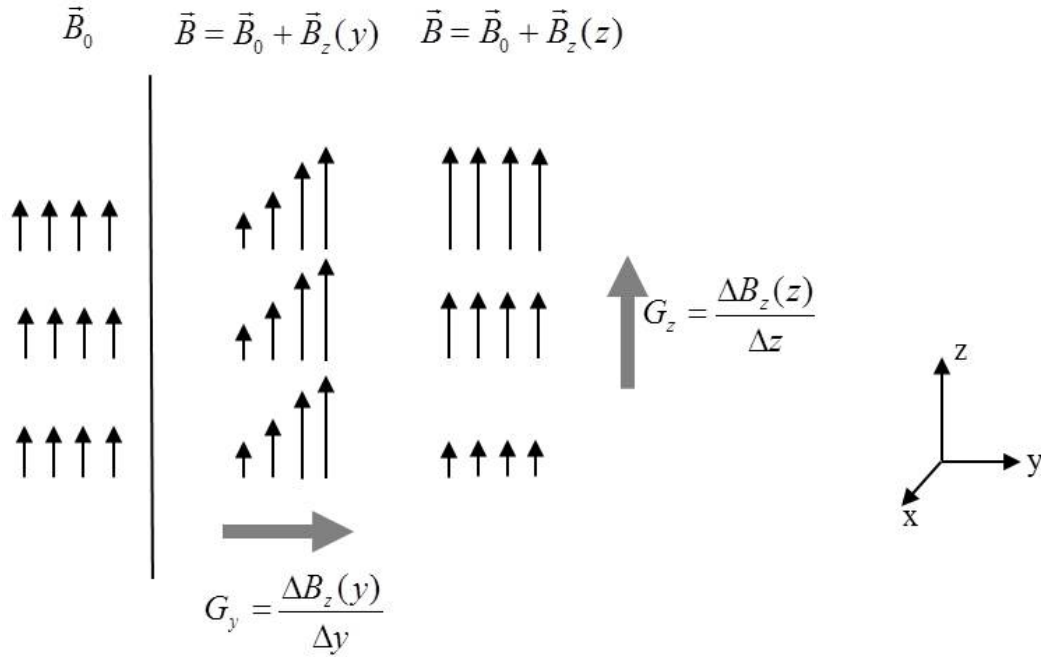


**Figure 5:** Static magnetic field  $B_0$  and the gradients  $G_y$  and  $G_z$ , representing the magnetic field shift parallel to the y- and z-axis.

The signal reception is divided into two steps. First, a particular slice is selected from the entire volume applying an excitation pulse in the presence of an appropriate gradient in slice direction. Then a two dimensional coding scheme is chosen within a slice to determine the spatial distribution of the transverse magnetization. This process forms the basis of most MR pulse sequences.

According to equation 2.6, the spatially variable magnetic field causes the Larmor frequency to vary spatially:

$$\omega(r) = \gamma B_0 + \gamma G \cdot r = \omega_0 + \delta\omega(r) \quad (2.16)$$

The possibility to modify the Larmor frequency at a given location is a fundamental principle of spatial encoding in MRI.

Slice selection and the spatial encoding within the slice are based on the combination of gradient and RF fields. The concept of slice selection is the use of a RF pulse with a Larmor frequency  $\omega$  for selecting the position of the slice and the bandwidth  $\Delta\omega$  in combination with the gradient  $G_z$  specifies the slice thickness.

This concept ensures the excitation of the magnetization within the slice, but has in the ideal case no effect on the magnetization outside the slice. Therefore, the selected slice is characterized by its location and thickness.

For spatial encoding in the image plane, two orthogonal gradients are switched perpendicular to the slice selected direction. The frequency encoding technique applies a gradient in x-direction during signal acquisition, called the readout gradient  $G_x$ . Thus, a continuous frequency spectrum contributes to the MR signal where the frequency directly relates to the x-position of a spin ensemble.

The process of phase encoding uses a gradient between excitation RF pulse and signal acquisition. This gradient induces a change in frequency, leading to a spatial distribution of the phase between the spins. While frequency differences stop with the removal of the gradient, the phase differences remain. Phase encoding is used to resolve the second spatial direction (here y-direction) using the same principle as the frequency encoding process. To reconstruct the distribution of the magnetization along the x- and y-directions multiple measurements (repetitions) have to be performed.

### *k-Space*

The gradient modulated signals induced from magnetization precession are analyzed by trajectories in a 2D space, called k-space, corresponding to the Fourier transform of the spatial distribution of the magnetization [43, 44]. The name k-space originates from naming the time integrals of the gradient fields  $k$ . The k-space represents the MRI raw data of an image and is sampled in conventional MRI line by line. The simplest procedure is explained by a so called spin echo sequence (see section 2.1.5). A slice is selected after  $90^\circ$  RF pulse using the gradient  $G_z$ . At  $T_E/2$ , a  $180^\circ$  pulse is initiated to re-phase the spins. Between excitation and readout the phase encoding gradient  $G_y$  must be switched on. After the echo time  $T_E$  the signal is received and the readout gradient  $G_x$  is applied simultaneously. The signal is digitized and fills one line in k-space per phase encoding step. The required readout time is calculated from the sampling interval and the number of pixels in each row (resolution of the image in the x-direction). Each additional line is acquired by varying the phase encoding gradient  $G_y$  until the entire k-space is filled. Typically, the k-space has the same number of rows and columns as the final image. Using

a 2D-Fourier transformation, the acquired data are converted into its spatial equivalents. The result is a 2D matrix representing the MR image.

Near the center of k-space low spatial frequencies represent the signal intensity and contrast information of the image. High spatial frequencies in the peripheral regions of k-space contain the information of image resolution.

### 2.1.5 MR Sequences

Pulse sequences in MRI allow an adjustment of the image contrast using certain temporal series of RF and gradient pulses. In the last decades numerous imaging sequences were developed for different applications. Three important sequence types, which were used for the conducted experiments are described in more detail below[45].

#### *Spin echo and fast spin echo sequence*

The spin echo (SE) sequence is the most commonly used sequence in MRI. The pulse diagram in Figure 6 shows the interaction of RF pulse and the different gradients in a SE sequence. A  $90^\circ$  RF pulse turns the magnetization vector into the  $xy$  plane. Immediately after the spins started to precess at different frequencies ( $T_2'$  decay) they lose their phase coherence (dephasing effect). Hence the resulting total magnetization is reduced. However, the transverse magnetization is inverted by a refocusing RF pulse ( $180^\circ$  pulse) after the time  $T_E/2$ , leading to a rephasing effect which reaches its maximum at  $T_E$ . The data acquisition (DAQ) is performed after the echo time  $T_E$ , the time in between excitation and signal readout. The  $G_z$  gradient serves the slice selection, while the  $G_y$  gradient performs the phase encoding and  $G_x$  the frequency encoding. The rephasing of the spins generates the spin echo after the time  $T_E$ . For the fast spin echo (FSE) sequence this procedure is repeated several times with multiple  $180^\circ$  refocusing pulses (see Figure 7) [46].

Since the effective echo time  $T_E$  is extended, in the fast spin echo sequences the images are more  $T_2$ -weighted. The number of echoes, also called turbo factor, allows controlling of the  $T_2$ -weighting effect and indicates the number of recorded echoes after an excitation.

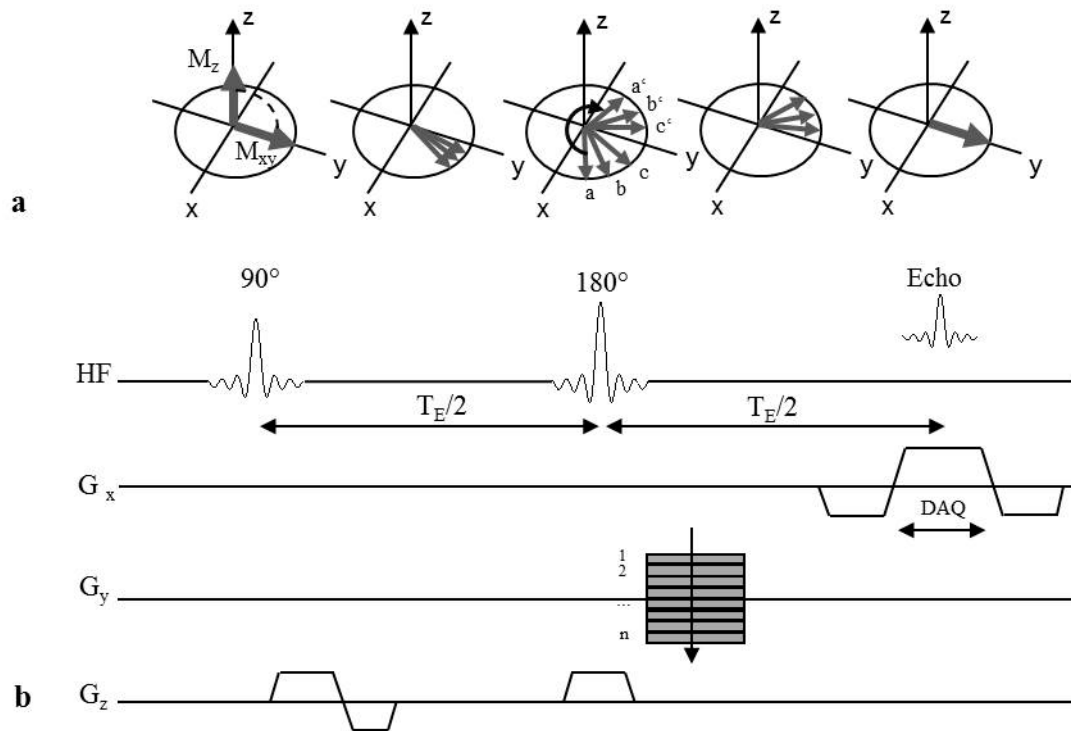


**Figure 6:** Schematic diagram (a) and the pulse diagram of a spin echo sequence (b): After a  $90^\circ$  RF pulse the net magnetization is flipped into the xy-plane and the spins start to dephase. The  $180^\circ$  refocusing pulses after  $T_E/2$  leads to a rephasing of the spin and therefore generates the spin echo after  $T_E$ . The slice selection ( $G_z$ ), the phase encoding ( $G_y$ ) and the frequency encoding ( $G_x$ ) gradients are illustrated.

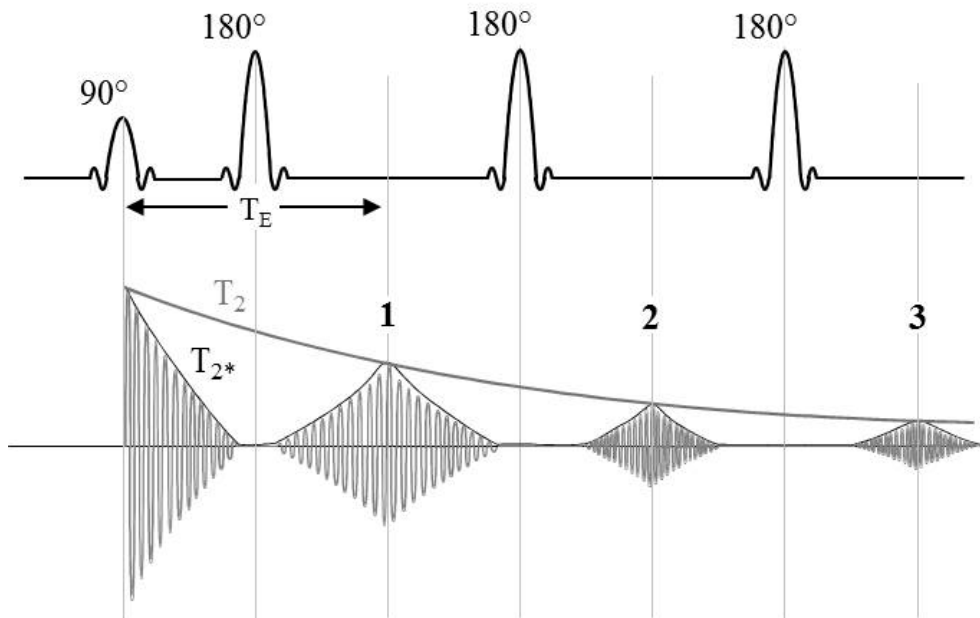


**Figure 7:** Fast spin echo (FSE) sequence with 3 echoes: Time response curve of a  $90^\circ$  RF pulse and three  $180^\circ$  refocusing pulses generating three echoes. The corresponding detected MR signal of the FSE sequence is presented.

*Gradient echo sequence*

The gradient echo sequence (GRE, gradient recalled/ refocused echoes) is often applied for fast image acquisition. In comparison to the previously described spin echo sequences the GRE pulse sequence doesn't use a  $180^\circ$  refocusing RF pulse to produce an echo. The reversal of a gradient is only used for the echo generation. A dephasing gradient with an opposite polarity is applied prior to the rephasing readout gradient. The rephasing and dephasing areas under the two gradient pulses, the so called gradient momentum, have to be equal to generate an echo signal (see Figure 8).

The GRE sequence forms the basis for very fast imaging techniques such as FLASH (Fast Low Angle Shot). A low excitation flip angle allows short repetition times ( $T_R < 10\text{ms}$ ) because the full  $T_1$  time isn't needed for the spins to return to their original orientation. A further important reason for the application of GRE sequences is a hyper intense signal of the flowing blood.

A favored application of this sequence is MR angiography without using contrast agent [47]. GRE sequences provide a relatively high SNR related to the used imaging time. SE sequences achieve a higher signal compared to GRE sequences because of the avoidance of the  $T_2'$  decay.

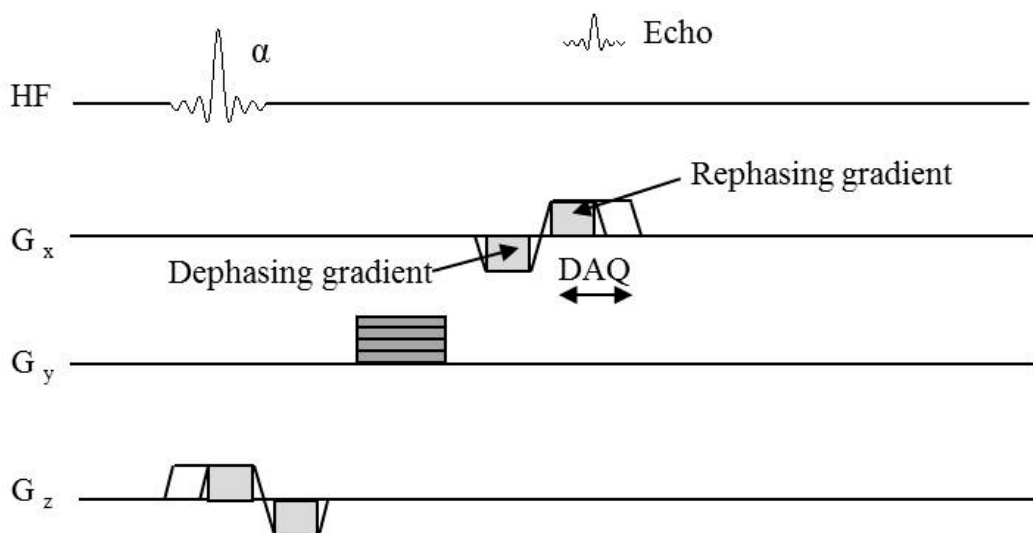


**Figure 8:** Pulse diagram of a gradient echo sequence: A dephasing gradient with an opposite polarity is applied in front of the rephasing readout gradient to generate the echo.

However, a longer  $T_{R/min}$  must be taken into consideration due to the introduced refocusing pulse in the SE sequence. Another advantage of GRE is its moderate level of the RF energy delivered to the patient, which is significantly higher in SE sequence with  $90^\circ$  and  $180^\circ$  RF pulse.

*Echo planar imaging*

Echo planar imaging (EPI) is an ultra-fast measurement method mainly used for functional MRI of the brain. With a reduced imaging time, motion artifacts are decreased making EPI a favorable imaging technique also for extracranial regions of the body such as heart and abdomen. Further important applications are diffusion and perfusion imaging. The EPI method acquires multiple lines of imaging data (k-space lines) after a single  $90^\circ$  and  $180^\circ$  RF excitation, instead of collecting only one line within each  $T_R$  period like the SE sequence. Normally the entire k-space is filled after one excitation. After  $180^\circ$  RF pulse, the frequency encoding gradient oscillates from a positive to a negative amplitude and, in combination with short phase encoding gradients (also called blips), creates several gradient echoes (see Figure 9). Each oscillation of the frequency encoding gradient corresponds to one line of imaging data in k-space, and each blip corresponds to a transition to the next k-space line [48].

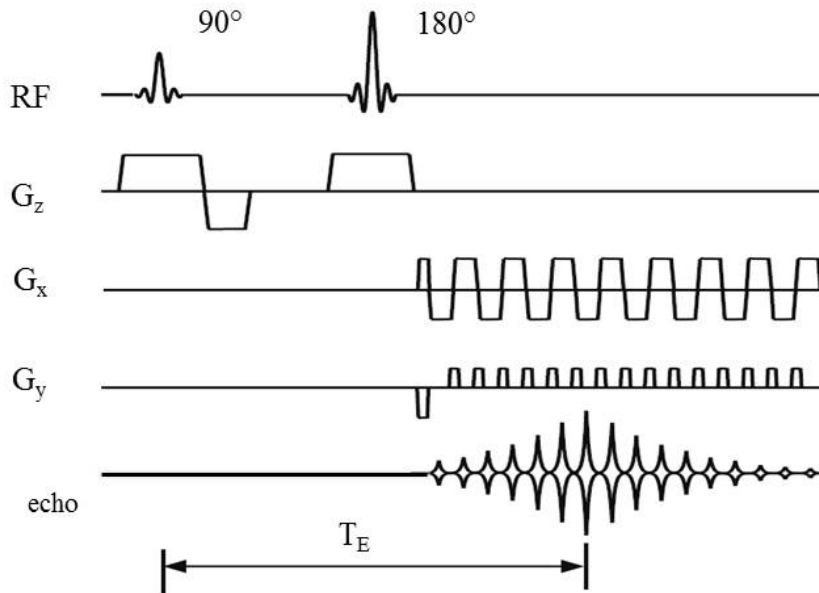


**Figure 9:** Pulse diagram of an echo-planar imaging (EPI) sequence with an oscillating frequency encoding gradient and several short phase encoding gradients (blips). One image is acquired with a single excitation. One image is acquired with a single excitation in the shortest possible time. Therefore, different EPI techniques are suitable for imaging of rapid physiologic processes in the

human body [49, 50]. However, the method has several disadvantages. It is very sensitive to susceptibility effects and inhomogeneities of the magnetic field leading to image artifacts and a decreased SNR. Additionally, the EPI images show strong geometric distortions which are mostly corrected by post processing algorithms.

### 2.1.6 Diffusion Imaging

Diffusion-weighted magnetic resonance imaging (DWI) is an imaging technique measuring diffusive motion also called the Brownian motion of water molecules in the body. The entire in vivo MR diffusion imaging approach is described in more detail in literature [51]. A common application of DWI technique is the diagnosis of stroke. Changes in the diffusion behavior of the brain tissue are also characteristic for some central nervous system diseases such as multiple sclerosis. The directional dependence of diffusion allows to determine the course of large nerve fiber bundles in white matter. There are different types of diffusion: The collective diffusion is the diffusion along a concentration gradient of several particles that are described by the Fick's law. The self-diffusion describes the diffusion of a single particle using the Einstein relation. Here, the movement direction of a single particle is completely random. Due to the interaction with other particles continuous direction changes occur.

The directional dependence of the self-diffusion is described by the following differential equation:

$$\frac{\partial P(r,t)}{\partial t} = \nabla \cdot (D \nabla P), \quad (2.17)$$

where  $P(r, t)$  is the probability density to find a particle at its specific location  $r$  with the corresponding time  $t$ . The (self) diffusion coefficient  $D$  as proportionality factor is described by

$$D = \frac{k_B T}{6\pi\eta R_H}, \quad (2.18)$$

where  $k_B$  is Boltzmann's constant,  $T$  the absolute temperature,  $\eta$  the viscosity and  $R_H$  the hydrodynamic radius.

However, the diffusion model for free diffusion is not applicable in vivo, because the molecular motion is restricted by cellular barriers. Therefore, an important parameter is the apparent diffusion coefficient (ADC), which depends on the direction as well as on the diffusion length.

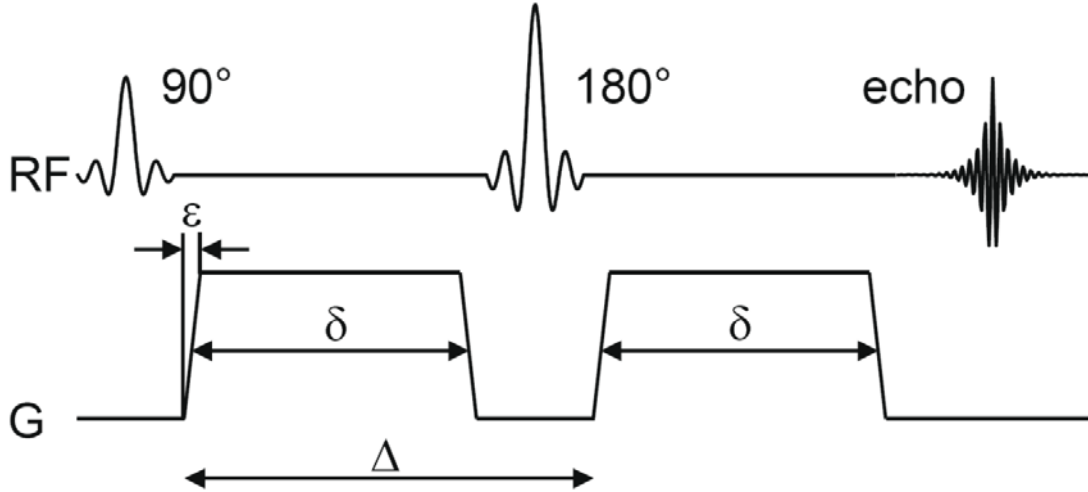


**Figure 10:** Pulse diagram of a spin echo sequence for diffusion-weighted imaging. Due to self-diffusion the transverse magnetization is not fully rephased after the 180° pulse leading to an attenuation of the signal. [52]

The ADC describes the self-diffusion of water or other molecules in biological tissue and their restriction by the tissue's microstructure.

The principle of diffusion measurement by MRI considers the phase changes during the simple bipolar pulse gradient. The phase of moving spins is not being rephased by this gradient pulse. The measured signal represents the mean value over a certain volume.

Signal attenuation  $S/S_0$  for DWI is given by

$$\frac{S(b)}{S_0} = e^{-bD}, \text{ where} \quad (2.19)$$

$$b = \gamma^2 G^2 \left[ \delta^2 \left( \Delta - \frac{1}{3} \delta \right) + \frac{1}{30} \epsilon^3 - \frac{1}{6} \delta \epsilon^2 \right] \quad (2.20)$$

is the so called *b-value*, including the parameters  $G$ ,  $\delta$ ,  $\epsilon$  and  $\Delta$  (shown in Figure 10). The diffusion coefficient  $D$  is calculated by several measurements with different *b-values* (at least two *b-values*).

Diffusion tensor imaging (DTI) is an imaging technique for detecting the directional dependence of the three-dimensional diffusion behavior. The diffusion coefficient in anisotropic media depends on the direction and is calculated as a diffusion tensor (3x3 matrix) in each volume element (voxel) using a modification of the Einstein equation given by:

$$\vec{r}^T \cdot \hat{D}^{-1} \vec{r} = 6\Delta t; \quad \hat{D} = \begin{pmatrix} D_{xx} & D_{xy} & D_{xz} \\ D_{yx} & D_{yy} & D_{yz} \\ D_{zx} & D_{zy} & D_{zz} \end{pmatrix} \quad (2.21)$$

The eigenvalues  $\lambda_1, \lambda_2, \lambda_3$  and the eigenvectors  $\vec{e}_1, \vec{e}_2, \vec{e}_3$  of  $\hat{D}$  define the principle directions of the ellipsoid and the corresponding equatorial radii  $A = \sqrt{6\lambda_1\Delta t}$ ,  $B = \sqrt{6\lambda_2\Delta t}$  and  $C = \sqrt{6\lambda_3\Delta t}$  consider the possible anisotropy of diffusion in vivo.

The mean diffusivity (*MD*) and the fractional anisotropy (*FA*) are calculated with respect to these values. The *FA* indicates the direction dependency of diffusion and allows a conclusion on the course of large nerve fibers. Within normal aging processes, a significant decrease of the *FA* value and an increase of the *MD* value is observed. Therefore, these values are also used as a biomarker for clinical diagnostic [53].

The resulting diffusion-weighted MRI measurements often show images of relatively insufficient quality and high noise levels, since diffusion manifests in a reduction of the measured signal. Higher spatial resolution with smaller volume elements generates correspondingly lower signal intensity. A large number of measurements is required and therefore time efficient measurement sequences such as echo planar imaging are the key factor for DWI.

## 2.2 Post Processing Algorithms

### 2.2.1 Image Registration

The following chapter will introduce the main image registration techniques used throughout this thesis. An overview of some registration methods is given in literature [54-56].

Image registration is an important part in digital image processing and brings two or more images/ sets of data in accordance. Registration is necessary when images are measured in different positions, at different time points or with different techniques. Hereby one of the images is set as reference image (fixed image) and the other images (moving images) are optimally adapted on the basis of a balancing transformation. So, registration is the determination of a displacement  $u(x)$  that spatially aligns the moving image  $I_M(x+u(x))$  to the reference image  $I_R(x)$ . Afterwards, the quality of alignment is defined by image similarity metrics, such as the sum of squared differences, the correlation ratio, or the mutual information.

The registration procedures are specifically designed and optimized for different applications and are divided into two categories, feature-based and intensity-based methods. The intensity-based method directly utilizes the intensity values for registration. For the feature-based method, a relatively small number of features are extracted (manually or automatically) from the images and used for the optimal registration. The advantage of the feature-based procedure in relation to the intensity-based method is the lower computational complexity and the lower noise sensitivity, as the registration is not directly dependent on intensity values. However, the major drawbacks are the pre-processing and identification of the features. [57]

There are many registration methods, composed of various transform models (rigid, affine, non-rigid), similarity measures (e.g. mutual information), optimization methods (e.g. gradient descent), interpolation methods (nearest neighbor, linear or bilinear, cubic, B-spline), and multi-resolution schemes. Registration methods based on linear transformations including translation, rotation and scaling as possible degrees of freedom

for the moving image. For the registration of complex distorted images, i.e. images with locally carrying distortions, non-rigid methods are applied. Registration is performed in most instances iteratively by minimizing and smoothing an energy function. The commonly used transformation models are listed below (see Figure 11).

- *Translation transformation* is defined as  $T(\vec{x}) = \vec{x} + \vec{t}$ , with  $\vec{t}$  as translation vector.
- *Rigid transformation* is defined with rotation and translation. The image is treated as a rigid body, thus no scaling or stretching is possible.
- *Similarity transformation* treats the image as an object with isotropic translation, rotation, and scaling.
- *Affine transformation* is a transformation with translation, rotation, scaling, and shearing options for the image registration.
- *B-spline transformation* is for the category of non-rigid transformations, with a multidimensional piecewise polynomial. This is an iterative optimization method.

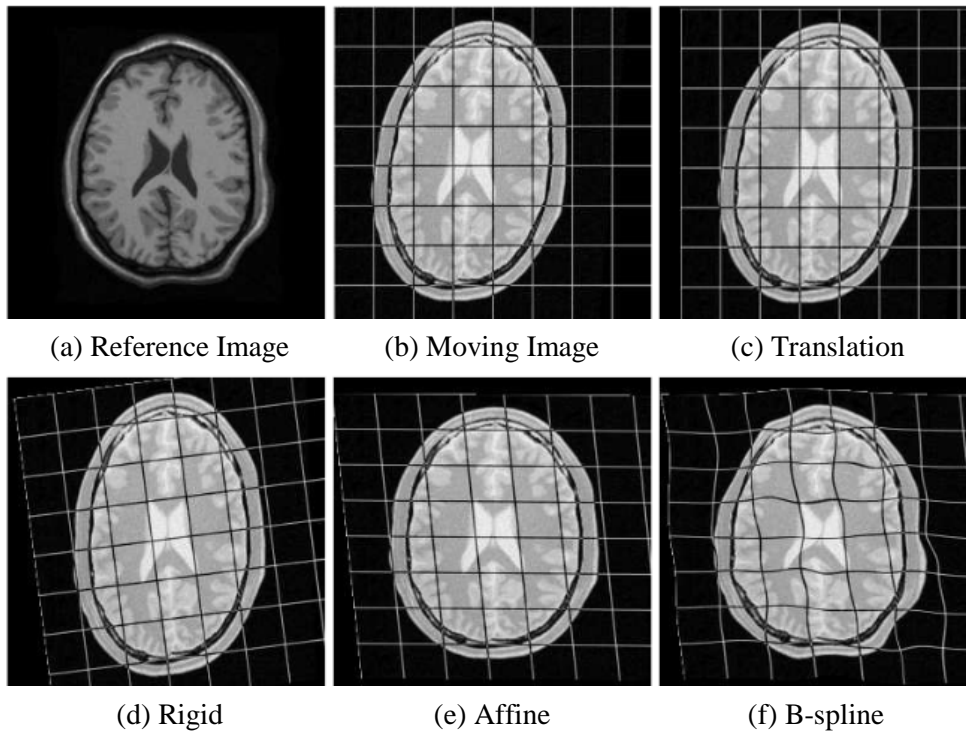


**Figure 11:** Example of the reference (a) and moving (b) image with its transformation models translation (c), rigid (d), affine (e) and B-spline (f) with the overlaid grid from the elastix manual [58, 59].

### 2.2.2 Image Segmentation

The following chapter will introduce the main image segmentation techniques utilized for this thesis. These methods represent only a small subset of commonly used image processing methods. An overview of image processing methods is presented in literature [60, 61].

Image segmentation is a technique dividing an image into different components. The detailed subdivision depends on the demand. The fastest way to segment an image is to set a threshold manually or to perform a histogram analysis. The histogram analysis method is nonparametric and divides an image histogram into two classes so that the inter-class variance is maximized [62]. The threshold value  $x$  separates the image into two classes (class 1:  $(0; x]$  and class 2:  $(x; I_{\max}]$ ).

The k-Means (kM) algorithm is an unsupervised clustering procedure. It divides a given dataset into  $k$  clusters. The procedure attempts to optimize a cost function without any training data. Therefore the minimum distances of the samples to the centroid of the associated cluster are iteratively determined. The cluster centroids are recomputed after each reassignment. [63, 64]

The Fuzzy c-Means (FcM) algorithm is an extension of the kM algorithm, using fuzzy cluster affiliations during the iterative optimization. Each part of a sample belongs to every cluster (membership degree) and after fulfilling the convergence criterion the samples are classified by associating them to their clusters with highest membership degree. The FcM is less sensitive to noise and expandable with additional terms. The kM algorithms depend on the chosen initial value and tend to a local optimum. [65, 66]

Active contour models segment images by matching closed contours and specify between inside and outside of the contour. It is an iterative optimization process, adapting the deformable contour to the favored target region in the image (e.g. edges). There are two commonly applied models, the parametric snake [67] and the non-parametric Level Set [68]. The first method is used in this thesis and is explained in more detail. Snakes provide

a tool to trace object contours even in subjects or discontinuous objects. Other edge-based techniques such as edge-detection filters (e.g. Sobel or Laplacian of Gaussian filter) only use complete objects for detection. The snake is a parametrized active contour method, where the contour is usually described by a set of points. It is supposed to minimize an energy cost function, where the external energy is derived from the image and the internal energy provides smoothness constraints to the snakes. Active contour models also detect incomplete delineated objects and thus provide more robust image segmentation in presence of noise or lower image contrast.

For a better description or variation of the form of image structures simple morphological operators are used. Morphological operators belong to the class of local operators, which consider the neighborhood of an element, and are applied on binary images. The elements of an image are either part of an object (denoted as '1') or part of the background (denoted as '0'). Morphological operators are used to manipulate the shapes of the image objects or to remove noise and operated to binary or grayscale images (not treated in this thesis).

The morphological erosion (with A referred as image and B referred as structuring element or kernel) is described by

$$A \ominus B = \{z | (B)_z \subseteq A\} \quad (2.22)$$

The erosion of A by B is the set of all displacement pixels for which B fits completely inside A. For each pixel in the image, the four (see Figure 12) or eight neighboring pixels are considered. The value of the pixel is changed from '1' to '0' if at least one neighboring pixel has the value zero. This causes the reduction of a bright image region by one pixel. The erosion works similar to a minimum filter for connected components: Dark structures are enlarged, bright areas are reduced.

The dilation represents the opposite function of the erosion and is indicated as Minkowski-Sum:

$$A \oplus B = \{z | (\widehat{B})_z \cap A \neq \emptyset\} \quad (2.23)$$

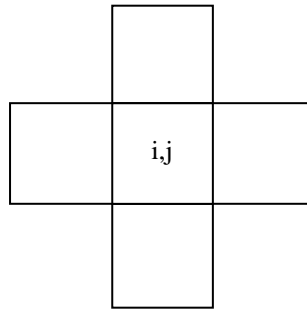


**Figure 12:** Example of a structured element by four neighboring pixels  $[i-1:i+1, j]$ ,  $[i, j-1:j+1]$ .

The dilation is the set of all displacement vectors  $z$  which cause at least one image element of  $A$  and  $(\hat{B})_z$  to overlap. In digital image processing, the dilation is generally applied by a structuring element and acts similar to a maximum filter: Bright structures are enlarged (dilated), darker areas are reduced. In binary images, the value of the pixel changes from '0' to '1' if at least one neighboring pixel has the value one.

Also, combinations of both morphological operators are possible. Erosion followed by dilation is called opening and results in a suppression of local interference from bright pixels. A dilation followed by erosion is called closing and causes a suppression of localized dark noise or a selective filtering of small dark structures.

### 2.2.3 Distortion Correction

The calculation of each pixel intensity with the distortion correction method using reversed gradient technique is exactly described in Morgan et al. [33] and is briefly summarized below.

Field inhomogeneities are generated by the spatially varying static magnetic field  $\Delta B(x,y,z)$ . The local magnetic field disturbances result in a change of the spins precession frequency by the Larmor frequency  $\gamma\Delta B(x,y,z)$ . The inhomogeneities cause spatial distortions of  $\Delta B(x,y,z)/G_r$  along the axis, where  $r$  can be  $x$ ,  $y$  or  $z$ .  $G_r$  is the strength of the effective gradient along the  $x$ -,  $y$ - and  $z$ -axis. Then the transform from the real to the distorted image space is given by

$$r_1 = r \pm \Delta B(x,y,z) / G_r. \quad (2.24)$$

Spatial distortions are considered for single-slice EPI acquisition only along the phase encoding direction ( $x$ -direction). The frequency encoding ( $y$ -direction) and the slice selection ( $z$ -direction) show no dominant influence on the distortion compared to the phase encoding direction.

If two acquisitions are performed with the same parameters but reversed phase encoding gradient, the spatial shift of the signal in the second image occurs in opposite direction along the  $x$ -axis. The spatial shift for both images is

$$x_{1/2} = x \pm \frac{\Delta B(x, y, z)}{|G_x|} \quad (2.25)$$

The spatially correct coordinate is calculated by the mean value of the shifted coordinates.

$$x = \frac{x_1 + x_2}{2} \quad (2.26)$$

The corresponding signal values are determined by performing line integrals of pixel intensity of  $x_1$  and  $x_2$ . To obtain the correct pixel intensity for the distortion corrected image, the Jacobian  $J(x_i/x)$  of the coordinate transform must be applied additionally resulting in

$$i(x) = i_1(x_1) \times J\left(\frac{x_1}{x}\right), \text{ where } J\left(\frac{x_1}{x}\right) = \frac{dx_1}{dx} \quad (2.27)$$

and

$$i(x) = i_2(x_2) \times J\left(\frac{x_2}{x}\right), \text{ where } J\left(\frac{x_2}{x}\right) = \frac{dx_2}{dx}. \quad (2.28)$$

To calculate the correct signal intensity  $i(x)$  of each pixel the differentiation of equation 2.26 is required with a substitution from equation 2.27 and 2.28 to eliminate the differentials:

$$i(x) = \frac{2 \times i_1(x_1) \times i_2(x_2)}{i_1(x_1) + i_2(x_2)}. \quad (2.29)$$

### 3 Material and Methods

The thesis focuses on the genitourinary system especially on the urethral sphincter and the kidneys with their sub-structures (cortex, medulla, and pelvis). The chapter *Material and Methods*, as well as the chapters *Results* and *Discussion* are divided into three main parts.

First, *Visualization of Urethral Sphincter* deals with the optimization of sequence parameters in order to represent the thin structure of the urethral sphincter in an animal model. High-resolution datasets illustrate both the anatomy of the urethra as well as the localization of the injected stem cells. The injected stem cells were monitored and evaluated for short and long term periods.

Second, *Segmentation of the Internal Renal Structures* represents the optimization of human abdominal image datasets regarding the delineation of the kidney from surrounding tissue and the classification of the internal renal structures. These non-contrast enhanced images are the basis for the subsequent automatic segmentation algorithm. The developed algorithm is executed on images acquired at a field strength of 1.5T.

Third, *Characterization of Distortion Corrected Diffusion Tensor Imaging* describes a fusion of the segmented areas with functional datasets. The developed segmentation algorithm was further refined and executed on images obtained at a field strength of 3T. The distortion correction algorithm based on reversed gradient method using abdominal echo planar images was developed and evaluated.

An overview of the performed examinations is shown in Figure 13.

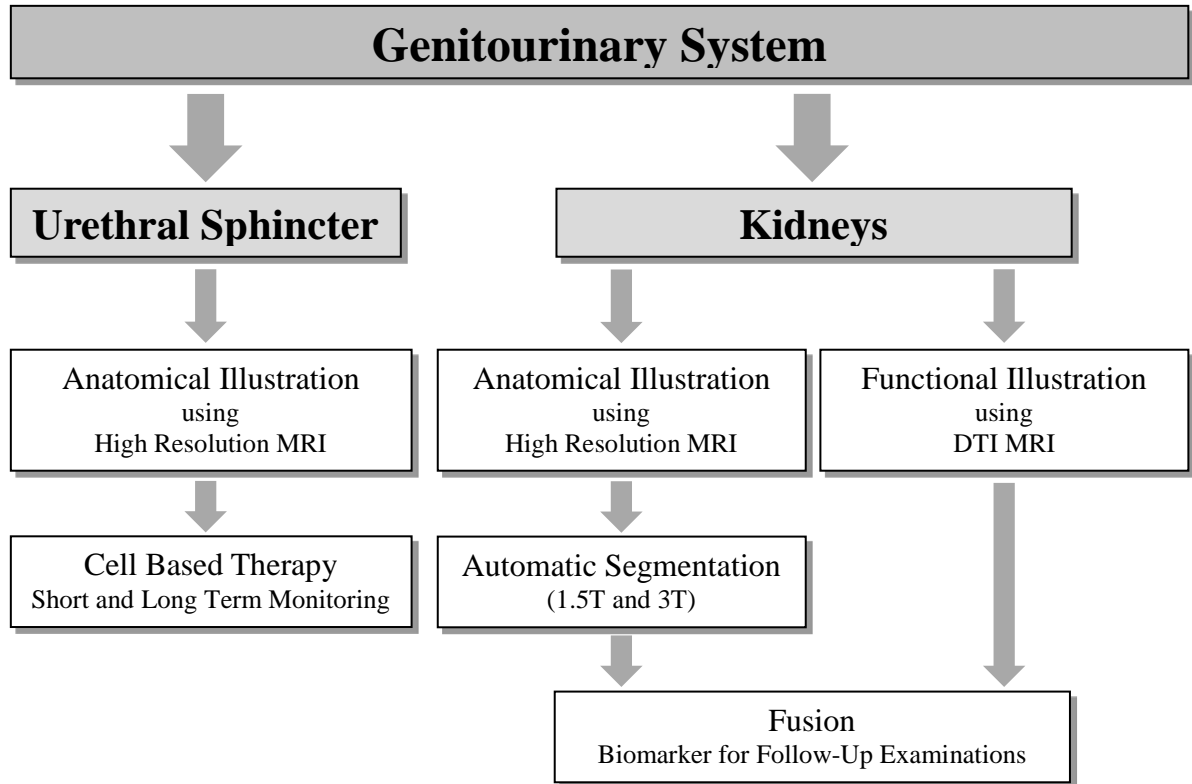


**Figure 13:** Overview of the examinations performed during this thesis, focusing on the urethral sphincter and the kidneys. First, the anatomy is visualized using high-resolution MR images. For further investigations of the urethral sphincter a cell study was executed for short and long term periods. The developed automatic segmentation algorithm based on anatomical images of the kidney. The morphological datasets were combined with functional data obtaining a biomarker for follow-up examinations.

### 3.1 Genitourinary Tract

#### 3.1.1 Kidneys

In humans, the kidney is a bean-shaped organ located retroperitoneal. It exists typically in pairs, mirrored on the spine, and is approximately at the level of the twelfth thoracic vertebra to third lumbar vertebra. The right kidney is slightly lower than the left due to the large right lobe of the liver. During inspiration the kidneys as well as the diaphragm move caudal, whereat the location of the kidneys is breathing related. Several organs of the abdomen have contact areas to the kidneys, separated by perirenal fat. The left kidney is overlaid by stomach, spleen, the pancreas and the colon, whereas the right kidney is overlaid mainly by the liver, but also by the colon and duodenum. On top of both kidneys are the bicorn adrenal glands. The kidney is approximately 11–14 cm in length, 6 cm wide and about 4 cm thick.

Urophanic substances, excess water, salts and other metabolic products are filtered from the blood by the kidneys and thus produce urine. The parenchyma of the kidney is divided into two major structures; the outer renal cortex and the inner renal medulla (see Figure 14). The functional basic unit of the kidney is the nephron consisting of renal glomeruli.

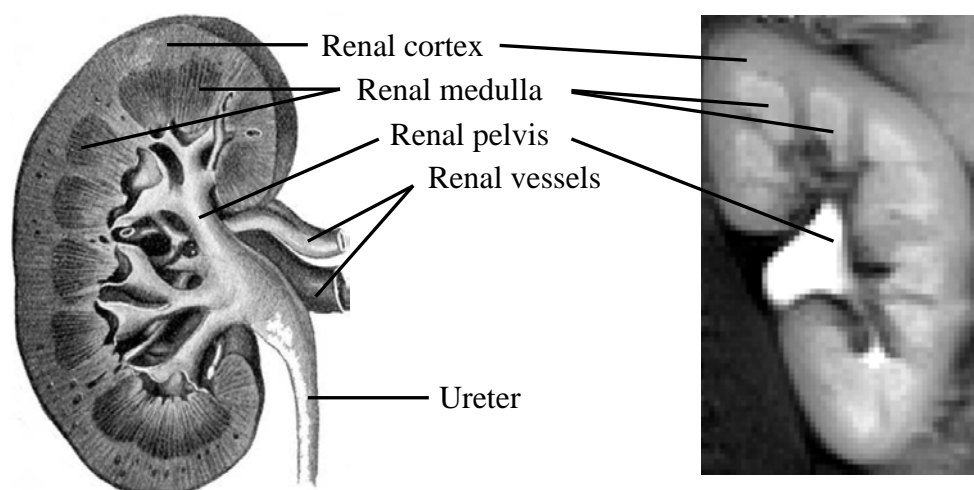


**Figure 14:** Anatomy of the right kidney with labeled renal cortex, medulla, pelvis, veins and the ureter represented schematically (left) [69] compared to a T<sub>2</sub>-weighted MR image (right).

The nephron is located in the cortex, and the following renal tubule, that passes from the cortex deep into the medullary pyramids. The primary urine is built in glomeruli by filtering the blood by cross-flow filtration. In this filtration, only the small-molecular components of blood plasma are contained in the filtrate.

However, this primary urine also contains several substances that are valuable for the body. These valuable substances, such as sugars, amino acids, electrolytes and filtered water, are reabsorbed to the circulation using the renal tubules. Therefore, the primary urine is concentrated to the final urine and transported from the renal pelvis to the ureter and the urinary bladder. The pelvic region and surrounding fat is called the renal sinus, which is within the hilum. At the hilum, the ureter and renal vein exit the kidney [70]. Both kidneys produce an average of 30 to 90 ml urine/hour.

### **3.1.2 Bladder and Sphincter**

The bladder is a hollow, muscular organ and has two basic functions: storage and regular emptying of urine. In a relaxed state the bladder can absorb about 500 ml, before a strong urge to urinate occurs. The size, shape and capacity of the bladder are individually different and depend on gender.

During the micturition the urine circulates through the urethra, arising from the bladder floor and passing through the pelvic floor. The urethra has a length of 3-5 cm in women and about 20-25 cm in men. In this thesis, the female urogenital tract is described representative. The female urogenital tract is a lined tube with mucosal tissue, extending in a slight curve behind the pubis and going through the clitoris to the vaginal opening. The micturition starts after the contraction of the bladder detrusor and simultaneous opening of the urethral sphincter. This allows coordinating both arbitrary and involuntary muscle activity and therefore a regulated and painless emptying. The urethral closure is ensured by two ring-shaped muscles, the internal and external bladder sphincter (see Figure 15). The detrusor (internal bladder sphincter) is located at the base of the bladder and cannot be arbitrarily controlled.

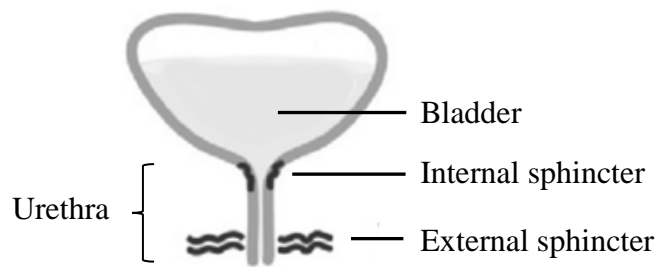


**Figure 15:** Schematic delineation of the bladder, the urethra and the internal/ external sphincter.

The passage of the urine to the urethra through the pelvic floor corresponds to the external sphincter apparatus of the bladder. The pelvic floor muscles have several different muscle groups and are controlled or trained arbitrarily. A healthy pelvic floor muscle/sphincter is therefore of central importance for the urinary continence, thereby micturition may be disturbed due to various medical conditions.

## 3.2 Visualization of Urethral Sphincter

The following chapter presents a high resolution MR imaging method of the thin structure of the urethral sphincter in an animal model. The image acquisition protocol as well as the localization of the labeled stem cells inside the urethral sphincter is described in more detail. Parts of the chapter were published by the applicant (Will et al. [71]).

### 3.2.1 MRI Acquisition

#### *Phantom study*

For measuring Superparamagnetic Iron Oxide (SPIO)-labeled mesenchymal stem cells (MSC), an agar matrix was used as a suitable environment. The agar solution (1%) was boiled and embedded in plastic boxes before it became stable. By using a special stamp, a series of identical cone-shaped cavities was created in the agar block. For MR measurement, a cell number of  $2 \cdot 10^5$  and  $5 \cdot 10^5$  MSC with ferucarbotran labeling of 200  $\mu\text{g/ml}$  medium were used. Cells were centrifuged at 200 g for five minutes, dissolved in 8% gelatin (20  $\mu\text{l}$ ), and implanted into the cone-shaped cavities within the agar matrix. For comparison, empty cavities and control cells were implanted. The PKH26 (Sigma-Aldrich, Taufkirchen, Germany) labeling for histology preparation was also tested in MRI excluding artifact generation (see Figure 16).

After the gelatin solidified, the hollows were closed with agar. Thus, it was possible to achieve a homogeneous distribution of targeted cells in a defined volume of 0.2 ml/cm<sup>2</sup> within a homogeneous agar block.

Imaging was performed on a 3T clinical whole body MR scanner (Magnetom Trio, Siemens Healthcare, Erlangen, Germany) with a bore diameter of 60 cm, slew rate of 200 T/m/s, and maximal field gradients strength of 40 mT/m. A spoiled gradient-echo (GRE) sequence with multiple  $T_E$  values of 3.92, 9.53, 15.14, 20.75, and 26.36 ms was applied as negative contrast approach, sensitive to the distribution of the Larmor-frequency near the iron particles.

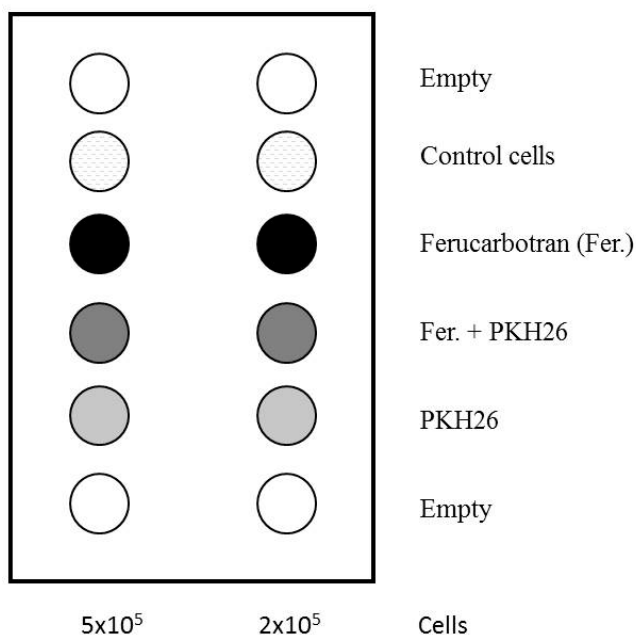


**Figure 16:** MRI agar phantom with cone-shaped cavities filled with control cells (without labeling) and cells labeled with PKH26, ferucarbotran labeling and a combination of both labeling types. Two different amounts of cells ( $5 \cdot 10^5$  and  $2 \cdot 10^5$ ) were chosen.

Higher amounts of iron result in a reduced effective transversal relaxation time ( $T_2^*$ ) and are localized as signal voids in the magnitude images. An identifier for the iron particles in contrast to the tissue with low signal intensity is the enlargement of the signal voids size with increasing  $T_E$ . The size of the signal voids in MRI also depends on the number of labeled cells. Furthermore, the SPIO particles produce field inhomogeneities illustrated as characteristically dipole field pattern in the GRE phase images. Sequence parameters of the GRE for the phantom study are summarized in Table 3.

**Table 3:** Sequence parameters: GRE sequence of the phantom and animal study for signal void detection and  $T_2$ -w FSE sequence for delineation of the urethral anatomy.

	GRE <sub>Phantom</sub>	T <sub>2</sub> -w FSE <sub>Animal</sub>	GRE <sub>Animal</sub>
T <sub>E</sub> (ms)	3.92-26.36	60	5.29-22.01
T <sub>R</sub> (ms)	50	3000	42
Number of slices	32	24	24
Slice thickness (mm)	1	2	2
Field of View (mm <sup>2</sup> )	128 × 128	134 × 200	200 × 200
Bandwidth (Hz/Pixel)	300	238	161
Flip angle (°)	25	180	25
Voxel size (mm <sup>3</sup> )	0.5×0.5×1	0.39×0.39×2	0.52×0.52×2

### *Animal study*

Iron labeling with ferucarbotran was used for in vivo cell detection of therapeutic MSC in a mini-pig model. Female “Goettingen Minipigs” (age 9 months, 17-24 kg; Ellegaard Göttingen Minipigs A/S, Dalmose, Denmark) were used as recipients for in vivo experiments. Labeled stem cells were injected transurethral under cystoscopic guidance into the urethral sphincter. Application of iron labeled undifferentiated MSC from bone marrow, placenta and adipose tissue was performed. An additional staining for cell detection was performed with PKH26 according to manufacturing manual. PKH26 is a red fluorescent cell linker kit for cell membrane labeling and is used for the detection and localization of the stem cells. According to the manufacturers' manual, PKH26 can only adhere to vital cells.

In all animals a total amount of about  $2.0 \cdot 10^6$  cells/ml was circularly injected into the rhabdosphincter and distributed over four depots, each injection containing of 250  $\mu$ l of cell suspension. To avoid a vacuum and therefore an outwards flow of the cell suspension by the moving needle, the needle remained in the injection site for additional 10 s. Ten mini-pigs were used for stem cell treatment with iron labeling: three groups of MSC populations consist of different follow-up time points (3 weeks (n=4), 3 months (n=4) and 6 months (n=2); see Figure 17). An analogous group of “sham”-operated mini-pigs (n=2), treated with MSC culture media only, served as negative control.

Measurements of post mortem mini-pigs were performed on the same scanner as used in the phantom study. The body coil was used for homogeneous radio frequency transmission and for signal detection a six elements anterior body coil and a spine coil was combined. For a better localization of the urethra, a liquid filled balloon bladder catheter (solution of sodium chloride) was utilized. The anatomy of urethra and sphincter was depicted by an adapted high resolution T<sub>2</sub>-w FSE sequence with the sequence parameters summarized in Table 3. Twenty-four slightly tilted axial slices with a thickness of 2 mm were acquired without gap in interleaved manner, leading to a scan time of about 10 minutes. The slices were positioned orthogonally to the catheter obtaining a vertical section through the urethra.

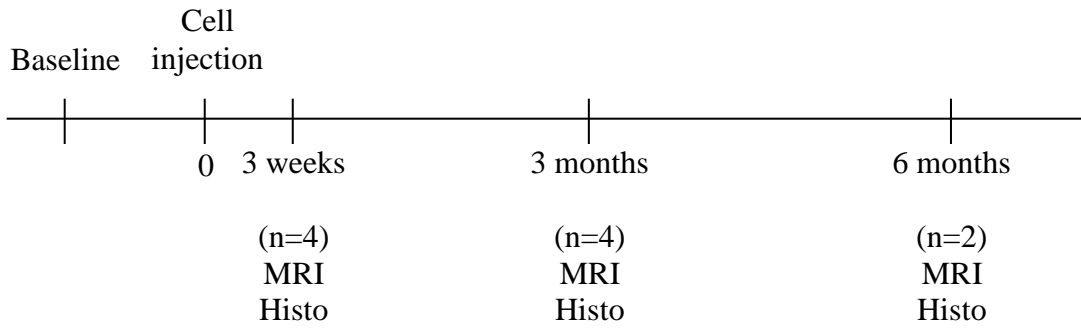


**Figure 17:** Measurements of ten mini-pigs were performed in MRI with following histological preparation at three different time points: three weeks, three months and six months after cell injection. Also two “sham”-operated mini-pigs, treated with MSC culture medium, were measured three weeks after treatment.

A GRE sequence using multiple  $T_E$  values (5.29, 13.62, and 22.01 ms) was applied to identify and verify depositions of iron particles. The slice orientation and number of slices in measurements with the GRE sequence were identical to those in the FSE sequence. Other parameters of the GRE sequence are summarized in Table 3. The images are acquired with fat suppression leading to a scan time of about 8 minutes. To identify the iron particles, the location of the signal voids in the magnitude images obtained by visual inspection and was compared to the field inhomogeneities in the phase images.

### 3.2.2 Histological Preparation

All animals were euthanized (following local ethic committee guidelines) and the entire urinary tract as well as surrounding tissue were removed. After incubating the sample overnight in 18% saccharose solution as a cryoprotective, the tissue samples were quick frozen in fluid nitrogen, embedded in tissue-freezing medium (Leica Microsystems, Wetzlar, Germany) and stored at  $-25^{\circ}\text{C}$ . Ultrathin cryotome sections of  $5\ \mu\text{m}$  were produced from each tissue sample to compare the size and the location of the iron labeled stem cells. Sections were evaluated with regard to PKH26 labeling and stained with Hematoxylin-Eosin (HE) and Prussian blue (PB) staining according to manufacturers' guidelines (Morphisto, Frankfurt am Main, Germany). The labeled cells were then visualized and evaluated via fluorescence microscopy.

For visual evaluation and subsequent comparison with histology, the urethra was divided into 12 sectors (clockwise). All signal voids in FSE MR images underwent a plausibility check. Signal voids, resulting from surrounding tissue (e.g. blood residue or air bubbles), were excluded from the evaluation. Only signal voids identified as iron labeled cell depots were considered for comparison with histological findings.

An accurate localization of signal voids is very important to determine whether the endoscopic positioning of iron labeled cells in the thin-walled sphincter muscle was successful or there was an incorrect positioning of the cells outside the urethral muscle. The localization was also evaluated in the histology staining independently by a second assessor.

### **3.3 Segmentation of the Internal Renal Structures**

MR protocols were optimized for an ideal delineation of the kidneys from the surrounding tissue to obtain an automatic segmentation approach of the kidney including the internal renal structures cortex, medulla and pelvis. This work was published in parts by the applicant (Will et al. [72]). The following section describes the image acquisition protocol, the registration algorithm and the post processing segmentation algorithm in healthy human kidneys.

The purpose of this study was to determine the accuracy of in vivo measurements of healthy human kidney volumes using non-contrast enhanced T<sub>1</sub>- and T<sub>2</sub>-w MR images. First, the feasibility of determination of the entire kidney volume in healthy humans by MR measurements without contrast agent is evaluated. This step includes an adaptation of the MR imaging parameters in the context of an automatic segmentation procedure. Second, an automatic algorithm was implemented for renal segmentation with a combined differentiation of the internal renal structures as cortex, medulla and pelvis based on high resolution MR images. Afterwards, the results of the automatic segmentation algorithm were compared to a manual segmentation (reference standard). Finally, the repeatability of the renal volume and sub-volume measurements was evaluated.

#### **3.3.1 MRI Acquisition**

In vivo measurements of healthy volunteers were performed on a 1.5T whole body MR scanner (Magnetom Sonata, Siemens Healthcare, Erlangen, Germany). The body coil was used for homogeneous RF transmission and 12-element anterior-posterior phased array coils were applied for signal detection. This methodological study was approved by the local ethics committee and an informed consent was obtained from all subjects.

Two clinical MR protocols were adapted in order to obtain a sufficient differentiation of the entire kidneys from the surrounding organs as well as to differentiate the internal renal structures. For the segmentation of the entire kidneys, a T<sub>2</sub>-w half-Fourier

single-shot turbo spin echo (HASTE) sequence was used. For this sequence, the echo time ( $T_E$ ) was varied to achieve maximum kidney-liver and kidney-spleen contrast. For segmentation of the internal renal structures, a  $T_1$ -w spoiled gradient echo (GRE) sequence was used and the contrast between renal cortex and medulla maximized by varying the flip angle. Adaptation of these two parameters was performed during initial measurements of three healthy volunteers.

The HASTE sequence was applied with the following parameters:  $T_R$  1800 ms, bandwidth (BW) 781 Hz/Pixel, flip angle  $150^\circ$ , voxel size  $1.71 \times 1.37 \times 5.00$  mm<sup>3</sup>, field of view (FoV)  $350 \times 350$  mm<sup>2</sup>, and parallel acquisition factor of 2. For accurate slice excitation both kidneys were covered in a single breath-hold. To minimize the required number of slices, coronal slice orientation was chosen. Thirteen slightly tilted coronal slices (parallel to the orientation of the kidney axis) with a thickness of 5 mm were acquired without gap in interleaved manner, leading to a scan time of 23 s. The echo time  $T_E$  was varied from 61 to 122 ms in order to determine the optimal contrast for the kidney segmentation.

Slice orientation and voxel size in measurements with the GRE sequence were identical to those in the HASTE sequence. Other parameters of the GRE sequence were set to:  $T_R/T_E$  132/2.44 ms, BW 260 Hz/Pixel, leading to a scan time of 19 s. In order to optimize the contrast between cortex and medulla, the excitation flip angle was varied between  $30^\circ$  and  $90^\circ$  in steps of  $10^\circ$ . Fat saturation was applied to both  $T_1$ - and  $T_2$ -w measurements to improve the overall image contrast and to avoid chemical shift artifacts.

With the adapted sequence parameters, measurements in 12 healthy volunteers (mean age  $33 \pm 11$  years and body mass index (BMI) of  $25 \pm 4.3$  kg/m<sup>2</sup>) were performed to acquire the data for the kidney segmentation.

### 3.3.2 Image Registration

Since the two datasets were acquired in different breath-holds, possible displacements of the kidneys between  $T_1$ -w and  $T_2$ -w datasets had to be compensated for. Thus, the  $T_1$ -w images were co-registered slice-wise to the  $T_2$ -w images using the registration

program ELASTIX [58]. The following registration parameters were optimized in order to obtain high registration accuracy for the given images: Transformation model (rigid, non-rigid), number of downsampling steps (1, 2, 3), polynomial order of the interpolation (1, 2, 3) and the number of iterations (200-1000). As a merit function for the optimization, in two datasets the kidney areas were manually labeled in three medial slices of T<sub>1</sub>-w and T<sub>2</sub>-w datasets. After each registration run, the intersection area of the kidneys in the registered T<sub>1</sub>-w and T<sub>2</sub>-w images was calculated (separately for the left and right kidney) and expressed as percentage deviation from the kidney areas in the T<sub>2</sub>-w images. Furthermore, non-rigid distortions inside the kidneys (e.g. medulla) were evaluated visually.

### 3.3.3 Automatic Segmentation Algorithm

Image segmentation was performed in two steps using MatLab (Version R2011b, The MathWorks, Natick, USA). First, the entire kidneys were segmented of surrounding tissues by thresholding the T<sub>2</sub>-w images and a subsequent refinement step using prior knowledge about the kidney shape and location. In a second step, T<sub>1</sub>-w and T<sub>2</sub>-w images were used to distinguish between the renal structures (cortex, medulla, and pelvis). All thresholds specified in this algorithm were determined and tested manually in several subjects for the same measurement setup and sequence parameters. The obtained optimal values were held constant for the automatic segmentation algorithm.

*Entire kidney segmentation:* A preliminary kidney mask was obtained for each slice of T<sub>2</sub>-w data separately by applying an empirically determined threshold at 32% of the maximum pixels' intensity in the slice. It was assumed that all pixels above this threshold belong to the kidney. Since the spleen, the vertebrae and some parts of the gastrointestinal tract showed similar signal intensity values as the kidney, this initial mask was further refined. All image segmentation steps were performed for the right and left kidney separately. Due to the very small distance between the superior pole of left kidney and spleen, the threshold-based algorithm may generate a common area and splits the splenorenal recess into two parts.

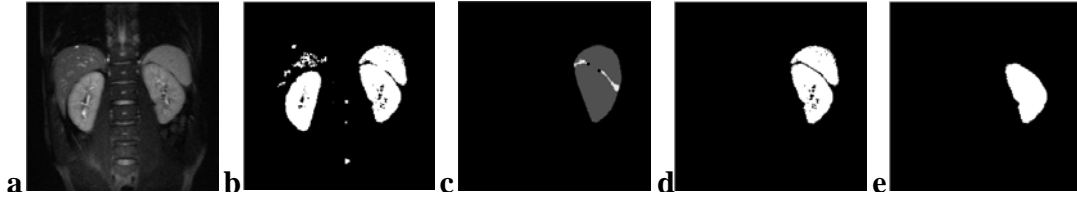


**Figure 18:** Separation of the spleen and the kidney using preliminary mask (b) from T<sub>2</sub>-w images (a): The subtraction of the mask from the convex hull resulted in two splenorenal regions (light grey, c). Separation of the kidney from the spleen was performed along the shortest line connecting the splenorenal regions (set points, d) resulting in the final binary mask of the left kidney (e).

To remove this artificially generated connection between kidney and spleen, the convex hull of the combined area was calculated. Then, two splenorenal regions were identified by subtracting the connected area from the convex hull. The separation of the kidney from the spleen was performed along the shortest line connecting the splenorenal regions (see Figure 18). Finally, the obtained binary mask was refined using active contours [67]. For the use of active contour some adjustment parameters are specified prior to the procedure. These parameters have not been altered during execution of segmentation. For edge detection the image was filtered using a Gaussian filter.

Another step isolates the gastrointestinal tract from the kidney, as it was also artificially detected as kidney in the initially binary mask. The algorithm started at the central slice where the kidney has its maximum extension and is not impaired by partial volume effects. Afterwards, the algorithm propagated outwards in both directions. Since the gastrointestinal tract is located at the lower end of the kidneys, only the lower halves of the binary kidney masks were considered, thus keeping the already well segmented areas. Based on the currently processed mask (denoted as  $M_i$ ), several test points along the contour were compared to corresponding points of the previous mask (denoted as  $M_{i-1}$ ). If these test points are outside the segmented area of the previous contour, the form of the kidney outline of this mask was transferred to the current mask by taking the intersection of both masks ( $M_i \leftarrow M_i \cap M_{i-1}$ ).

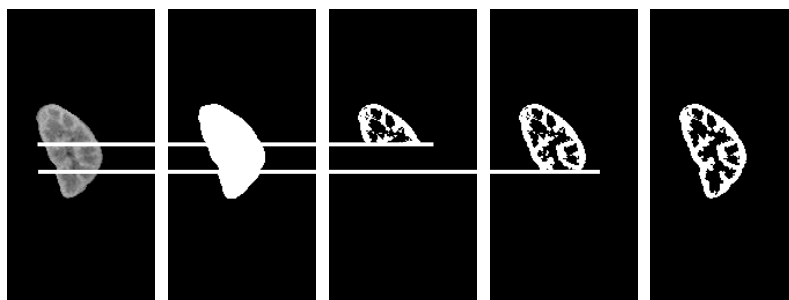


**Figure 19:** The classification of the cortex was realized slice-wise and for left and right kidney separately. The signal distribution was analyzed in each row of the kidney in the T<sub>1</sub>-w image. All pixels with a value above the local threshold were assigned to cortex.

*Renal structure segmentation:* Within the generated entire kidney mask, the renal cortex, medulla, and pelvis were subsequently separated. This separation algorithm utilizes assumptions of the renal anatomical structure, e.g. that the renal cortex surrounds parts of the medulla.

T<sub>1</sub>-w images were used to segment the renal cortex for left and right kidney separately. Due to intensity inhomogeneities, a single threshold for the entire kidney was found to be inadequate. Instead, classification of the cortex was realized by analyzing signal distribution in each row of the kidney (see Figure 19). All pixels with a value above a local threshold were assigned to cortex. This threshold was calculated as the row's mean intensity value inside the kidney mask minus the standard deviation. In addition, the first and last slices containing kidney tissue pixels (different for right and left kidney) were labeled exclusively as cortex.

The algorithm for the segmentation of pelvis used both, T<sub>1</sub>- and T<sub>2</sub>-w images. The final pelvis mask was obtained by fusion of both segmented areas. Pelvis appears as a hypointense region of the kidney in T<sub>1</sub>-w images. Images with T<sub>2</sub>-w contrast are helpful in differentiation between pelvis and ureter. Therefore, the pelvis segmentation was executed in two steps: Fluid (urinary) areas showed lower signal intensity than renal parenchyma tissue in T<sub>1</sub>-w images. In the first step, the slices including parts of the renal pelvis were determined in T<sub>1</sub>-w images with a fixed threshold (Figure 20a). This threshold based on the darkest areas of the image. In the second step, the segmentation of pelvis was performed in T<sub>2</sub>-w images, where pelvis appears as brightest area of the entire kidney region (Figure 20b). For this purpose, the pelvis was separated using a region based threshold (pixel values higher than 80% of the mean signal intensity of the entire kidney

were assigned to pelvis). These steps led to occasional misclassifications of fat pixels along the outer parenchyma in cases where the kidney mask was slightly larger than the kidney shape. Those undesired pixels were identified through their position (lateral) and deleted from the pelvis mask. Along with the segmented pixels classified as pelvis the union pelvis mask was obtained (Figure 20c). Subsequently, the pelvis mask was subtracted from the cortex mask to remove erroneously identified pixels.

Finally, the renal medulla mask was obtained by subtracting the cortex and pelvis masks from the entire kidney mask. The final volumes of the entire kidneys, renal cortex, medulla and pelvis were then calculated by voxel summation (voxel volume is  $1.37 \times 1.37 \times 5 \text{ mm}^3$  or  $9.38 \text{ mm}^3$ ). The complete segmentation process is presented in Figure 21.

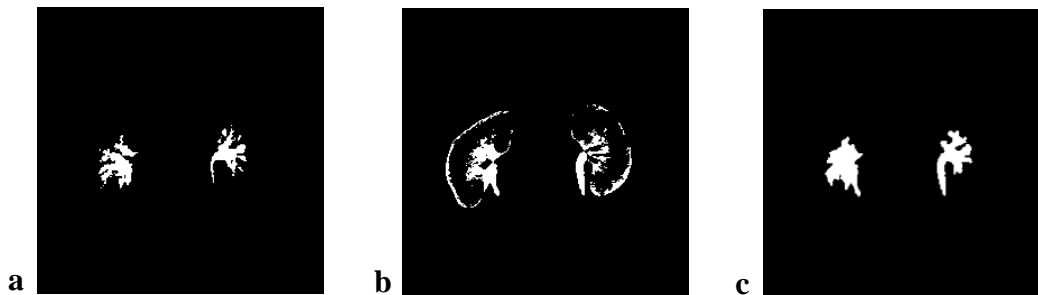


**Figure 20:** Resulting binary pelvis mask (a) from the segmentation of  $T_1$ -w images. Second binary pelvis mask (b) resulted from the segmentation of  $T_2$ -w images. Combination of both masks produced the final binary mask of the pelvis (c) for an exemplary slice.

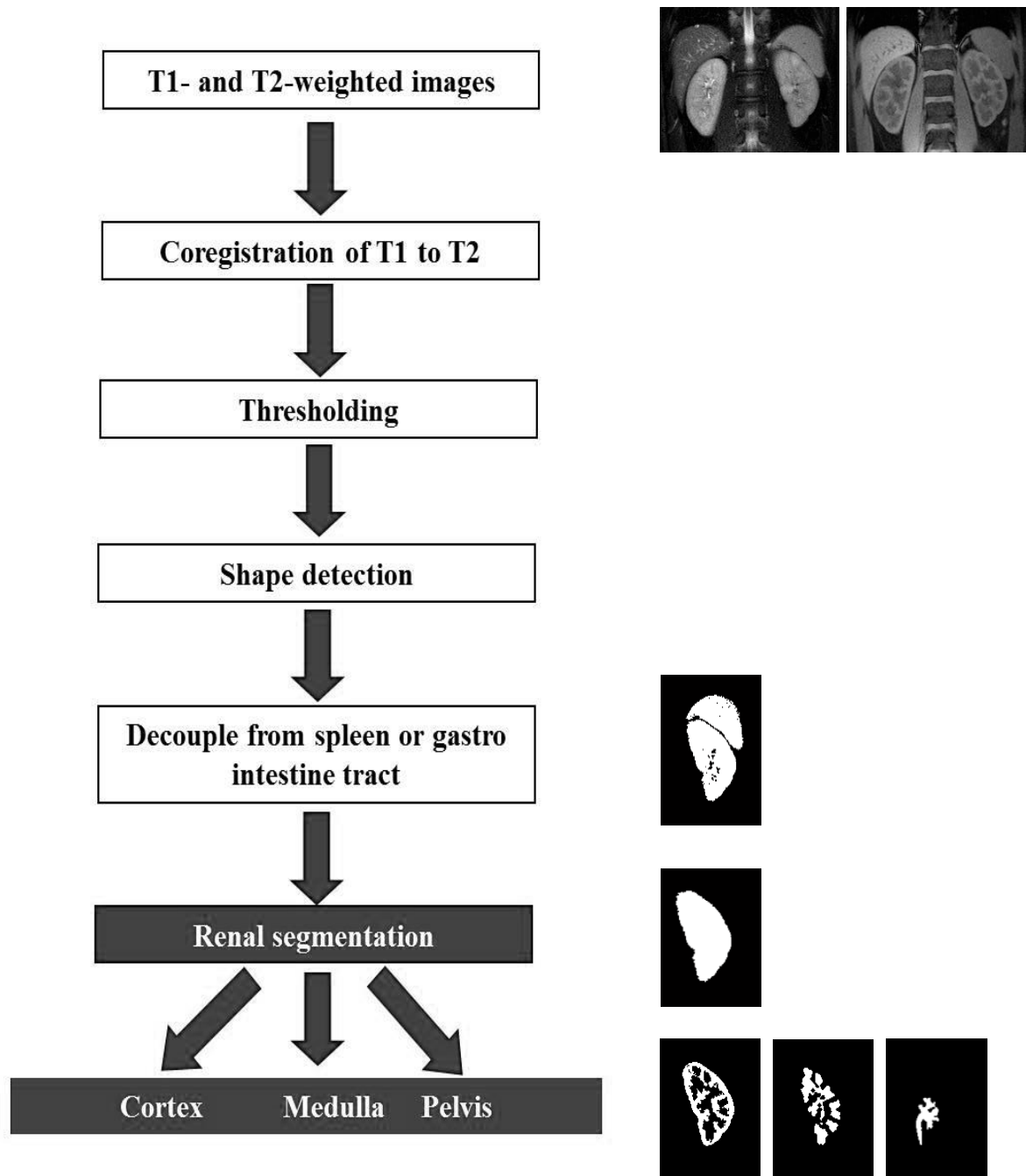


**Figure 21:** Block diagram of the complete segmentation procedure of the entire kidney and renal structures cortex, medulla and pelvis.

### 3.3.4 Evaluation

A custom user interface based on MatLab was implemented to create reference standard masks for the entire kidneys (based on T<sub>2</sub>-w MR images), renal pelvis (based on T<sub>1</sub>- and T<sub>2</sub>-w images) and medulla (based on T<sub>1</sub>-w images). The reference standard masks for

each volunteer were carefully drawn manually in each slice. The reference mask for the cortex was obtained by subtracting the pelvis and medulla masks from the entire kidney mask.

For the evaluation of the accuracy of the optimized algorithm, volume error ( $ve$ ) and overlap error ( $oe$ ) of automatic and manual segmentation were calculated using the following formulas:

$$ve = abs\left(\frac{|V_A| - |V_M|}{|V_M|}\right) \quad (3.1)$$

$$oe = \frac{|V_M \cup V_A| - |V_M \cap V_A|}{|V_M|} \quad (3.2)$$

Here,  $V_M$  and  $V_A$  represent the sets of voxels belonging to the manually and automatically segmented volumes, respectively, and the  $|V|$  operator is used to determine the cardinality of the sets. To compare the results with existing work, volume overlap ( $vo$ , also known as Jaccard index) and Dice's coefficient ( $dice$ ) [73] were calculated according to

$$vo = \frac{|V_M \cap V_A|}{|V_M \cup V_A|} \quad (3.3)$$

$$dice = \frac{2|V_M \cap V_A|}{|V_M| + |V_A|} \quad (3.4)$$

A repeatability study was performed in order to evaluate the variations between measurements of the same subject with the same sequence protocol and scanner. One volunteer was subsequently scanned three times after repositioning on the scanner table. Then, for each dataset the kidney volume was obtained by the proposed automatic segmentation algorithm, and the coefficient of variation (standard deviation divided by mean value) of the three volumes was calculated.

### **3.4 Characterization of Distortion Corrected Images from DTI**

The following chapter presents the transfer of automatically segmented areas of the kidney based on high resolution anatomical images to distortion corrected functional datasets. Therefore an approach including distortion correction and superposition was performed to enable the calculation of fractional anisotropy and mean diffusivity of the entire specific areas of cortex, medulla and pelvis.

An accurate quantification approach for distortion corrected diffusion tensor images of the kidney was obtained in healthy volunteers, including a differentiation of internal renal structures. For this purpose, the automatic segmentation results - based on non-contrast enhanced high resolution anatomical imaging [72] - were transferred to the distortion corrected functional maps derived from renal echo-planar DTI. Distortion correction is executed based on DTI images acquired with opposite phase encoding directions. The quality of this approach was tested by comparison to results from manual segmentation in functional map. Possible influences of partial volume effects were examined and strategies for avoiding such effects are reported. In addition, the distortion correction approach using standard EPI image datasets was compared to distortion correction using multiband (MB) EPI.

#### **3.4.1 MRI Acquisition**

In vivo measurements of 10 healthy volunteers (7 men, mean age  $30.4 \pm 9.4$  years; range: 24-50 years) without any history of kidney diseases were performed. The volunteers had no specific preparation prior to measurement such as fasting or drinking. All measurements were performed on a 3T whole body MR scanner (Magnetom Skyra, Siemens Healthcare, Erlangen, Germany) using a body coil for homogeneous RF transmission and 12-element anterior-posterior phased array coils for signal detection. This methodical study was approved by the local ethics committee and written informed consent was obtained from all subjects. Volunteers were positioned head first in supine position.

Two MR sequences, a T<sub>2</sub>-w half-Fourier single-shot turbo spin echo (HASTE) and a T<sub>1</sub>-w spoiled gradient echo (GRE), were applied in order to obtain a sufficient

differentiation of the entire kidneys from the surrounding organs as well as reliable differentiation of internal renal structures (cortex, medulla and pelvis). All images were acquired with fat suppression and multi-breath-hold (2x16s). The slices were acquired parallel to the orientation of the kidney axis. Sequence parameters are summarized in Table 4.

For determination of the diffusion tensor a diffusion-weighted single-shot spin-echo echo-planar imaging (DW-SE-EPI) sequence was applied. Slice orientation was oblique coronal, slightly tilted parallel to the long axis of the kidneys. Sixteen slices were acquired with a respiratory belt triggering. EPI data were collected with two different phase-encoding directions (Head-Feet, H>>F, and Feet-Head, F>>H). This procedure results in geometric distortions in opposite directions. b-values were chosen to 0 and 400 s/mm<sup>2</sup>; diffusion-sensitizing gradients were applied along 30 different directions, using a bipolar diffusion gradient scheme [74]. Acquisition time was about 4min 47s depending on the respiratory rate of each subject. In order to minimize possible shifts during respiratory triggering the DW-SE-EPI images were registered on the first b0 image using SPM (Statistical Parametric Mapping, Version 8, London, UK). The calculated functional maps were also co-registered slice-wise to the anatomical T<sub>2</sub>-w images using Elastix.

**Table 4:** Sequence parameters: T<sub>2</sub>-w HASTE sequence for entire kidney segmentation; T<sub>1</sub>-w GRE sequence for internal structure segmentation; DW-SE-EPI sequence for diffusion tensor imaging.

	<b>T<sub>2</sub>-w HASTE</b>	<b>T<sub>1</sub>-w GRE</b>	<b>DW-SE-EPI</b>
T <sub>E</sub> , ms	92	3.21	85
T <sub>R</sub> , ms	2000	120	1700
Number of slices	16	16	16
Slice thickness, mm	3.5	3.5	3.5
Acq. matrix	320 × 320	320 × 320	192 × 192
FoV, mm <sup>2</sup>	400 × 400	400 × 400	400 × 400
Phase resolution, %	100	70	67
Phase FoV, %	100	100	100
Partial Fourier	4/8	7/8	6/8
Parallel acq. factor	2	2	2
BW, Hz/Pixel	710	260	1736
Averages	1	1	1
b-values, s/mm <sup>2</sup>	-	-	0, 400
Affiliation	breath-hold	breath-hold	respiratory-triggered

### 3.4.2 Registration and Segmentation

Registration and segmentation of the anatomical images is based on the approach described in Chapter 3.2.3. The segmentation approach was further refined and is described below.

The basic structure of the segmentation algorithm is similar to that presented previously. However, adjustments are made so that the algorithm also works for images recorded at 3T. Changes in signal intensity and SNR of the images were adapted, so that the sequence-dependent thresholds were not required. Suitable threshold values were adapted, as the setup and the magnetic field strength were changed.

*Entire kidney segmentation:* The algorithm started at the central slice where the kidney has its maximum extension and is not impaired by partial volume effects. Afterwards, the algorithm propagated outwards in both directions. The preliminary kidney mask was obtained for each slice of T<sub>2</sub>-w data separately by applying three classes (class I: background, class II: dark tissue, class III: bright tissue). All pixels belonging to class III were retained. Since spleen, liver, vertebrae and some parts of gastrointestinal tract show signal intensity values similar to the kidneys' values, this initial mask had to be further refined. All image segmentation steps were performed for the right and left kidney separately.

Because of the very small distances between kidney and liver in thin volunteers, the artificially generated connection was removed with a new algorithm. Therefore, the connecting points between liver and right kidney are detected by moving along the outer contour of the kidney and the two regions are separated by a linear line. Separation of the spleen and the gastrointestinal tract is performed as described previously. Finally, the obtained binary mask was refined using active contours [67].

*Renal structure segmentation:* The substructures cortex, medulla and pelvis are first created as described in the first algorithm. However, the adjacent slices and not only the previous slice are used for eliminating incorrect detected pixels. By summing three slices only the areas which are extend over at least two slices are retained.

The final volumes of the entire kidneys, renal cortex, medulla and pelvis were calculated by voxel summation (voxel volume is  $1.25 \times 1.25 \times 3.5 \text{ mm}^3$  or  $5.47 \text{ mm}^3$ ).

### 3.4.3 Distortion Correction

For distortion correction the reversed gradient method was used [33]. EPI data were collected with two opposed phase-encoding directions, resulting in pairs of images with distortions going in opposite directions. From these image pairs the susceptibility-induced off-resonance field was estimated [32] using FSL TOPUP [75]. Based on this off-resonance field map two distorted images were combined into a single corrected one. The adapted parameters are listed below and saved in a configuration file:

```
warpres = 20, 16, 14, 12, 10, 6, 4, 4, 4;  
subsamp = 2, 2, 2, 2, 2, 1, 1, 1, 1;  
fwhm = 8, 6, 4, 3, 3, 2, 1, 0, 0;  
miter = 5, 5, 5, 5, 5, 10, 10, 20, 20;  
lambda = 0.005, 0.001,  $1.0 \cdot 10^{-4}$ ,  $1.5 \cdot 10^{-5}$ ,  $5.0 \cdot 10^{-6}$ ,  $5.0 \cdot 10^{-7}$ ,  $5.0 \cdot 10^{-8}$ ,  $5.0 \cdot 10^{-10}$ ,  $1.0 \cdot 10^{-11}$ ;  
ssqlambda = 1;  
regmod = bending_energy;  
estmov = 1, 1, 1, 1, 1, 0, 0, 0, 0;  
minmet = 0, 0, 0, 0, 0, 1, 1, 1, 1;  
splineorder = 3;  
numprec = double;  
interp = spline;  
scale = 1.
```

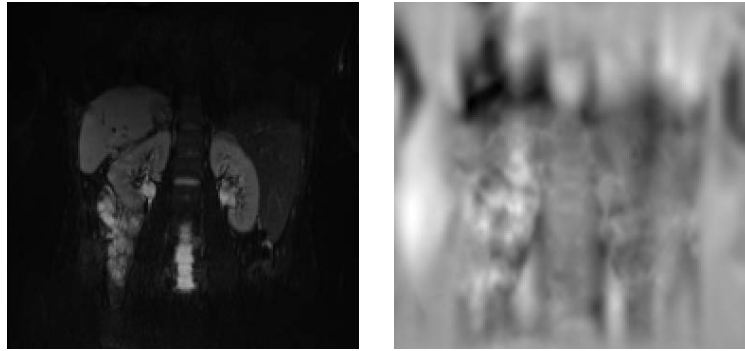


**Figure 22:** The first b0 images (b0 (F>>H) and b0 (H>>F), left) are used to obtain a susceptibility-induced off-resonance field (right) with dark areas corresponding to -50Hz and bright areas to 150Hz.

Only the first pair of b0 images (b0 (H>>F) to b0 (F>>H)) was used in the first step of FSL TOPUP to estimate a susceptibility-induced off-resonance field (see Figure 22) by locating the maximized similarity gauged by the sum-of-squared differences of the unwarped volumes. The dicom images are converted into the required nifty format. *topup* will attempt to estimate the field with the input parameters b0 images (*bothdata*), the acquisition parameter file ('*acqpara.txt*') and the configuration file:

- `fslmerge -t bothdata FH_1 HF_1`
- `topup --imain=bothdata --datain=acqpara.txt --config=bo2bo.cnf --out=results  
--iout=unwarpedIm`

The resulting field was applied as input for the other sets of image pairs. Hereby, it was assumed that the susceptibility induced field will be constant for all acquired images. *applytopup* calculates the undistorted images with the input parameters of all image pairs (*FH<sub>i</sub>*, *HF<sub>i</sub>*, where  $i=1\dots n$ ), the acquisition parameter file and the estimated field generated by *topup*:

- `applytopup --imain=FH_$i, HF_$i --inindex=1,2 --datain=acqpara.txt --topup=results  
--out=/Entzerrt_ep2d/Entz_$i`

After combining two EPI datasets with opposite phase encoding directions into a single distortion corrected one, mean diffusivity (*MD*) and fractional anisotropy (*FA*) maps were calculated by using a home-made routine [76] written in MatLab.

$$FA = \frac{3(\lambda_1 - \bar{\lambda})^2 + (\lambda_2 - \bar{\lambda})^2 + (\lambda_3 - \bar{\lambda})^2}{2\sqrt{\lambda_1^2 + \lambda_2^2 + \lambda_3^2}} \quad (3.5)$$

$$MD = \frac{\lambda_1 + \lambda_2 + \lambda_3}{3} \quad (3.6)$$

The distortion corrected diffusion-weighted images were noise corrected corresponding to Gudbjartsson et al. [77]. The diffusion tensor was calculated as reported by Basser et al. [78] i.e., the eigenvalues  $\lambda_{1-3}$  and the corresponding eigenvectors  $v_{1-3}$  were calculated pixelwise. *MD* and *FA* maps of the kidneys were derived from these data. The functional maps were interpolated to the resolution of the anatomical segmentation masks.

#### 3.4.4 Image Analysis

Due to shift artifacts at the edges of the boundary slice after registration and increasing partial volume effects, the evaluation was performed for all slices as well as for ten central slices. The comparison is intended to illustrate the difficulties at the boundary slices and the impact of two-dimensional acquisition.

Anatomical masks calculated on the basis of T<sub>1</sub>- and T<sub>2</sub>-w images were superimposed to *MD* and *FA* maps and qualitatively checked by visual inspection. Homogeneity of results in segmented areas (representing either cortex, medulla or pelvis) was checked by assessment of mean *values* and standard deviation of *FA* and *MD*. Possible influences of partial volume effects from picture elements from transitional areas were assessed by additional calculations with eroded picture elements close to segmentation borders. On a binary mask, erosion causes an enlargement of dark structures and a decrease of bright structures by one pixel. The eroded masks were then superimposed to obtain mean values and standard deviation of *FA* and *MD* and subsequently compared to the standard generated masks.

For evaluation of the accuracy of distortion correction approach a manual segmentation of the entire kidney was performed on *MD* maps. The reference masks for each volunteer were carefully drawn manually in two chosen medial slices. The volume error, overlap

error, volume overlap and Dice's coefficient of the manual and the automatic segmentation were calculated [72].

### 3.4.1 Multiband Technique

MB-EPI approaches enable the acquisition of DTI images by acquisition of multiple slices clearly faster than standard EPI.

Four healthy volunteers were examined on a clinical 3T MR scanner (Magnetom Prisma, Siemens Healthcare, Germany) with anterior and posterior surface array coils. T<sub>2</sub>-w FSE and T<sub>1</sub>-w GRE images were applied for anatomical segmentation. Diffusion-weighted single-shot spin-echo echo-planar (DW-SE-EPI) sequences were applied with standard and multiband technique (MB-factor 2) using respiratory triggering. DTI data were collected with two different phase-encoding directions and combined using the FSL TOPUP tool. The segmented masks were then superimposed to the calculated *MD* and *FA* maps and the results were verified by visual inspection. *MD* and *FA* values of renal cortex and medulla were compared between standard and multiband approach.



## 4 Results

### 4.1 Visualization of Urethral Sphincter

Phantom measurements revealed that iron labeled cells are detectable in both, magnitude and phase GRE images. Field inhomogeneities show a characteristically dipole-shaped pattern in GRE phase images, which allows a clear allocation of iron particles. With increasing  $T_E$  both, signal voids (in the magnitude images) and dipole field patterns (in the phase images) enlarge (see Figure 23). The control cells without iron labeling do not show substantial changes in signal intensity.

With the data obtained from the phantom measurements the optimal iron charge and the optimum amount of cells was found that has to be injected into the animal sphincter. Due to the clear localization of the urethra through the liquid filled bladder catheter, all iron depots were detected.

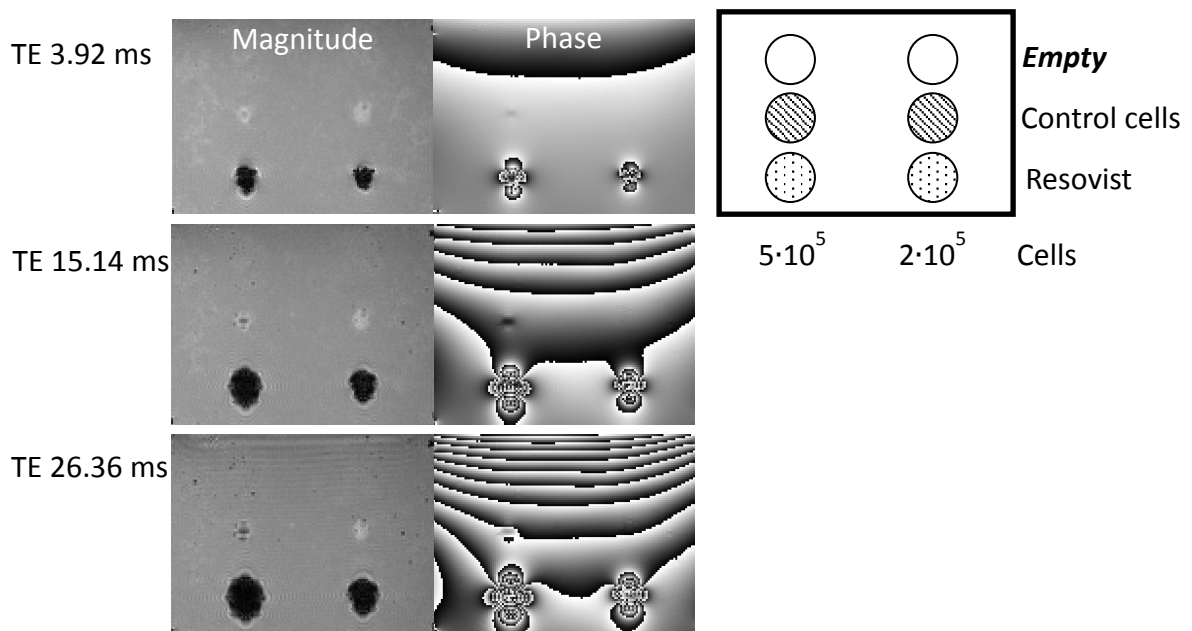


**Figure 23:** MRI phantom measurements show different numbers of cells ( $5 \cdot 10^5$  and  $2 \cdot 10^5$ ) with and without iron labeling. GRE magnitude images visualize the iron particles as signal voids. In contrast to normal tissue structures, the size of the signal voids enlarges with increasing  $T_E$  (3.92, 15.14 and 26.36 ms) and thus is an explicit identifier for iron particles. In GRE phase images the field inhomogeneities show a characteristic dipole field pattern. [71]

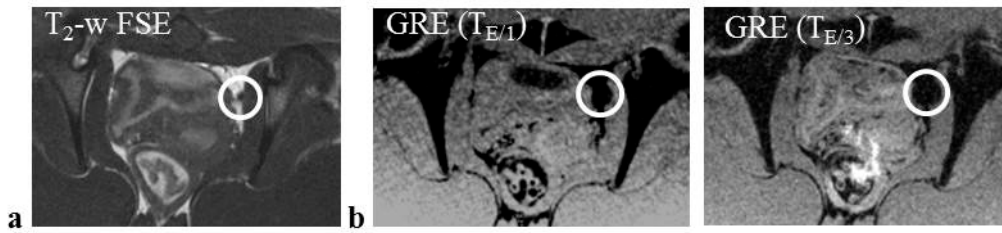


**Figure 24:** T<sub>2</sub>-w FSE transverse slice of the region cranial of the bladder with conspicuous lymph node (a) showed an amplified signal void. The GRE images with two different T<sub>E</sub> values (b) showed the presence of iron particles, caused by either loose iron particle or death labeled cells which are transported from the injection area to the lymph nodes.

Due to a very small size of the sphincter muscle (only a few millimeters), the iron deposits have accumulated outside the muscle in the surrounding tissue in some cases. This was probably attributed to an incorrect application of cells during the injection procedure. One mini-pig (three weeks after injection) received a further MR examination for the evaluation of the lymph nodes. Iron particles were detected inside one specific lymph node (see Figure 24). This suggests that the loose iron particles as well as dead labeled cells might be transported to the lymph nodes.

Furthermore, iron deposits were detectable in all three time periods (see Figure 25). In addition, non-precise injections were located by detecting cells outside of the sphincter muscle in MR images.

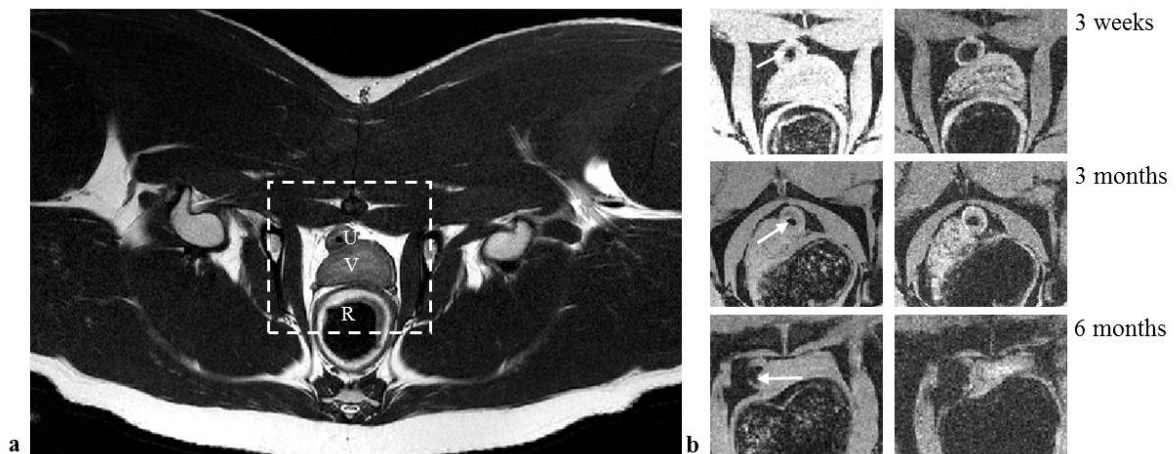


**Figure 25:** (a) High resolution T<sub>2</sub>-w FSE images of a female mini-pig and GRE images at two different TE values (5.29 and 22.01 ms) with cell injection depot on the left side from the liquid filled bladder catheter 3 weeks, 3 months and 6 months after injection (b). U, urethra; V, vagina; R, rectum. [71]

No difference was detected in the individual depot areas with different MSC. The “sham”-operated mini-pigs showed no increasing signal voids and therefore no iron particles by the treatment with MSC culture media.

The endoscopically applied cells were detectable by MRI and correlated well with the histological specimen. The comparison of MRI and tissue sections showed preeminent accordance of location and extension of iron depots (see Figure 26). Tissue analysis of harvested urethras revealed up to four detected cell depots in nearly all animals with heterogeneous localization within muscle and connective tissue.

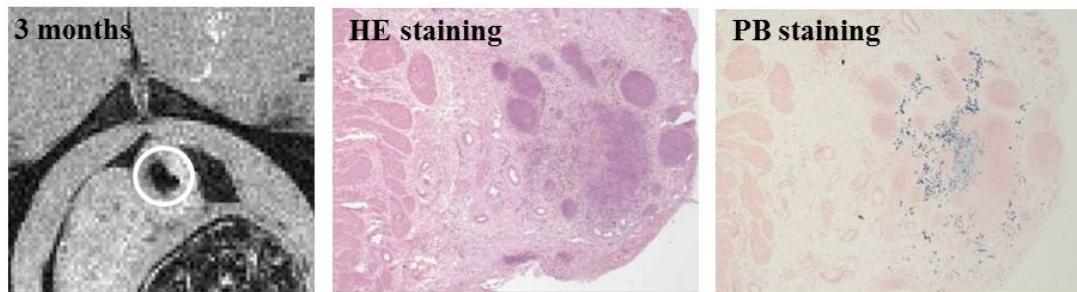


**Figure 26:** GRE image of iron labeled cells three months after injection correlated well with the histological staining. The Hematoxylin-Eosin (HE) and Prussian Blue (PB) staining show the distribution of iron particles. [71]

## 4.2 Segmentation of the Internal Renal Structures

### *MRI Sequence Optimization*

In order to be able to differentiate the entire kidneys from the surrounding organs (liver, spleen and gastrointestinal tract) and their internal structures, two MR sequences were adapted. The contrast-to-noise ratios (CNR) between cortex and medulla in the T<sub>1</sub>-w GRE images measured at different flip angles are listed in Table 5. Considering these CNR values as well as the contrast between the kidneys and surrounding tissues, flip angle of 70° was found to be an acceptable trade-off.

Table 6 lists CNR values between different tissues in T<sub>2</sub>-w HASTE images measured at varied echo times. The CNR between kidney and liver was maximal at T<sub>E</sub> of 82 ms, while the maximum CNR between kidney and spleen occurred at T<sub>E</sub> of 102 ms. Therefore, T<sub>E</sub> of 95 ms was selected for the HASTE sequence. Corresponding T<sub>1</sub>- and T<sub>2</sub>-w images of one volunteer obtained with these adapted sequence parameters are shown in Figure 27.

**Table 5:** Contrast-to-noise ratios between renal cortex and medulla for the left (CNR<sub>C/M,l</sub>) and right (CNR<sub>C/M,r</sub>) kidney obtained at different flip angles ( $\Theta$ , deg) using a T<sub>1</sub>-w GRE sequence with T<sub>R</sub> of 132 ms and T<sub>E</sub> of 2.44 ms. CNR<sub>C/L</sub> values between liver and right renal cortex and CNR<sub>C/S</sub> values between spleen and left renal cortex are presented as well. Flip angle of 70° is an acceptable trade-off.

$\Theta$	CNR C/M,l	CNR C/M,r	CNR C/L	CNR C/S
30	9.57	9.41	1.62	8.18
40	11.96	13.66	1.41	<u>8.78</u>
50	13.04	<u>13.97</u>	6.24	7.76
60	13.20	13.21	<u>6.39</u>	7.75
<b>70</b>	<b><u>13.70</u></b>	<b>12.91</b>	<b>6.30</b>	<b>8.62</b>
80	11.32	13.46	<u>6.39</u>	6.33
90	11.06	11.61	5.93	5.79

*Underlined entries show the optima in each category, the bold entries signal the chosen trade-off.*

## Results

**Table 6:** Contrast-to-noise ratios between kidney-liver ( $CNR_{K/L}$ ) and kidney-spleen ( $CNR_{K/S}$ ) measured at different  $T_E$  using a  $T_2$ -w HASTE sequence with  $T_R$  of 1800 ms.  $T_E$  of 95 ms proved to be an acceptable trade-off for all tissues studied.

$T_E$ , ms	$CNR_{K/L}$	$CNR_{K/S}$
61	16.43	0.34
71	19.06	0.96
82	<u>19.86</u>	1.20
92	18.15	2.51
<b>95</b>	<b>19.28</b>	<b>2.77</b>
102	16.52	<u>3.90</u>
112	15.55	2.95
122	18.79	3.55

*Underlined entries show the optima in each category, the bold entries signal the chosen trade-off.*

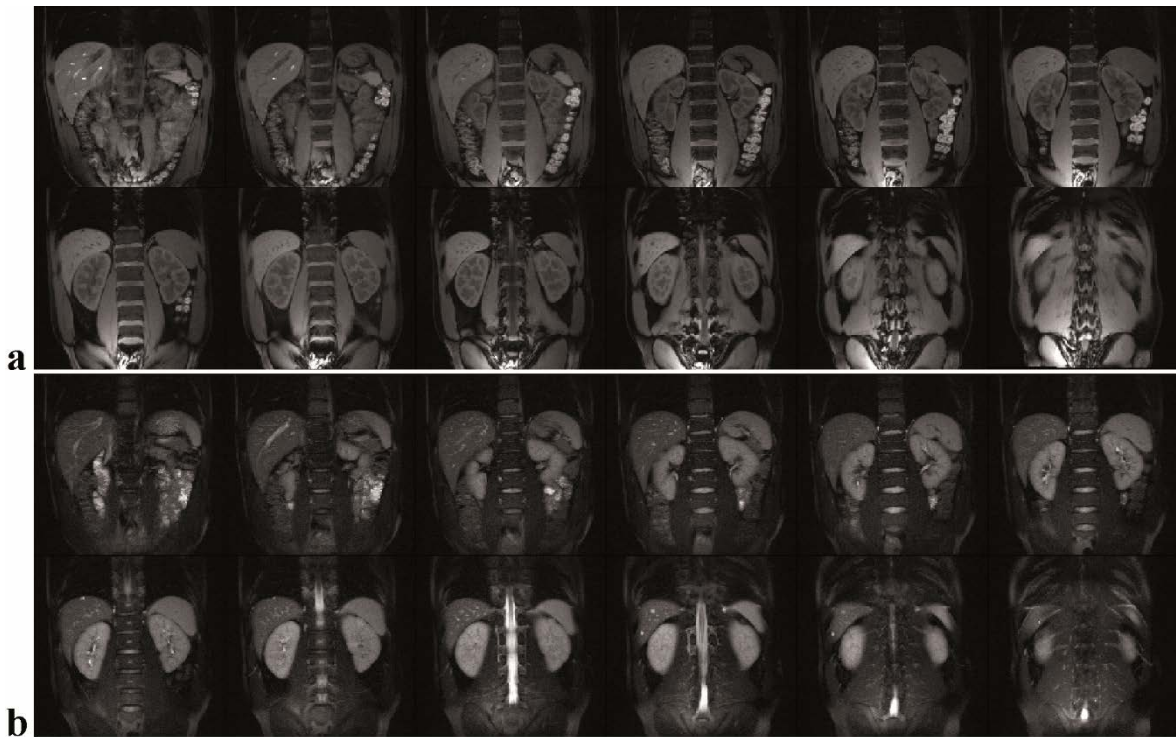


**Figure 27:** Optimized  $T_1$ -w (a) and  $T_2$ -w (b) images of a healthy subject. In this volunteer twelve slices with a thickness of 5 mm (without gap) were necessary to cover the entire kidneys. [72]

### Image Registration

To find the optimal registration algorithm, eleven different parameter sets were tested. For each parameterization, the percentage deviation of the manually labeled kidney areas between the T<sub>2</sub>-w images and the post-registered T<sub>1</sub>-w images was calculated (Figure 28). When employing the non-rigid deformation model, high deviations have been found in all three slices (parameter sets 1-8). In some cases, the kidneys' inner structures showed even worse alignment than without registration, while the outer kidney boundary was well registered. This behavior was most likely caused by the lack of contrast between cortex and medulla in the T<sub>2</sub>-w images. In contrast, using the rigid deformation model resulted in clearly better alignment both at the kidney surface and the boundaries inside the kidneys (see Figure 29). The best alignment (mean deviation of 4.26% and 2.87% for left and right kidney, respectively) was obtained using a rigid deformation model with two resolution levels, cubic BSpline interpolation, normalized mutual information metric and 200 iterations (parameter set 11). The computation time of this registration procedure was about 70 s per image resulting in the processing time of approximately 15 minutes for the entire dataset.

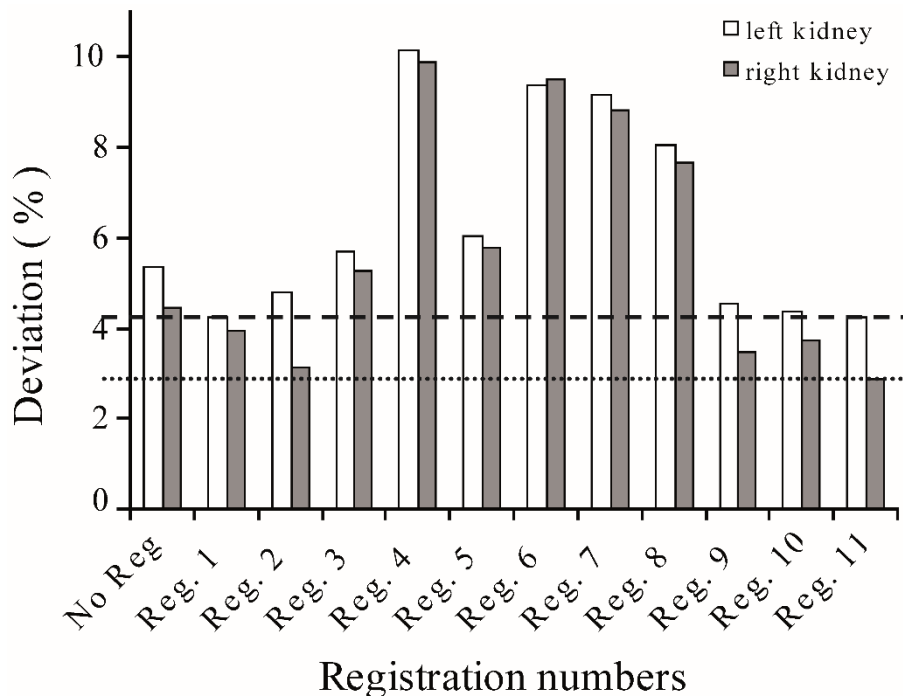


**Figure 28:** Percentage deviation in manually labeled kidney areas between T<sub>1</sub>- and T<sub>2</sub>-w images using different registration parameters. Rigid registrations (registration number 9-11) resulted in a higher internal agreement than non-rigid ones (1-8). Registration 11 showed the best results for all three slices with a mean deviation of 4.26% and 2.87% for left and right kidney. [72]

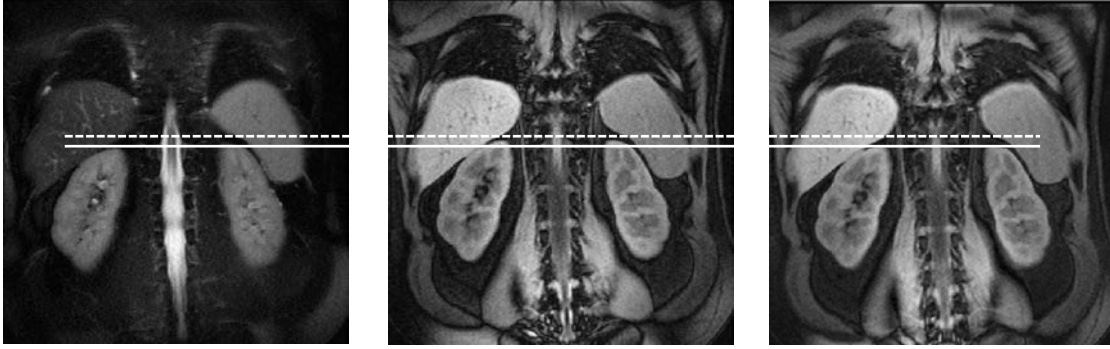


**Figure 29:** Illustration of the registration with the T<sub>2</sub>-w image (a) as reference image, the T<sub>1</sub>-w image as a moving image and the resulting image (c).

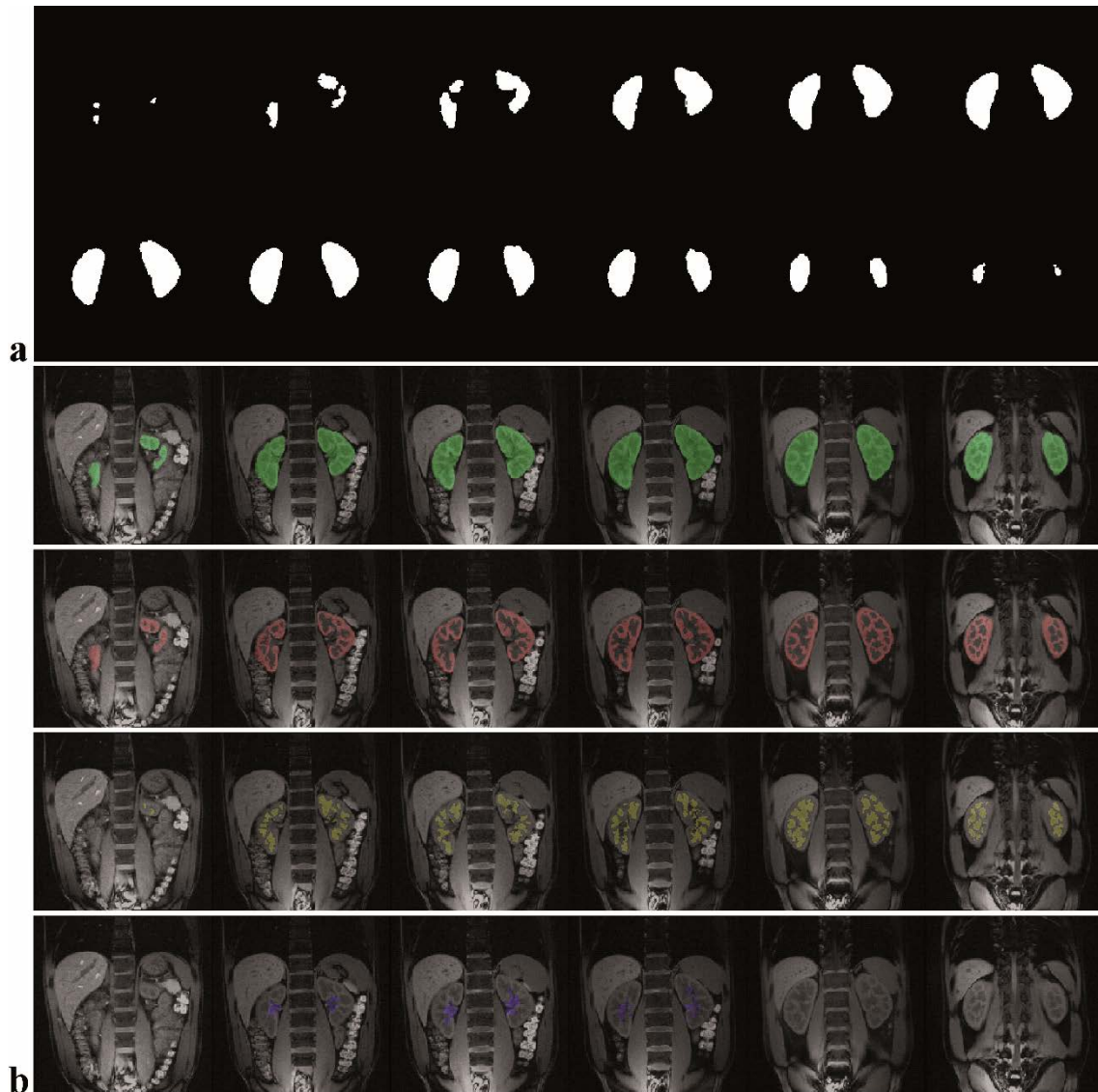
### Segmentation Algorithm

Figure 30a shows representative results for the kidney masks creation on the basis of the T<sub>2</sub>-w images for all slices. Figure 30b demonstrates the corresponding successful segmentation of cortex, medulla and pelvis for selected slices. All determined coefficients are summarized in Table 7. The resulting *ve* of  $4.97 \pm 4.08\%$  for the entire kidney and  $7.03 \pm 5.56\%$  for the cortex in all 12 subjects shows high agreement between manual and automatic segmentation.

The standard deviation regarding data of the renal pelvis is higher than values of other renal structures. However, the standard deviations of the entire kidney, cortex and medulla volumes are relatively low showing a high agreement between manual and automatic segmentation. The overlap errors for the entire kidney and cortex are acceptable. Due to their geometric structure the overlap errors of medulla and pelvis are more evident than in renal cortex.

**Table 7:** Mean and standard deviation values (in %) for the volume error (*ve*), overlap error (*oe*), volume overlap (*vo*) and Dice's coefficient (*dice*) calculated from all 12 subjects.

	Kidney	Cortex	Medulla	Pelvis
<i>ve</i>	$4.97 \pm 4.08$	$7.03 \pm 5.56$	$12.33 \pm 7.35$	$17.57 \pm 14.47$
<i>oe</i>	$12.58 \pm 2.48$	$37.35 \pm 6.04$	$56.36 \pm 8.58$	$54.40 \pm 12.14$
<i>vo</i>	$88.07 \pm 2.30$	$67.92 \pm 4.51$	$57.14 \pm 5.17$	$56.53 \pm 8.72$
<i>dice</i>	$93.64 \pm 1.31$	$80.82 \pm 3.22$	$72.59 \pm 4.30$	$71.87 \pm 6.91$



**Figure 30:** Automatically created segmentation masks for the entire kidneys of one healthy volunteer for all slices (a). Visualization of the automated segmentation of the entire kidneys (green), renal cortex (red), medulla (yellow) and pelvis (blue) for several slices superimposed to  $T_1$ -w MR images (b). [72]

The *vo* and *dice* coefficient base on different algorithms. Both values are described in this study to obtain a better comparison to literature values. The volume overlap generally shows smaller values than the *dice* coefficient. A simulation (Figure 31) shows the calculated values in relation to the overlapping area. The dice coefficient is linearly depended on the shared area, while the volume overlap reveals a non-linear character. Despite the different values both coefficients show the same overlapping area, demonstrated by our calculated values in Table 7.

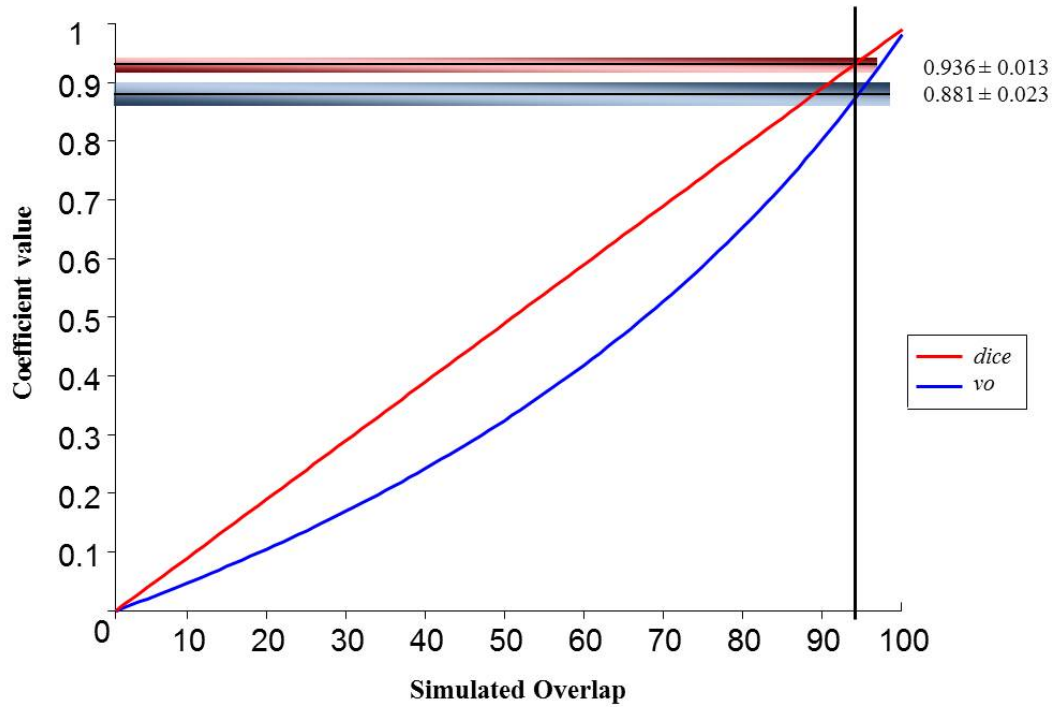


**Figure 31:** The simulation shows the calculated values of the Dice' coefficient (*dice*, red) and the volume overlap (*vo*, blue) in relation to the overlapping area. The Dice coefficient is linearly depended on the shared area, while the volume overlap reveals a non-linear character. Despite the different values (*vo* shows in general smaller values than *dice*) both coefficients show the same overlapping area.

The results of a slice-wise comparison of the manual and automatic segmentation are shown in Figure 32. A high correlation of the segmented areas was observed with the determination coefficients ( $R^2$ ) of 0.96, 0.88, 0.92 and 0.87 for the entire kidney, cortex, medulla and pelvis, respectively. Furthermore, the lines obtained by linear regression (solid lines) are in good accordance to the lines of identity (dashed lines), indicating correct tissue area quantification. Only the pelvis area quantification shows minor systematic underestimation.

In the repeatability study, the kidney volume between all three trials deviated by 4.76% calculated from the within-subject coefficient of variation. Internal structures showed deviations of 6.35% (cortex), 1.74% (medulla) and 16.33% (pelvis).

## Results

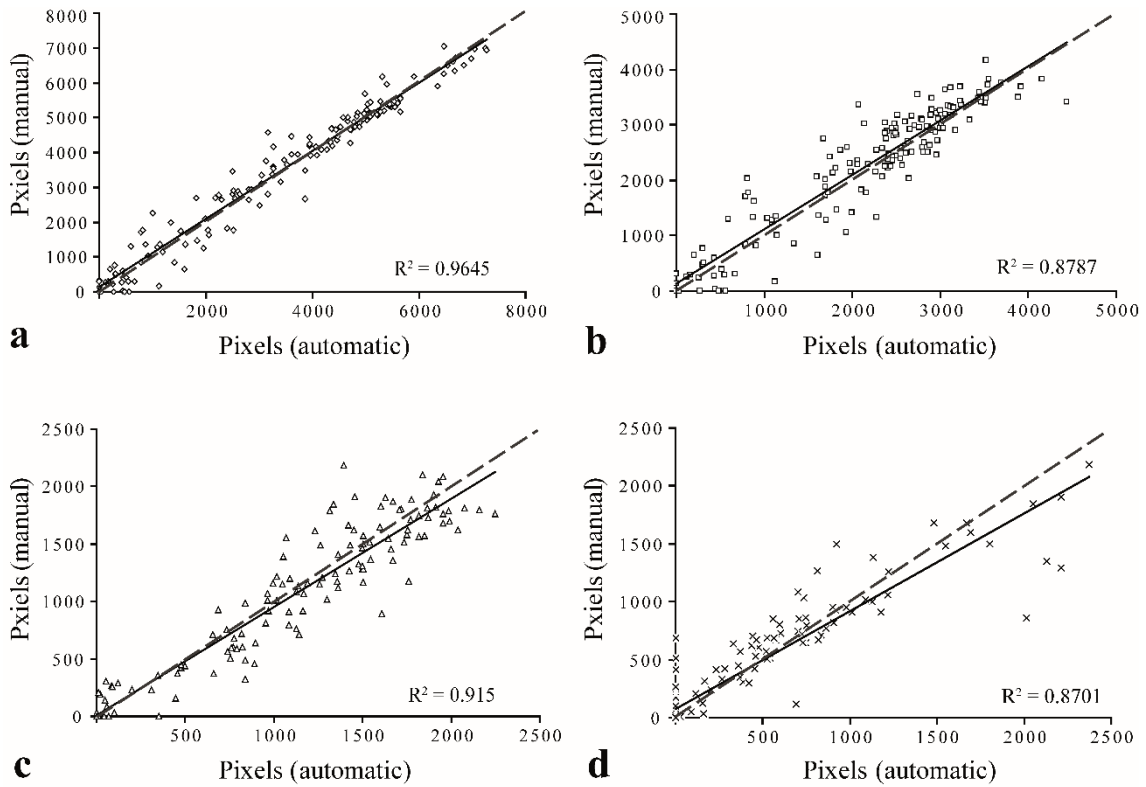


**Figure 32:** Comparison of manually and automatically created segmentation areas for each slice of entire kidney (a), cortex (b), medulla (c) and pelvis (d) of all 12 volunteers (--- line of identity). One pixel equates 1.88 mm<sup>2</sup>. [72]

The automatically (manually) obtained mean total volume of both kidneys over all volunteers was  $404.8 \pm 70.9$  cm<sup>3</sup> ( $412.1 \pm 71.7$  cm<sup>3</sup>). The mean volumes of cortex, medulla and pelvis for automatic and manual segmentation are listed in Table 8 below.

**Table 8:** Mean volumes (in cm<sup>3</sup>) and standard deviation over all 12 volunteers for the entire kidney, cortex, medulla and pelvis of the automatic and the manual segmentation.

Volume	Automatic	Manual
Entire kidney	$404.8 \pm 70.9$	$412.1 \pm 71.7$
Cortex	$252.1 \pm 42.1$	$263.9 \pm 47.7$
Medulla	$108.9 \pm 16.1$	$104.0 \pm 16.8$
Pelvis	$44.0 \pm 24.7$	$45.8 \pm 18.6$

## Results

---

The ratio between cortex and the entire kidney volume was  $64.0 \pm 3.0\%$  ( $62.4 \pm 2.5\%$ ) on average, the ratio between medulla and the entire kidney volume was  $25.4 \pm 3.0\%$  ( $27.1 \pm 3.1\%$ ) and the ratio between medulla and cortex volume was  $43.5 \pm 4.8\%$  ( $39.9 \pm 5.9\%$ ).

The computation time of the automatic segmentation algorithm including mask generation, region determination and export of the results was about 50 s for the entire dataset.

### 4.3 Characterization of Distortion Corrected Images from DTI

#### *Segmentation*

One subject was excluded from this study because several sets of images showed distinct motion artifacts.

The automatically obtained mean total volume of both kidneys over all volunteers is  $386.6 \pm 77.0 \text{ cm}^3$ . The mean volumes of cortex, medulla and pelvis are determined to  $248.3 \pm 44.0 \text{ cm}^3$ ,  $104.2 \pm 20.4 \text{ cm}^3$ , and  $34.6 \pm 16.0 \text{ cm}^3$  respectively. Planimetry of the central ten slices show an area of about 81.4% of the entire kidney area, 76.0% of the cortex area, 89.3% of the medulla area and 96.3% of the pelvis area.

#### *Distortion correction*

In contrast to the uncorrected EPI images, distortion corrected EPI images show a high congruence with the anatomical kidney mask. Figure 33 shows the automatic segmentation mask of the entire kidney superimposed to the anatomical  $T_2$ -w image, a DTI image (b0) with opposite phase-encoding direction ( $H \gg F$  and  $F \gg H$ ) and a distortion corrected image.

The paramedial slices show small deviations, while the central slices of the distortion corrected images match well with the anatomical segmentation.

As mentioned above, manually segmentation of the entire kidney was performed in *MD* maps across all slices and for later comparison over ten middle slices. The manually obtained mean total volume of both kidneys over all volunteers drawn in *MD* maps is  $379.2 \pm 85.7 \text{ cm}^3$ . Planimetric analysis of the central ten slices covers about 82.3% of the entire kidney area.

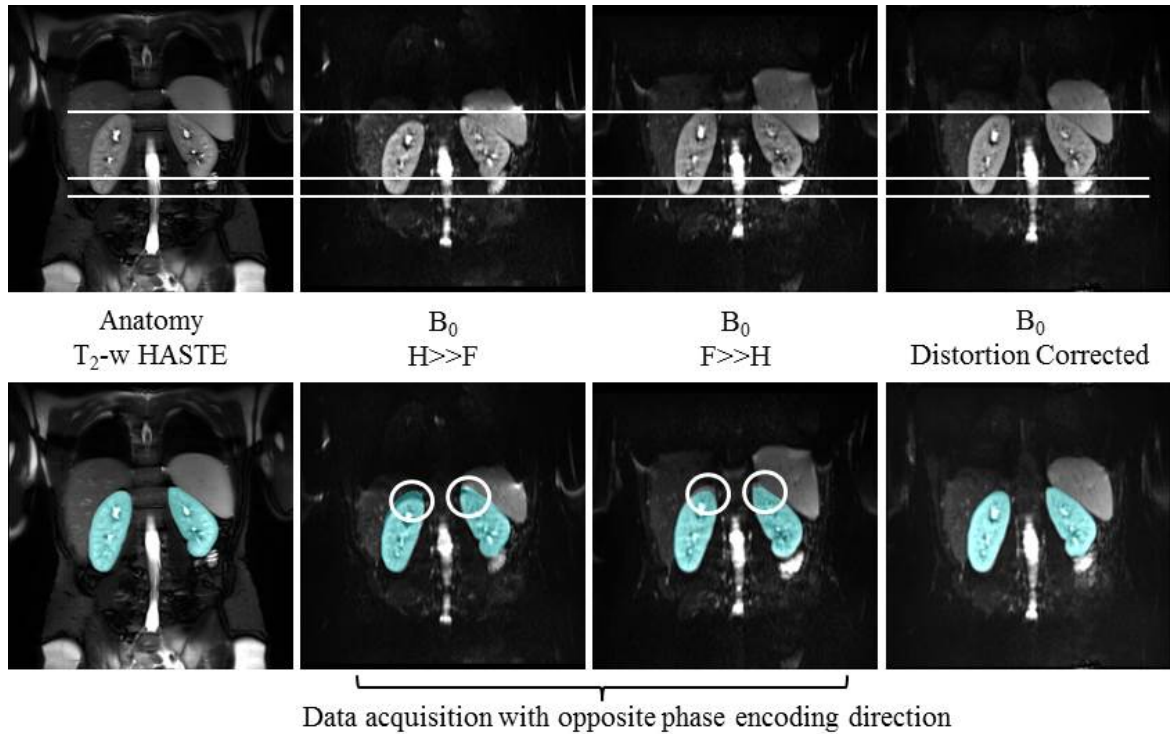


**Figure 33:** Superimposed entire kidney mask to  $T_2$ -w HASTE image,  $b_0$  images with  $H \gg F$  and  $F \gg H$  phase-encoding directions and the distortion corrected image.

The mean  $ve$  for all 9 subjects over ten middle slices (over all slices) is  $2.92 \pm 1.55\%$  ( $4.77 \pm 3.41\%$ ), showing high agreement between manual segmentation in the functional maps and automatic segmentation in anatomical images. Also mean  $oe$  of  $13.31 \pm 2.89\%$  ( $19.72 \pm 3.67\%$ ),  $vo$  of  $87.62 \pm 2.50\%$  ( $82.32 \pm 2.85\%$ ) and the *dice* coefficient of  $93.38 \pm 1.43\%$  ( $90.28 \pm 1.71\%$ ) show a successful operation of the used distortion correction approach.

Results of a slice-wise comparison of the manual and automatic segmentation are shown in Figure 34. A high correlation of the segmented areas is observed with the determination coefficient ( $R^2$ ) of 0.94 for the entire kidney. Therefore, a high correlation of the other segmented masks like cortex, medulla and pelvis is expected.

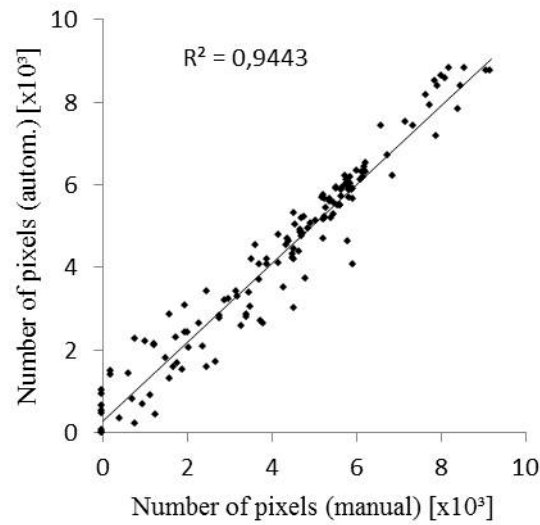


**Figure 34:** Slice-wise comparison of segmented areas between manual segmentation of *MD* maps and automatic segmentation of anatomical  $T_2$ -w images.

The resulting automatically generated masks were superimposed to the calculated distortion corrected *FA* (Figure 35) and *MD* maps. Mean and standard deviation *FA/MD* values of cortex, medulla and pelvis are given in Table 9 for all slices and for ten central slices. A comparison between all slices and only the central slices in *FA* maps shows almost the same value in the pelvis region. The pelvis usually does not extend to the outer slices and thus reducing the slice number shows no influence on *FA* values. The medulla region shows a noticeable increase of 3.8%, while the values in the cortex area decrease by approximately 1.4% in all slices. Generally no differences in the *MD* values of the regions cortex and medulla are recognizable, which is reflected in the analysis using only central slices.

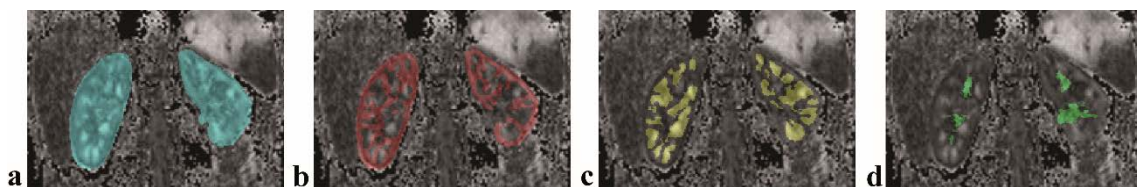


**Figure 35:** Automatic segmented masks of the entire kidney (a), cortex (b), medulla (c) and pelvis (d) superimposed to distortion corrected *FA* maps.

## Results

**Table 9:** Calculated mean and standard deviation fractional anisotropy ( $FA$ ) and mean diffusivity ( $MD$ ,  $10^{-3}$   $\text{mm}^2/\text{s}$ ) values for automatic segmented masks of cortex, medulla and pelvis with and without erosion for all slices and ten central slices.

	Normal masks		Eroded masks	
	<u>all slices</u>	<u>central slices</u>	<u>all slices</u>	<u>central slices</u>
$FA_{\text{Cortex}}$	$0.209 \pm 0.020$	$0.206 \pm 0.017$	$0.205 \pm 0.020$	$0.201 \pm 0.017$
$FA_{\text{Medulla}}$	$0.265 \pm 0.034$	$0.275 \pm 0.038$	$0.278 \pm 0.040$	$0.291 \pm 0.045$
$FA_{\text{Pelvis}}$	$0.197 \pm 0.013$	$0.196 \pm 0.010$	$0.193 \pm 0.012$	$0.192 \pm 0.009$
$MD_{\text{Cortex}}$	$2.710 \pm 0.153$	$2.602 \pm 0.079$	$2.723 \pm 0.161$	$2.613 \pm 0.080$
$MD_{\text{Medulla}}$	$2.646 \pm 0.117$	$2.660 \pm 0.119$	$2.628 \pm 0.127$	$2.634 \pm 0.122$
$MD_{\text{Pelvis}}$	$3.580 \pm 0.746$	$3.590 \pm 0.739$	$3.722 \pm 0.850$	$3.707 \pm 0.825$

The small difference between the two regions in the evaluation with all slices results from the misalignment of the superimposed masks in the marginal slices.

To show the influences of partial volume effects within the masks,  $FA$  and  $MD$  values of the eroded masks (see Figure 36, right) are also calculated for all slices and the central slices (Table 9, right). Through the erosion the  $FA$  values of cortex are slightly decreased whereat medulla values are increased. Thus, a higher difference between the two tissue types is achieved. The standard deviation does not show huge differences between normal and eroded masks. The  $MD$  values are similar for cortex (normal mask:  $2.71 \cdot 10^{-3} \text{mm}^2/\text{s}$ ; eroded mask:  $2.72 \cdot 10^{-3} \text{mm}^2/\text{s}$ ) and medulla (normal mask:  $2.65 \cdot 10^{-3} \text{mm}^2/\text{s}$ ; eroded mask:  $2.63 \cdot 10^{-3} \text{mm}^2/\text{s}$ ). The  $MD$  values of the pelvis region show an increase from normal masks to eroded masks of 4.0% for all slices.

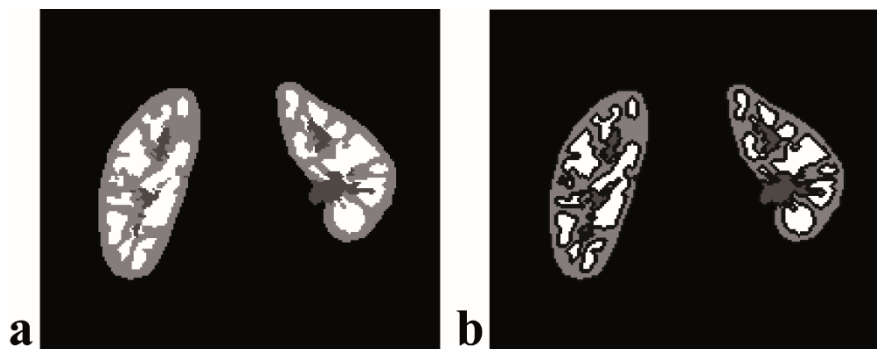


**Figure 36:** (a) Automatic segmented masks of entire kidney, cortex (bright grey), medulla (white) and pelvis (dark grey). (b) The black boundaries surrounding the areas result from the erosion of the masks.

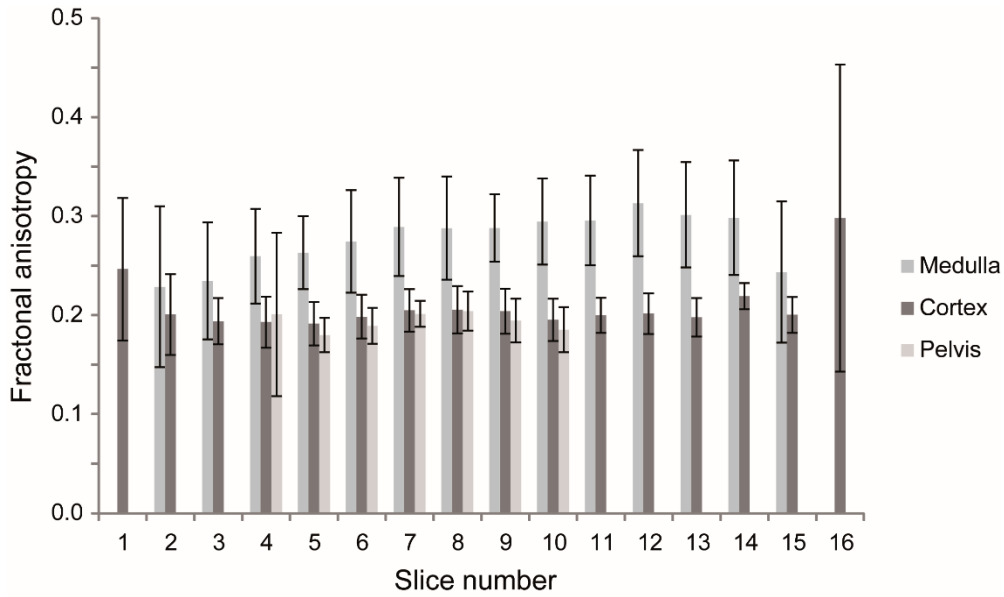


**Figure 37:** Mean FA values and their standard deviations over all subjects are illustrated for each slice. Both the cortex and the pelvis region show strong variations at the marginal slices and relatively low in the central slices. In contrast the medulla region shows also stronger variations in the central slices.

For two representative central slices a manual segmentation of the anatomical images in each subject was performed to show any failures of the automatic segmentation and their influences (Figure 37). The *FA* values for cortex ( $0.207 \pm 0.024$ ), medulla ( $0.282 \pm 0.043$ ) and pelvis ( $0.195 \pm 0.026$ ) show only small differences from the values calculated with automatic segmentation. The best agreement to the manual generated values is shown by the eroded automatically segmented masks over all slices.

#### *Multiband technique*

Qualitative comparison of the anatomical and distortion corrected echo-planar images of the kidneys showed clearly better agreement than uncorrected images. Figure 38 shows the segmentation masks superimposed to distortion corrected DTI image with standard (c) and multiband (d) technique. For both techniques the boundary slices show small deviations, while the central slices match well with the anatomical segmentation. Calculation of mean *FA* and *MD* values in the cortex/medulla area for standard and multiband acquisition results in higher *FA* values for MB technique. The *MD* values show a small decrease for MB technique (see Table 10).

## Results

**Table 10:** Comparison of fractional anisotropy ( $FA$ ) and mean diffusivity ( $MD$ ,  $10^{-3}$  mm<sup>2</sup>/s) values calculated for the cortical and medullary regions based on standard and multiband acquisition techniques.

	$FA_{\text{Standard}}$	$MD_{\text{Standard}}$	$FA_{\text{Multiband}}$	$MD_{\text{Multiband}}$
Cortex	$0.18 \pm 0.02$	$2.44 \pm 0.09$	$0.22 \pm 0.02$	$2.27 \pm 0.31$
Medulla	$0.23 \pm 0.04$	$2.47 \pm 0.15$	$0.29 \pm 0.04$	$2.25 \pm 0.40$

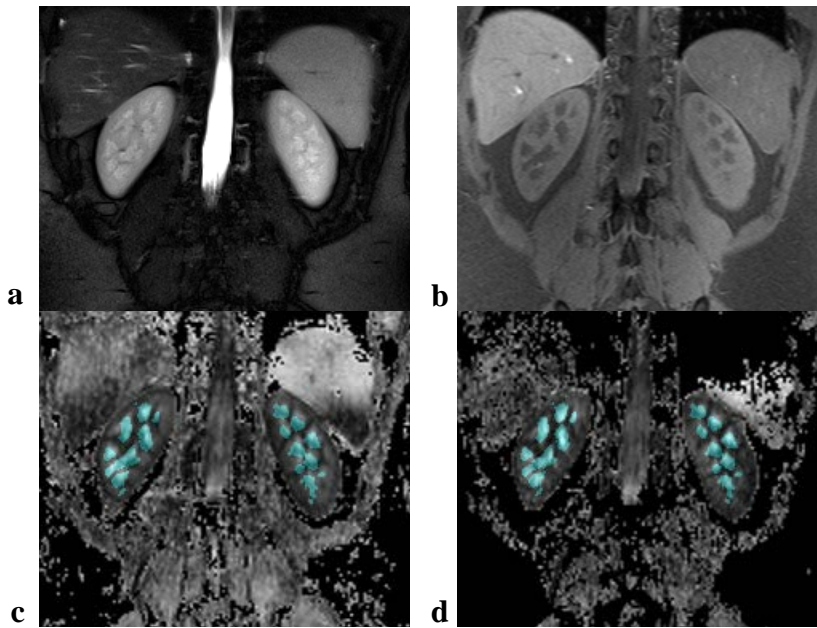


**Figure 38:** Segmentation of internal renal structures like cortex and medulla were performed from  $T_1$ -w (a) and  $T_2$ -w (b) MR images. The segmented masks were superimposed to the distortion corrected fractional anisotropy (FA) maps based on standard (c) and multiband (d) acquisition approaches.



## 5 Discussion

In this work a reliable method for detection of injected labeled stem cells over a time period of up to six months using high-resolution MR images has been presented. Not only the anatomy of the urethral sphincter but also the anatomy of the entire kidney, and their individual compartments were applied using adapted MR sequence protocols. An automatic segmentation algorithm based on non-contrast enhanced MR datasets of the kidney was implemented, which is important for later application in patients. Determination of the cortical, medullary and pelvic volumes and their ratio to the total kidney volume are essential biomarkers for the evaluation of specific diseases. Furthermore, the anatomical information was combined with functional data of the kidney. Based on the implemented distortion correction algorithm of abdominal DTI datasets both, fractional anisotropy and mean diffusivity values were determined and evaluated in the entire renal area.

### 5.1 Visualization of Urethral Sphincter

To the best of my knowledge this is the first study to visualize iron labeled MSCs within the urethral sphincter muscle using MRI. There is no profound therapy concept for the type of stress incontinence that is mainly caused by muscular weakness or dysfunction. This study was performed to evaluate the possibility of an effective cell labeling with SPIOs. The transurethral needle injection of human MSC into the bladder sphincter of female mini-pigs and their behavior within the tissue was controlled during a visual inspection using MRI.

The way in which the cells exhibit their therapeutic potential is still ambiguous. Differentiation and integration of the cells into the damaged tissue and into a paracrine function which induces local restoration are discussed as important mechanisms.

As differentiation, proliferation and integration of the cells are in close relation with cell division, duration of detectability plays an important role in displaying the fate of the cells. Roeder et al. [79] demonstrated retention of SPIO in MSC in collagenic sponges under “tissue” conditions for up to four weeks. Cell tracking in MRI has been presented

for up to three [80] or four months [81] with a decreasing signal loss over time. The detection of iron depots of different MSC in the rhabdosphincter in our approach was demonstrated for short (three weeks) as well as long-term (three and six months) animal groups. The iron depots in animals were detected even six months after injection. These results were confirmed by the histological staining and thus demonstrate a long traceability of the iron particles in the porcine urethral sphincter. So far, no statement can be made about the behavior of the cells in a damaged sphincter model. This should be investigated in further studies.

A potential problem is the comparability before and after injection in the same animal. The results of the long-term studies have only been compared to sham animals. Unfortunately, the repeated examination of a mini-pig is difficult due to anaesthetization. The animals show different response to anesthesia, so in some cases the animals died after the second or third anesthesia. For this reason sham operated animals were used as comparison. Another limitation is the high expenditure to examine a living animal several times.

The presented results are preliminary and show the behavior of the cells in an intact sphincter muscle. Moreover, even if there is evidence for iron deposition in the sphincter structure or in its direct vicinity, there is no proof of the viability of the cells by MRI. Since the detection of iron particles inside the sphincter muscle or even in surrounding tissue after six months was possible, the iron particles are probably embedded inside the cellular structure. Otherwise the SPIO particles would have been removed from the macrophages to the kidneys [82] or to surrounding lymph nodes, which has been observed in one MR measurement in our study. Amsalem et al. [83] have shown that after injection of iron labeled MSCs only macrophages were existent and have caused an inflammation of the heart. In the presented study, initial findings of histological analysis have shown that the located cell deposits did not consist of necrotic cells or macrophages. Further examinations should be performed to affirm these results in more detail; however, this study has its main focus on cell labeling and visualization of the labeled cells in MRI for several months.

Labeling with iron oxide nanoparticles allows detection of even small amount of cells. However, the size of signal voids depicted by MRI is not decisive for the number of cells

and is influenced by the characteristics of the surrounding tissue [84]. A substantial disadvantage of the negative contrast methods is that the signal behavior of some other materials (e.g. air or blood) is comparable to iron particles. Through the bladder catheter air bubbles have been partially embedded and were settled at the bladder neck. Like iron particles also air bubbles produce greater signal voids with increasing TE and thus hamper detection of labeled stem cells. Similarly, metallic abrasion of the needle could produce signal voids. However, this was tested in preliminary experiments and a metal abrasion was not detected in MRI with the commonly used needles. Due to natural occurring signal voids near the injection area, the detection of labeled stem cells is difficult. Another option displaying the signal voids is the positive contrast method by sequence preparation [85-88] or post processing [89-91].

Another important factor of cell detection is high spatial resolution of MR images. Our sequence has a resolution of  $0.4 \times 0.4 \times 2.4 \text{ mm}^3$ . However with this protocol it was not possible to separate the different muscle groups inside the thin structure (striated urogenital sphincter length  $13.7 \pm 3.9 \text{ mm}$  and thickness  $3.11 \pm 1.4 \text{ mm}$  [92]). For a differentiation or functional imaging a higher resolution and receive coils with higher sensitivity are probably necessary. Macura et al. [93], for example, used an intraurethral radiofrequency receive coil and could separate the urethra into smooth muscle and striated muscle with a resolution of  $0.2 \times 0.2 \times 2.5 \text{ mm}^3$  (1.5T). However, an intraurethral coil is not suitable for potential clinical application in humans.

The presented method has shown to be robust and sensitive to labeling and detection of MSC inside the porcine sphincter. Cell depots were detected in animals even six months after injection showing a good traceability. Translation of the proposed approach in clinical routine offers a non-invasive application technique for monitoring of morphological changes of the bladder sphincter. The localization of the labeled cells in MRI can be used as a follow-up control pre and post injection as well as a control for precise application of the cells.

## 5.2 Segmentation of the Internal Renal Structures

The presented technique provides a reliable automatic volumetric segmentation of the entire kidneys as well as renal cortex, medulla and pelvis in healthy volunteers based on non-contrast enhanced MR images. A good agreement between automatic and manual segmentation of the entire kidneys was obtained.

In recent years a number of studies of renal volumetric segmentation have been reported [4, 5, 24]. However, a straightforward comparison of their results is not always possible because some authors do not report the volume error values. The automatically calculated total kidney volume of  $405 \pm 71 \text{ cm}^3$  for both kidneys in healthy subjects agrees with the range of values reported in literature, e.g. Cheong et al. [94] have shown a single kidney volume of  $202 \pm 36 \text{ ml}$  for men and  $154 \pm 33 \text{ ml}$  for women.

Tang et al. [24] proposed an automatic renal segmentation algorithm using contrast enhanced MR images. They also compared their results to manual segmentation and calculated the overlap error. However, calculations have been performed with an equation that slightly differs from our definition of the volume overlap parameter. With an overlap of 66% for cortex and 76% for medulla we are in the same range. For the renal pelvis Tang et al. have reported reasonable agreement of automatic to manual segmentation of almost 90%.

Gloger et al. [29] recently presented a fully automated kidney segmentation algorithm of 3D non-contrast enhanced MR images acquired with a T<sub>1</sub>-w VIBE (volume interpolated breath-hold examination) sequence. They have reported a volume error of 7.5% for the right and 10.7% for the left kidney parenchyma, which is slightly worse compared to our results ( $ve \sim 5\%$ ). Furthermore, the results of our method (O) and Gloger et al. (G) for the overlap error (O: 20%, G: 25%), the volume overlap (O: 82%, G: 78%) as well as the dice coefficient (O: 90%, G: 86%) for the entire kidneys showed a high agreement to the manual segmentation. In contrast to Gloger et al. our algorithm also segments medulla and pelvis. To the best of our knowledge, none of the approaches in literature segmented the renal pelvis from native MR images. Additionally, our method mainly focused on the combination of adapted MR images with an ordinary post-processing algorithm.

Slice orientation proved to be of crucial influence on kidney segmentation in MRI. Axial slice orientation provides only minor partial volume effects in the kidneys [95], but a

higher number of slices have to be acquired covering the entire kidneys at a given slice thickness. This leads to an acquisition time potentially exceeding breath-hold capacity. Using coronal or sagittal slice orientation, breathing movements showed the lowest through-plane component [96]. Since sagittal slice orientation requires a high number of slices to cover both kidneys and additionally showed worse partial volume effects, coronal slice orientation was considered the best choice regarding both, measurement time and motion related artifacts.

Our comparison of different approaches for image registration revealed that a non-rigid registration achieves a better adaptation of the outer structures of the kidney. Unfortunately, medulla and pelvis regions showed strong deformations, which are not acceptable for accurate volumetry of internal renal structures. In contrast, the rigid registration seems to be clearly beneficial for outer as well as internal structures. The still existing mismatch of the outline registration leads to a higher overlap error of cortex, medulla and pelvis in our study.

The presented registration did not lead to a significant improvement in all cases. However, the values shown in Figure 27 are mean values from three different slices. Any improvement in the registration of T<sub>1</sub>- and T<sub>2</sub>-w images leads to better agreement of the automatically generated masks and contributes to a clearly differentiation of internal renal structures. Registration provides only a limited quality gain in compliant healthy volunteers, but seems crucial for examinations of patients who are expected to show sometimes a more pronounced mismatch between image series recorded in different breath-holds.

### *Study limitations*

Limited quality of segmentation evolves from the border slices. Partial volume effects [95, 97] due to finite slice thickness and overlapping with other organs lead to erroneous calculation of the volume. Since scan time is limited due to the breath-hold phase, relatively coarse voxel size of  $1.71 \times 1.37 \times 5 \text{ mm}^3$  was applied in our study. A higher image resolution would improve the volumetric results and diminish effects of the imprecise volumetric calculation of the first and last slices for both, manual and automatic segmentation.

A potential challenge that has to be accounted for is the separation of the spleen from the kidney. This problem mainly appears in skinny volunteers, as the fat deposit between spleen and kidney is almost completely lacking. Parts of the kidney might be artificially removed by the algorithm, but this part was recreated (at least for the most parts) afterwards by the snake algorithm automatically.

Another limitation is the correct determination of the renal pelvis. The pelvis size depends on the fluid status of each volunteer. However, this effect was not considered in this study. The overlap errors regarding the medulla and particularly renal pelvis are more pronounced than for the renal cortex. The reason for this is an increase of the volume error due to geometrical features (e.g. large surface) in those compartments. It is well-known that correct determination of the border of the pelvis in native MR images is critical. So the volume error of more than 17% is in a reasonable range but still improvable. Some studies reported in literature using administration of contrast agent [24] have shown better results. However contrast agent is not well compatible for patients with kidney diseases, therefore the presented approach was developed for examinations without administration of contrast agent.

Proposed sequence types and parameters can also be applied for studies on other MR scanners operating at 1.5T (especially if the used receiver coils have similar sensitivity and characteristics). Suitable threshold values should be adapted, if the measurement setup is changed, since the measured signal intensity depends on the hardware and software of the used MR unit. Optimization of the acquisition parameters was performed at a field strength of 1.5T. A change in field strength usually results in modified tissue contrast. Relaxation times of tissue do not change linearly with field strength and therefore sequence parameters should be optimized again, if measurements for renal segmentation are planned at different field strength (e.g. 3 Tesla).

The presented segmentation algorithm has been proved on healthy volunteers. Lee et al. recently reported that in some renal diseases the corticomedullary contrast is modified or even decreased [98]. Similar to our approach, T<sub>1</sub>-w images were used for the differentiation of cortex and medulla. The reliability of the proposed algorithm in patients has to be determined, especially under conditions with a weakened contrast between cortex and medulla. In our work we have optimized parameters of T<sub>1</sub>-w sequences regarding the relevant contrast between medulla and cortex. With a

contrast to noise ratio of approximately 13 between medulla and cortex obtained in healthy subjects, some tolerances remain even in cases with slightly changed tissue properties. The proposed segmentation procedure is expected to work quite well in cases with normal signal characteristics of the renal compartments, but changes in respective volumes. Renal diseases, leading to strong changes in signal of T<sub>1</sub>- and T<sub>2</sub>-w MRI (e.g., tumors, cysts), were not yet included for volume quantification using the given approach.

In conclusion, the combination of adapted MR images, image registration and automatic segmentation provides reliable and repeatable volumetric results of the entire kidney, renal cortex, medulla and pelvis without applying contrast agent. With a total image post-processing time of approximately 16 minutes, including registration and segmentation, the presented method is much faster than manual segmentation.

Translating the proposed work to clinical routine offers a non-invasive approach for assessment and monitoring of morphological changes by calculating the ratio between cortex and the entire kidney volume. This is of special interest since the cortical volume is known to decrease over time in some patients with affected kidneys [99, 100].

### 5.3 Characterization of Distortion Corrected Images from DTI

In this part of the thesis a reliable quantification of mean diffusivity and fractional anisotropy in distortion corrected EPI images in healthy kidneys was developed. It has been demonstrated that DTI values of the internal renal structures cortex, medulla and pelvis were accurately determined by fusion of an automatic volumetric segmentation, based on highly resolved anatomical MR images, and distortion corrected EPI images.

Successful distortion correction was demonstrated by comparison of the automatically generated masks from anatomical images and the manually drawn masks on *MD* maps. Due to the different breathing related positions of the kidney it is not self-evident that the distortion correction method works robust in the abdomen, therefore, first the distortion correction has been verified by a manual segmentation of the entire kidney. A good agreement between automatic and manual segmentation of the entire kidneys was shown using similarity parameters *ve*, *oe*, *vo* and *dice* coefficient. Gloger et al. [29] have shown similar values comparing manual and automatic segmentation results, like *ve* (0.075-0.107), *oe* (0.198-0.212), *vo* (0.817-0.820) and *dice* (0.893-0.903), which are in a good correspondence to ours.

Inferior quality of automatic segmentation evolves in marginal slices. Partial volume effects [97, 95] due to finite slice thickness and overlapping with other organs lead to erroneous calculation of the segmented masks. Furthermore, the manual segmentation in the *MD* maps was very difficult because of blurred boundary lines of the kidney and surrounding tissue. Therefore, to mitigate the influence of peripheral slices, the calculation of the *FA* and *MD* values was limited on the central slices for the second evaluation. The number of central slices was chosen arbitrarily to incorporate the largest possible volume for evaluation. However, no major differences between both approaches were found in cortex and medulla region, suggesting that marginal slices only have a small effect on the results.

The presented segmentation algorithm has been proved only on healthy volunteers. Slight motion artifacts at the edge of the kidney in EPI lead to blurred edges of the borders of the kidney in *MD* and *FA* maps, particularly indicating potential problems in patients with

irregular breathing. Motion artifacts were minimized by individual registration steps but not completely eliminated. This effect is also reduced by eroding the masks or excluding marginal slices, eliminating the border values from rating of averaged *MD* and *FA* values. Additional misalignments, possibly caused by eddy currents, were reduced using bipolar diffusion gradient schemes [74]. An alternative approach would be a simple non-rigid registration which allows an agreement of the entire kidneys in a very short time, but that's not given for the internal renal structures cortex and medulla.

Fusion of high-resolution anatomic segmented masks with distortion corrected diffusion-weighted images showed *MD* values of cortex and medulla in good concordance with literature. Notohamiprodjo et al. have shown *MD* values in the range of  $2.55\text{-}2.79\cdot 10^{-3}$   $\text{mm}^2/\text{s}$  for cortex at 3T, which is comparable to our study ( $2.68\cdot 10^{-3}$   $\text{mm}^2/\text{s}$ ) [101]. The number and level of the b-values has to be taken into account for the comparison with literature, because *MD* values vary with the selected b-values [102]. The mean *FA* value of the medulla (0.29), resulting from the anatomical segmentation, is smaller than values reported in literature (approx. 0.4), whereas the mean cortical *FA* value of 0.20 is in the range of published values (0.19 to 0.23) [101]. This is attributable to the fact that most evaluation methods in literature used regions of interest drawn in the brightest areas of the DTI parameter map or threshold-based methods for separation of cortex and medulla [101, 103]. This assumption was tested and verified by ROI analysis in our data: the six ROIs were placed directly into the brightest visible medullary areas of the *FA* map and resulted in similar values (cortex: 0.20, medulla: 0.45) to those found in literature. An advantage of the presented algorithm is a slice-wise quantification of the entire kidney structures, whereby local renal diseases, such as cysts or partial necrosis, could be included by an expanded segmentation.

For this study, the phase-encoding direction was chosen to H>>F because image quality was found superior when compared to usual encoding R>>L. Using 30 different diffusion-sensitizing gradients directions this method leads to an acquisition time of about three to four minutes for one EPI dataset, which should be shortened for a clinical application. Fewer directions would reduce acquisition time at the cost of image quality [102, 104]. Another possibility to reduce measurement time is using simultaneous multi-

slice (SMS) imaging technique [105-107], which allows reducing the repetition time by the number of simultaneously excited slices.

### *Multiband acquisition*

It was found that *MD* and *FA* values were accurately determined in specific areas of distortion corrected images by renal segmentation for multiband and standard EPI. Slight displacements by respiratory artifacts were eliminated by further registration to anatomical images. A benefit of acquisition time reduction by factor two with good accordance to standard values is a distinct advantage of these results acquired by multiband technique. This advantage can be spent to increase the resolution of DTI.

## 6 Outlook and Future Work

The following section will present the current status of development of the presented studies as well as provide ideas for continuing research with an emphasis on transferability to clinical routine.

### *Transfer from pre-clinical to clinical application*

First images of the female urethra in human subjects (Figure 39) showed a high anatomical resolution for reproducible localization of anatomical landmarks. Therefore a precise adjustment of the slice positioning orthogonal to the urethral course is possible. This allows the determination of the muscular thickness, as well as an estimation of the sphincter length. Since the anatomical delineation only provides information about length and thickness of the sphincter muscle as well as on the position of the urethra in relation to the anatomical surrounding tissue, other measuring methods should be taken into account for further analysis.

### *Multi-parametric and multi-modality methods*

For evaluation of the function and regeneration of the muscle sphincter, high resolution images should be combined with functional maps in new studies.

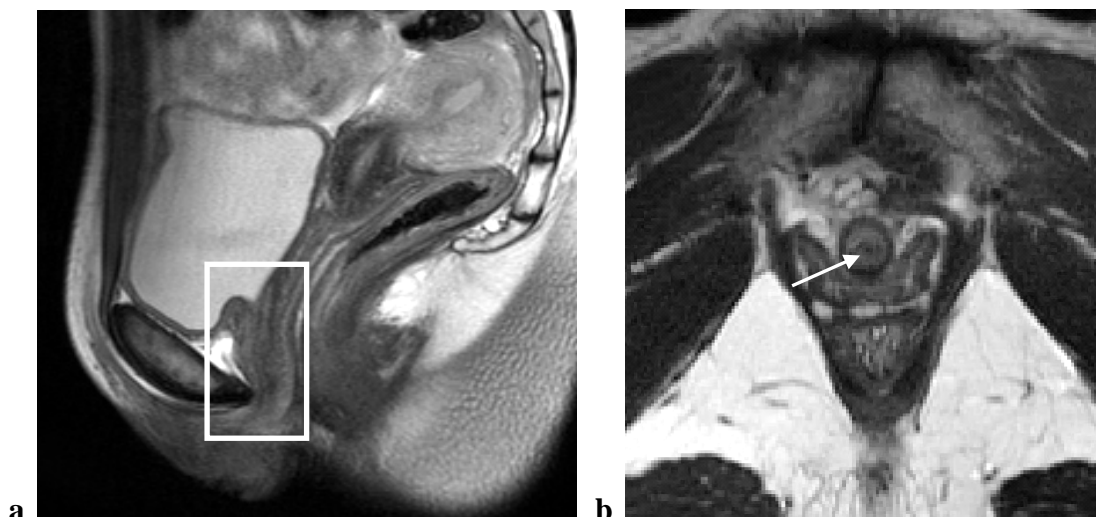


**Figure 39:** Sagittal (a) and axial (b)  $T_2$ -w TSE image of a female volunteer at 3 Tesla. The right image

shows a zoomed axial view of the urethra (white arrow) and allows a classification of the individual muscles and the determination of the urethral thickness.

DTI is a good way representing the fiber bundles and therefore the functionality of the tissue. Zijta et al. [108] have shown the feasibility of fibre tractography of the female pelvic floor using DTI. However it is challenging to perform DTI of the sphincter muscle because existing functional imaging techniques in MRI provide isotropic spatial resolution of  $1 \text{ mm}^3$  whereas the course of fiber bundles is not represented adequately at a sphincter thickness of 2 mm.

Anatomical MR images are also useful in combination with other modalities like histological images (as already shown in this work) or High Definition Urethral Pressure Profile (HD-UPP) data [109]. Combining MRI and HD-UPP as multi-modality fusion (Figure 40) generates additional information about pathological conditions on pressure distribution.

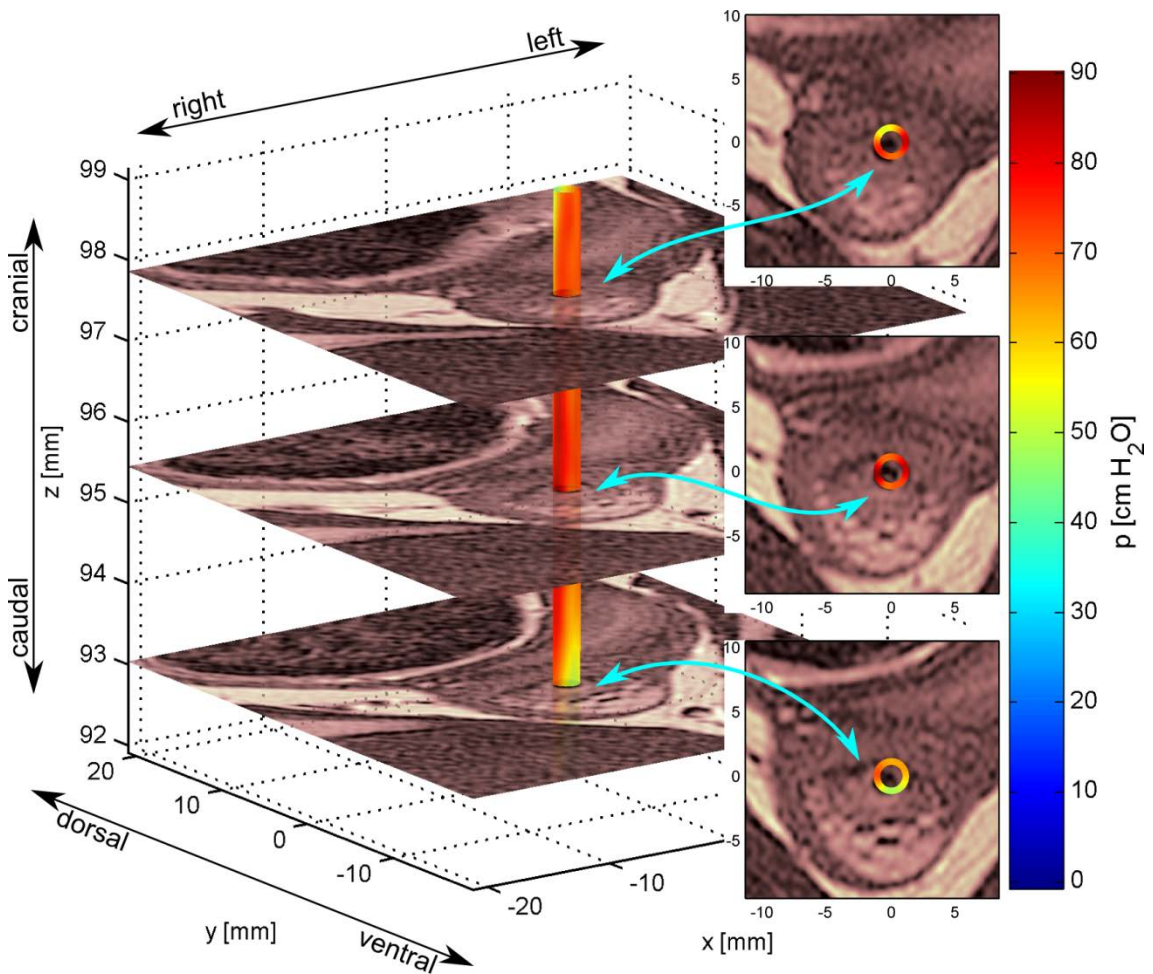


**Figure 40:** Fusion of anatomical MRI data and Urethral Pressure Profile (HD-UPP) data of a minipig. The insets show the center section of the respective MRI slices and the angular pressure distribution in the urethra. [109]

Initial experiments about fusion of urethral pressure data from HD-UPP and 3D morphological MRI data showed the potential to improve the diagnostic quality and treatment for follow-up examinations. The information of the location of the highest pressure and thus the location of the sphincter muscle supports the accuracy of the injection position. Not only results from anatomical proportions but also in combination with the increase of the pressure profile show a positive reaction on stem cell based treatments. This establishes the opportunity for a better diagnostic and therapy planning.

### *Application of segmentation algorithm in patient datasets*

The implementation of the described segmentation algorithm has been applied only on healthy subjects yet. Therefore, a continuative project is planned including pathological changes. The aim of the intended project is to evaluate the developed segmentation algorithm with patient data (with diabetic background) in order to examine the generated volumetric proportions in comparison with the disease. The amount of hilum fat was determined with respect to the total amount of renal fat. The advanced segmentation algorithm introduced in this thesis was adapted to these MR images, also acquired with a magnetic field strength of 3T. To simplify the application of the program and the evaluation of several hundred measurements, the program was implemented in a user-friendly graphical user interface (GUI) in MatLab. This GUI allows displaying the images and the resulting segmented binary masks. After visual inspection of the masks, manual adjustments are possible if necessary. Then, the resulting values can be set in relation to other collected data, e.g. blood parameters, obtaining an advanced knowledge of the disease.



## 7 Abstract

The aim of this thesis was the examination and delineation of single urogenital compartments using high-resolution magnetic resonance imaging (MRI). For the urethral sphincter regeneration a porcine model served to visualize iron labeled stem cells using high resolution MR datasets. Localization and adaptation of muscle tissue after cell injection was examined up to six months. For this purpose, a robust and sensitive non-invasive method was developed obtaining an essential understanding of the biological effects of the sphincter and thus developing new cell-based therapies.

Investigating further compartments of the urogenital tract, the renal structures cortex, medulla and pelvis were evaluated in healthy subjects using non-contrast enhanced high-resolution MRI. With adapted MR sequence protocols the individual renal structures were segmented automatically by a self-written algorithm. Compared to manual segmentation, the calculated coefficients for the entire kidneys showed a high agreement to the automatic segmentation. Additionally, the presented algorithm also segmented medulla and pelvis. To the best of our knowledge, none of the approaches in literature segmented the renal pelvis from native MR images. The combination of adapted MR images, image registration and automatic segmentation provides reliable and repeatable volumetric results of the entire kidney and their renal structures without applying contrast agent. Translating the developed algorithm to clinical routine offers a non-invasive approach for assessment and monitoring of morphological changes.

For further applications the segmented areas were superimposed to distortion corrected functional diffusion datasets in order to obtain region based values of fractional anisotropy (*FA*) and mean diffusivity (*MD*). For distortion correction the reversed gradient method was used. Successful distortion correction was demonstrated by comparison of automatically generated masks from anatomical images and manually drawn masks on *MD* maps. Manual segmentation in *MD* maps is very difficult because of blurred boundary lines of the kidney and surrounding tissue. Fusion of high-resolution anatomic segmented masks with distortion corrected diffusion-weighted images showed advantages for a reliable evaluation. *MD* values of cortex and medulla as well as cortical *FA* values were in good concordance with literature. The smaller medullary *FA* values

were attributable to the fact that most evaluation methods in literature used regions of interest drawn in the brightest areas of the DTI parameter map. An advantage of the presented algorithm is a slice-wise quantification of the entire kidney structures, whereby local renal diseases, such as cysts or partial necrosis, could be included by an expanded segmentation. The ratios between the individual volumes within the kidney, taking into account the functionality of these regions, provide further knowledge in renal diagnostics.

## 8 Zusammenfassung

Ziel dieser Arbeit war die Untersuchung und Darstellbarkeit einzelner Kompartimente des Urogenitaltrakts mittels hochauflösender Magnetresonanztomografie (MRT). Im Kontext der Schließmuskelregeneration wurde mit Hilfe der MRT der urethrale Schließmuskel eines Tiermodells visualisiert, wodurch im zeitlichen Verlauf die Lokalisierung und Anpassungsfähigkeit des Muskelgewebes nach Injektion von markierten Stammzellen untersucht werden konnte. Hierfür wurde eine robuste, sensitive und nicht-invasive Methode angewendet, um ein essentielles Verständnis der biologischen Effekte im Sphinkter zu erhalten und somit neue zellbasierte Therapien zu entwickeln.

Zur Untersuchung weiterer Kompartimente des Urogenitaltrakts wurden die renalen Strukturen Cortex, Medulla und Pelvis ohne die Verwendung von Kontrastmittel anhand hochauflösender MR-Methoden im Probanden evaluiert. Unter Zuhilfenahme optimierter MR-Sequenzen konnten die einzelnen Kompartimente klar strukturiert und durch einen selbstentwickelten automatischen Algorithmus segmentiert werden. Im Vergleich zur manuellen Segmentierung zeigten die berechneten Koeffizienten eine hohe Übereinstimmung zur automatischen Segmentierung der gesamten Nierenregion. Zusätzlich wurde durch den vorgestellten Algorithmus sowohl die Medulla als auch das Nierenbecken automatisch segmentiert. Bisher sind keine Ansätze aus der Literatur bekannt, die das Nierenbecken aus nativen MR-Bildern segmentierten und evaluierten. Die Kombination aus optimierten MR-Bildern, Bildregistrierung und automatischer Segmentierung liefert zuverlässige und wiederholbare Ergebnisse der Volumenbestimmung der gesamten Niere und der renalen Strukturen ohne Zuhilfenahme von Kontrastmittel. Bei einer möglichen Übertragung des entwickelten Algorithmus in die klinische Routine eröffnen sich neue nicht-invasive Möglichkeiten zur Bewertung und Überwachung morphologischer Veränderungen.

Zur weiteren Anwendung wurden die segmentierten Areale auf entzerrungskorrigierte funktionelle Diffusionsdatensätze überlagert, um eine regionenbasierte Darstellung der fraktionellen Anisotropie (*FA*) und der mittleren Diffusivität (*MD*) zu erhalten. Die

Durchführung der Verzerrungskorrektur wurde anhand der „reversed gradient“ Methode verwirklicht. Die erfolgreiche Verzerrungskorrektur konnte durch einen Vergleich der manuellen Segmentierung der *MD* Karten und den automatisch generierten Masken aus den Anatomiedatensätzen dargelegt werden. Die manuelle Segmentierung ist sehr zeitaufwändig und auf Grund der unscharfen Außenkontur der Niere in den *MD* Karten äußerst schwierig zu realisieren. Daher erbringt die Fusion von hochaufgelösten, anatomisch segmentierten Masken mit verzerrungskorrigierten funktionellen Daten Vorteile für eine zuverlässige Auswertung. Die berechneten funktionellen Werte zeigten eine gute Übereinstimmung mit Literaturwerten. Lediglich verringerte medullare *FA*-Werte sind auf die Tatsache zurückzuführen, dass die bisherigen Bewertungsmethoden nur Regionen aus den hellsten Bereichen der funktionellen Bilder mit einbezogen haben. Ein weiterer Vorteil des entwickelten Algorithmus ist somit eine schichtweise Quantifizierung der gesamten Nierenstrukturen, wobei lokale Nierenerkrankungen, wie Zysten oder eine partielle Nekrose, durch eine erweiterte Segmentierung mit in die Beurteilung einbezogen werden können. Die Verhältnisse der Volumina innerhalb der Niere, unter Berücksichtigung der Funktionalität der einzelnen Regionen, ermöglichen nun weitere Erkenntnisse in der Nierendiagnostik.

## 9 References

1. Eberli D, Aboushwareb T, Soker S, Yoo JJ, Atala A (2012) Muscle precursor cells for the restoration of irreversibly damaged sphincter function. *Cell transplantation* 21 (9):2089-2098. doi:10.3727/096368911X623835
2. Goldman HB, Sievert KD, Damaser MS (2012) Will we ever use stem cells for the treatment of SUI? ICI-RS 2011. *Neurourology and urodynamics* 31 (3):386-389. doi:10.1002/nau.22217
3. Gunetti M, Tomasi S, Giammo A, Boido M, Rustichelli D, Mareschi K, Errichiello E, Parola M, Ferrero I, Fagioli F, Vercelli A, Carone R (2012) Myogenic potential of whole bone marrow mesenchymal stem cells in vitro and in vivo for usage in urinary incontinence. *PloS one* 7 (9):e45538. doi:10.1371/journal.pone.0045538
4. Jones RA, Easley K, Little SB, Scherz H, Kirsch AJ, Grattan-Smith JD (2005) Dynamic contrast-enhanced MR urography in the evaluation of pediatric hydronephrosis: Part 1, functional assessment. *AJR American journal of roentgenology* 185 (6):1598-1607. doi:10.2214/AJR.04.1540
5. Karstoft K, Lodrup AB, Dissing TH, Sorensen TS, Nyengaard JR, Pedersen M (2007) Different strategies for MRI measurements of renal cortical volume. *Journal of magnetic resonance imaging : JMRI* 26 (6):1564-1571. doi:10.1002/jmri.21121
6. Graser A, Johnson TR, Chandarana H, Macari M (2009) Dual energy CT: preliminary observations and potential clinical applications in the abdomen. *European radiology* 19 (1):13-23. doi:10.1007/s00330-008-1122-7
7. Johnson TR, Krauss B, Sedlmair M, Grasruck M, Bruder H, Morhard D, Fink C, Weckbach S, Lenhard M, Schmidt B, Flohr T, Reiser MF, Becker CR (2007) Material differentiation by dual energy CT: initial experience. *European radiology* 17 (6):1510-1517. doi:10.1007/s00330-006-0517-6
8. Kaza RK, Platt JF, Megibow AJ (2013) Dual-energy CT of the urinary tract. *Abdominal imaging* 38 (1):167-179. doi:10.1007/s00261-012-9901-7
9. Mileto A, Marin D, Nelson RC, Ascenti G, Boll DT (2014) Dual energy MDCT assessment of renal lesions: an overview. *European radiology* 24 (2):353-362. doi:10.1007/s00330-013-3030-8
10. Bakker J, Olree M, Kaatee R, de Lange EE, Beek FJ (1998) In vitro measurement of kidney size: comparison of ultrasonography and MRI. *Ultrasound in medicine & biology* 24 (5):683-688
11. Bakker J, Olree M, Kaatee R, de Lange EE, Moons KG, Beutler JJ, Beek FJ (1999) Renal volume measurements: accuracy and repeatability of US compared with that of MR imaging. *Radiology* 211 (3):623-628. doi:10.1148/radiology.211.3.r99jn19623
12. Le Bihan D, Mangin JF, Poupon C, Clark CA, Pappata S, Molko N, Chabriat H (2001) Diffusion tensor imaging: concepts and applications. *Journal of magnetic resonance imaging : JMRI* 13 (4):534-546
13. Mannelli L, Maki JH, Osman SF, Chandarana H, Lomas DJ, Shuman WP, Linnau KF, Green DE, Laffi G, Moshiri M (2012) Noncontrast functional MRI of the kidneys. *Current urology reports* 13 (1):99-107. doi:10.1007/s11934-011-0229-6
14. Chevaillier B, Mandry D, Ponvianne Y, Collette JL, Claudon M, Pietquin O (2008) Functional semi-automated segmentation of renal DCE-MRI sequences using a growing neural gas algorithm. Paper presented at the 16th European Signal Processing Conference (EUSIPCO), Lausanne

15. Li S, Zollner FG, Merrem AD, Peng Y, Roervik J, Lundervold A, Schad LR (2012) Wavelet-based segmentation of renal compartments in DCE-MRI of human kidney: initial results in patients and healthy volunteers. *Computerized medical imaging and graphics : the official journal of the Computerized Medical Imaging Society* 36 (2):108-118. doi:10.1016/j.compmedimag.2011.06.005
16. Grenier N, Basseau F, Ries M, Tyndal B, Jones R, Moonen C (2003) Functional MRI of the kidney. *Abdominal imaging* 28 (2):164-175. doi:10.1007/s00261-001-0183-8
17. Coulam CH, Bouley DM, Sommer FG (2002) Measurement of renal volumes with contrast-enhanced MRI. *Journal of magnetic resonance imaging : JMRI* 15 (2):174-179
18. de Bazelaire CM, Duhamel GD, Rofsky NM, Alsop DC (2004) MR imaging relaxation times of abdominal and pelvic tissues measured in vivo at 3.0 T: preliminary results. *Radiology* 230 (3):652-659. doi:10.1148/radiol.2303021331
19. Di Leo G, Di Terlizzi F, Flor N, Morganti A, Sardanelli F (2011) Measurement of renal volume using respiratory-gated MRI in subjects without known kidney disease: intraobserver, interobserver, and interstudy reproducibility. *European journal of radiology* 80 (3):e212-216. doi:10.1016/j.ejrad.2010.09.005
20. Widmark JM (2007) Imaging-related medications: a class overview. *Proceedings* 20 (4):408-417
21. Cohen BA, Barash I, Kim DC, Sanger MD, Babb JS, Chandarana H (2012) Intraobserver and interobserver variability of renal volume measurements in polycystic kidney disease using a semiautomated MR segmentation algorithm. *AJR American journal of roentgenology* 199 (2):387-393. doi:10.2214/AJR.11.8043
22. Kanki A, Ito K, Tamada T, Noda Y, Yamamoto A, Tanimoto D, Sato T, Higaki A (2013) Corticomedullary differentiation of the kidney: evaluation with noncontrast-enhanced steady-state free precession (SSFP) MRI with time-spatial labeling inversion pulse (time-SLIP). *Journal of magnetic resonance imaging : JMRI* 37 (5):1178-1181. doi:10.1002/jmri.23909
23. Borgelt C, Timm H, Kruse R (2000) Using fuzzy clustering to improve naive bayes classifiers and probabilistic networks. Paper presented at the The Ninth IEEE International Conference San Antonio, TX,
24. Tang Y, Jackson HA, De Filippo RE, Nelson MD, Moats RA (2010) Automatic renal segmentation applied in pediatric MR urography. *International J Intell Inf Process* 1 (1):12-19
25. Sun Y, Moura J, Yang DY, Ye Q, Ho C (2002) Kidney segmentation in MRI sequences using temporal dynamics. *IEEE Int Symp Biomed Imag* 98-101
26. He L, Peng Z, Everding B, Wang X, Han CY, Weiss KL, Wee WG (2008) A comparative study of deformable contour methods on medical image segmentation. *Image Vis Computing* 26:141-163
27. Vivier PH, Dolores M, Gardin I, Zhang P, Petitjean C, Dacher JN (2008) In vitro assessment of a 3D segmentation algorithm based on the belief functions theory in calculating renal volumes by MRI. *AJR American journal of roentgenology* 191 (3):W127-134. doi:10.2214/AJR.07.3063
28. Gaudio C, Clementi V, Busato F, Corcioni B, Orrei MG, Ferramosca E, Fabbri E, Berardi P, Santoro A, Golfieri R (2013) Diffusion tensor imaging and tractography of the kidneys: assessment of chronic parenchymal diseases. *European radiology* 23 (6):1678-1685. doi:10.1007/s00330-012-2749-y
29. Gloger O, Tonies KD, Liebscher V, Kugelmann B, Laqua R, Volzke H (2012) Prior shape level set segmentation on multistep generated probability maps of MR datasets for

- fully automatic kidney parenchyma volumetry. *IEEE transactions on medical imaging* 31 (2):312-325. doi:10.1109/TMI.2011.2168609
30. Jezzard P, Balaban RS (1995) Correction for geometric distortion in echo planar images from B<sub>0</sub> field variations. *Magnetic resonance in medicine* 34 (1):65-73
31. Studholme C, Constable RT, Duncan JS (2000) Accurate alignment of functional EPI data to anatomical MRI using a physics-based distortion model. *IEEE transactions on medical imaging* 19 (11):1115-1127. doi:10.1109/42.896788
32. Andersson JL, Skare S, Ashburner J (2003) How to correct susceptibility distortions in spin-echo echo-planar images: application to diffusion tensor imaging. *NeuroImage* 20 (2):870-888. doi:10.1016/S1053-8119(03)00336-7
33. Morgan PS, Bowtell RW, McIntyre DJ, Worthington BS (2004) Correction of spatial distortion in EPI due to inhomogeneous static magnetic fields using the reversed gradient method. *Journal of magnetic resonance imaging : JMRI* 19 (4):499-507. doi:10.1002/jmri.20032
34. Lauterbur PC (1973) Image Formation by Induced Local Interactions - Examples Employing Nuclear Magnetic-Resonance. *Nature* 242 (5394):190-191. doi:10.1038/242190a0
35. Mansfield P, Grannell PK (1973) Nmr Diffraction in Solids. *J Phys C Solid State* 6 (22):L422-L426. doi:10.1088/0022-3719/6/22/007
36. Bloch F (1946) Nuclear induction. *Physical Review* 70:460-474
37. Purcell E, Torrey H, Pound R (1946) Resonance absorption by nuclear magnetic moments in a solid. *Physical Review* 69:37-38
38. Haken H, Wolf H (2000) *Atom- und Quantenphysik: Einführung in die experimentellen und theoretischen Grundlagen*. Springer, Berlin
39. Huettel S, Song A, McCarthy G (2004) *Functional Magnetic Resonance Imaging*. Sinauer Associates Inc, Sunderland
40. de Graaf R (2007) *In vivo NMR Spectroscopy - Principles and Techniques*, vol 2nd Edition. John Wiley & sons Ltd, England
41. Brown R, Cheng Y, Haake E, Thompson M, Venkatesan R (1999) *Magnetic resonance imaging - Physical principles and sequence design*, vol 2nd Edition. John Wiley & Sons, Inc., Hoboken, New Jersey
42. Bloch F (1946) Nuclear induction. *Physical Review* 70:460-474
43. Twieg DB (1983) The K-Trajectory Formulation of the Nmr Imaging Process with Applications in Analysis and Synthesis of Imaging Methods. *Med Phys* 10 (5):610-621. doi:10.1118/1.595331
44. Ljunggren S (1983) A Simple Graphical Representation of Fourier-Based Imaging Methods. *Journal of magnetic resonance* 54 (2):338-343. doi:10.1016/0022-2364(83)90060-4
45. Oppelt A (2005) *Imaging Systems for Medical Diagnostics*. Publicis: Corporate Publishing, Erlangen
46. Hennig J, Nauwerth A, Friedburg H, Ratzel D (1984) [New rapid imaging procedure for nuclear spin tomography]. *Der Radiologe* 24 (12):579-580
47. Bernstein M, King K, Zhou X (2004) *Handbook of MRI Pulse Sequences*. Elsevier, London
48. Stehling MJ, Howseman AM, Ordidge RJ, Chapman B, Turner R, Coxon R, Glover P, Mansfield P, Coupland RE (1989) Whole-body echo-planar MR imaging at 0.5 T. *Radiology* 170 (1 Pt 1):257-263. doi:10.1148/radiology.170.1.2909106

- 
49. Feinberg DA, Turner R, Jakab PD, von Kienlin M (1990) Echo-planar imaging with asymmetric gradient modulation and inner-volume excitation. *Magnetic resonance in medicine* 13 (1):162-169
  50. Mansfield P (1984) Real-time echo-planar imaging by NMR. *British medical bulletin* 40 (2):187-190
  51. Koh DM, Thoeny HC, (editors) (2010) *Diffusion weighted MR imaging Applications in the Body*. Springer Verlag
  52. Steidle G (2012) *Magnetic Resonance Techniques for Sensitive Assessment of Microscopic Properties of Muscular and Adipose Tissue*. Eberhard Karls Universität Tübingen, Tübingen
  53. Sullivan EV, Pfefferbaum A (2006) Diffusion tensor imaging and aging. *Neuroscience and biobehavioral reviews* 30 (6):749-761. doi:10.1016/j.neubiorev.2006.06.002
  54. Maintz JB, Viergever MA (1998) A survey of medical image registration. *Medical image analysis* 2 (1):1-36
  55. Haber E, Modersitzki J (2004) Numerical methods for volume preserving image registration. *Inverse problems* 20 (5):1621-1638. doi:Pii S0266-5611(04)76392-3 10.1088/0266-5611/20/5/018
  56. Hill DL, Batchelor PG, Holden M, Hawkes DJ (2001) Medical image registration. *Physics in medicine and biology* 46 (3):R1-45
  57. Zitova B, Flusser J (2003) Image registration methods: a survey. *Image Vision Comput* 21 (11):977-1000. doi:10.1016/S0262-8856(03)00137-9
  58. Klein S, Staring M, Murphy K, Viergever MA, Pluim JP (2010) elastix: a toolbox for intensity-based medical image registration. *IEEE transactions on medical imaging* 29 (1):196-205. doi:10.1109/TMI.2009.2035616
  59. Shamonin DP, Bron EE, Lelieveldt BP, Smits M, Klein S, Staring M, Alzheimer's Disease Neuroimaging I (2013) Fast parallel image registration on CPU and GPU for diagnostic classification of Alzheimer's disease. *Frontiers in neuroinformatics* 7:50. doi:10.3389/fninf.2013.00050
  60. Conzales R, Woods R (2008) *Digital image processing*, vol 3rd edition. Pearson Education, Inc., New Jersey
  61. Birkenfellner W (2011) *Applied medical image processing*. Taylor and Francis Group, LLC, Boca Raton, FL
  62. Otsu N (1979) Threshold Selection Method from Gray-Level Histograms. *Ieee T Syst Man Cyb* 9 (1):62-66
  63. Seber G (1984) *Multivariate Observations*. John Wiley & Sons, Inc, Hoboken, NJ
  64. Spath H (1985) *Cluster Dissection and Analysis: Theory, FORTRAN Programs, Examples*. Halsted Press, New York
  65. Bezdek JC (1981) *Pattern Recognition with Fuzzy Objective Function Algorithms*. Plenum Press, New York
  66. Dunn JC (1973) A Fuzzy Relative of the ISODATA Process and Its Use in Detecting Compact Well-Separated Clusters. *J Cybernetics* 3 (3):32-57
  67. Kass M, Witkin A, Terzopoulos D (1988) Snakes: Active contour models. *International Journal of Computer Vision* 1 (4):321-331
  68. Osher S, Paragios N, editors. (2003) *Geometric level set methods in imaging, vision, and graphics*. Springer
  69. Putz R, Pabst R (2000) *Sobotta- Atlas der Anatomie des Menschen- Band 2 Rumpf, Eingeweide, untere Extremitäten*, vol 21. Urban & Fischer Verlag, Munich/Jena

- 
70. Clapp W (2009) Renal Anatomy. In: Zhou XJ, Laszik Z, Nadasdy T, D'Agati VD, Silva FG, eds. *Silva's Diagnostic Renal Pathology*. *Silva's Diagnostic Renal Pathology*. Cambridge University Press, New York
71. Will S, Martirosian P, Eibofner F, Schick F, Bantleon R, Vaegler M, Grozinger G, Claussen CD, Kramer U, Schmehl J (2015) Viability and MR detectability of iron labeled mesenchymal stem cells used for endoscopic injection into the porcine urethral sphincter. *NMR in biomedicine* 28 (8):1049-1058. doi:10.1002/nbm.3339
72. Will S, Martirosian P, Wurslin C, Schick F (2014) Automated segmentation and volumetric analysis of renal cortex, medulla, and pelvis based on non-contrast-enhanced T1- and T2-weighted MR images. *Magma* 27 (5):445-454. doi:10.1007/s10334-014-0429-4
73. Zollner FG, Svarstad E, Munthe-Kaas AZ, Schad LR, Lundervold A, Rorvik J (2012) Assessment of kidney volumes from MRI: acquisition and segmentation techniques. *AJR American journal of roentgenology* 199 (5):1060-1069. doi:10.2214/AJR.12.8657
74. Reese TG, Heid O, Weisskoff RM, Wedeen VJ (2003) Reduction of eddy-current-induced distortion in diffusion MRI using a twice-refocused spin echo. *Magnetic resonance in medicine* 49 (1):177-182. doi:10.1002/mrm.10308
75. Smith SM, Jenkinson M, Woolrich MW, Beckmann CF, Behrens TE, Johansen-Berg H, Bannister PR, De Luca M, Drobnjak I, Flitney DE, Niazy RK, Saunders J, Vickers J, Zhang Y, De Stefano N, Brady JM, Matthews PM (2004) Advances in functional and structural MR image analysis and implementation as FSL. *NeuroImage* 23 Suppl 1:S208-219. doi:10.1016/j.neuroimage.2004.07.051
76. Steidle G, Schick F (2006) Echoplanar diffusion tensor imaging of the lower leg musculature using eddy current nulled stimulated echo preparation. *Magnetic resonance in medicine* 55 (3):541-548. doi:10.1002/mrm.20780
77. Gudbjartsson H, Patz S (1995) The Rician distribution of noisy MRI data. *Magnetic resonance in medicine* 34 (6):910-914
78. Basser PJ (1995) Inferring microstructural features and the physiological state of tissues from diffusion-weighted images. *NMR in biomedicine* 8 (7-8):333-344
79. Roeder E, Henrionnet C, Goebel JC, Gambier N, Beuf O, Grenier D, Chen B, Vuissoz PA, Gillet P, Pinzano A (2014) Dose-response of superparamagnetic iron oxide labeling on mesenchymal stem cells chondrogenic differentiation: a multi-scale in vitro study. *PloS one* 9 (5):e98451. doi:10.1371/journal.pone.0098451
80. Karussis D, Karageorgiou C, Vaknin-Dembinsky A, Gowda-Kurkalli B, Gomori JM, Kassis I, Bulte JW, Petrou P, Ben-Hur T, Abramsky O, Slavin S (2010) Safety and immunological effects of mesenchymal stem cell transplantation in patients with multiple sclerosis and amyotrophic lateral sclerosis. *Archives of neurology* 67 (10):1187-1194. doi:10.1001/archneurol.2010.248
81. Janowski M, Walczak P, Kropiwnicki T, Jurkiewicz E, Domanska-Janik K, Bulte JW, Lukomska B, Roszkowski M (2014) Long-term MRI cell tracking after intraventricular delivery in a patient with global cerebral ischemia and prospects for magnetic navigation of stem cells within the CSF. *PloS one* 9 (2):e97631. doi:10.1371/journal.pone.0097631
82. Salamon J, Peldschus K (2014) Ultrasound-guided intracardial injection and in vivo magnetic resonance imaging of single cells in mice as a paradigm for hematogenous metastases. *Methods in molecular biology* 1070:203-211. doi:10.1007/978-1-4614-8244-4\_15
83. Amsalem Y, Mardor Y, Feinberg MS, Landa N, Miller L, Daniels D, Ocherashvilli A, Holbova R, Yosef O, Barbash IM, Leor J (2007) Iron-oxide labeling and outcome of

- transplanted mesenchymal stem cells in the infarcted myocardium. *Circulation* 116 (11 Suppl):I38-45. doi:10.1161/CIRCULATIONAHA.106.680231
84. Pintaske J, Bantleon R, Kehlbach R, Claussen CD, Wiskirchen J, Schick F (2006) Effect of concentration of SH U 555A labeled human melanoma cells on MR spin echo and gradient echo signal decay at 0.2, 1.5, and 3T. *Magma* 19 (2):71-77. doi:10.1007/s10334-006-0029-z
85. Kim YB, Bae KH, Yoo SS, Park TG, Park H (2009) Positive contrast visualization for cellular magnetic resonance imaging using susceptibility-weighted echo-time encoding. *Magnetic resonance imaging* 27 (5):601-610. doi:10.1016/j.mri.2008.10.001
86. Stuber M, Gilson WD, Schar M, Kedziorek DA, Hofmann LV, Shah S, Vonken EJ, Bulte JW, Kraitchman DL (2007) Positive contrast visualization of iron oxide-labeled stem cells using inversion-recovery with ON-resonant water suppression (IRON). *Magnetic resonance in medicine* 58 (5):1072-1077. doi:10.1002/mrm.21399
87. Dharmakumar R, Koktzoglou I, Li D (2006) Generating positive contrast from off-resonant spins with steady-state free precession magnetic resonance imaging: theory and proof-of-principle experiments. *Physics in medicine and biology* 51 (17):4201-4215. doi:10.1088/0031-9155/51/17/006
88. Seppenwoolde JH, Viergever MA, Bakker CJ (2003) Passive tracking exploiting local signal conservation: the white marker phenomenon. *Magnetic resonance in medicine* 50 (4):784-790. doi:10.1002/mrm.10574
89. Bakker CJ, Seppenwoolde JH, Vincken KL (2006) Dephased MRI. *Magnetic resonance in medicine* 55 (1):92-97. doi:10.1002/mrm.20733
90. Dahnke H, Liu W, Herzka D, Frank JA, Schaeffter T (2008) Susceptibility gradient mapping (SGM): a new postprocessing method for positive contrast generation applied to superparamagnetic iron oxide particle (SPIO)-labeled cells. *Magnetic resonance in medicine* 60 (3):595-603. doi:10.1002/mrm.21478
91. Eibofner F, Steidle G, Kehlbach R, Bantleon R, Schick F (2010) Positive contrast imaging of iron oxide nanoparticles with susceptibility-weighted imaging. *Magnetic resonance in medicine* 64 (4):1027-1038. doi:10.1002/mrm.22498
92. Morgan DM, Umek W, Guire K, Morgan HK, Garabrant A, DeLancey JO (2009) Urethral sphincter morphology and function with and without stress incontinence. *The Journal of urology* 182 (1):203-209. doi:10.1016/j.juro.2009.02.129
93. Macura KJ, Genadry RR, Bluemke DA (2006) MR imaging of the female urethra and supporting ligaments in assessment of urinary incontinence: spectrum of abnormalities. *Radiographics : a review publication of the Radiological Society of North America, Inc* 26 (4):1135-1149. doi:10.1148/rg.264055133
94. Cheong B, Muthupillai R, Rubin MF, Flamm SD (2007) Normal values for renal length and volume as measured by magnetic resonance imaging. *Clinical journal of the American Society of Nephrology : CJASN* 2 (1):38-45. doi:10.2215/CJN.00930306
95. Gonzalez Ballester MA, Zisserman AP, Brady M (2002) Estimation of the partial volume effect in MRI. *Medical image analysis* 6 (4):389-405
96. Pham D, Kron T, Foroudi F, Schneider M, Siva S (2014) A review of kidney motion under free, deep and forced-shallow breathing conditions: implications for stereotactic ablative body radiotherapy treatment. *Technology in cancer research & treatment* 13 (4):315-323. doi:10.7785/tcrt.2012.500387
97. Gadeberg P, Gundersen HJ, Taguehoj F (1999) How accurate are measurements on MRI? A study on multiple sclerosis using reliable 3D stereological methods. *Journal of magnetic resonance imaging : JMRI* 10 (1):72-79

98. Lee VS, Kaur M, Bokacheva L, Chen Q, Rusinek H, Thakur R, Moses D, Nazzaro C, Kramer EL (2007) What causes diminished corticomedullary differentiation in renal insufficiency? *Journal of magnetic resonance imaging* : JMRI 25 (4):790-795. doi:10.1002/jmri.20878
99. Roger SD, Beale AM, Cattell WR, Webb JA (1994) What is the value of measuring renal parenchymal thickness before renal biopsy? *Clinical radiology* 49 (1):45-49
100. Mounier-Vehier C, Lions C, Devos P, Jaboureck O, Willoteaux S, Carre A, Beregi JP (2002) Cortical thickness: an early morphological marker of atherosclerotic renal disease. *Kidney international* 61 (2):591-598. doi:10.1046/j.1523-1755.2002.00167.x
101. Notohamiprodjo M, Dietrich O, Horger W, Horng A, Helck AD, Herrmann KA, Reiser MF, Glaser C (2010) Diffusion tensor imaging (DTI) of the kidney at 3 tesla-feasibility, protocol evaluation and comparison to 1.5 Tesla. *Investigative radiology* 45 (5):245-254. doi:10.1097/RLI.0b013e3181d83abc
102. Chuck NC, Steidle G, Blume I, Fischer MA, Nanz D, Boss A (2013) Diffusion Tensor Imaging of the Kidneys: Influence of b-Value and Number of Encoding Directions on Image Quality and Diffusion Tensor Parameters. *Journal of clinical imaging science* 3:53. doi:10.4103/2156-7514.122323
103. Thoeny HC, De Keyzer F, Oyen RH, Peeters RR (2005) Diffusion-weighted MR imaging of kidneys in healthy volunteers and patients with parenchymal diseases: initial experience. *Radiology* 235 (3):911-917. doi:10.1148/radiol.2353040554
104. Notohamiprodjo M, Glaser C, Herrmann KA, Dietrich O, Attenberger UI, Reiser MF, Schoenberg SO, Michaely HJ (2008) Diffusion tensor imaging of the kidney with parallel imaging: initial clinical experience. *Investigative radiology* 43 (10):677-685. doi:10.1097/RLI.0b013e31817d14e6
105. Duan F, Zhao T, He Y, Shu N (2015) Test-retest reliability of diffusion measures in cerebral white matter: A multiband diffusion MRI study. *Journal of magnetic resonance imaging* : JMRI. doi:10.1002/jmri.24859
106. Feinberg DA, Setsompop K (2013) Ultra-fast MRI of the human brain with simultaneous multi-slice imaging. *Journal of magnetic resonance* 229:90-100. doi:10.1016/j.jmr.2013.02.002
107. Xu J, Moeller S, Auerbach EJ, Strupp J, Smith SM, Feinberg DA, Yacoub E, Ugurbil K (2013) Evaluation of slice accelerations using multiband echo planar imaging at 3 T. *NeuroImage* 83:991-1001. doi:10.1016/j.neuroimage.2013.07.055
108. Zijta FM, Froeling M, van der Paardt MP, Lakeman MM, Bipat S, van Swijndregt AD, Strijkers GJ, Nederveen AJ, Stoker J (2011) Feasibility of diffusion tensor imaging (DTI) with fibre tractography of the normal female pelvic floor. *European radiology* 21 (6):1243-1249. doi:10.1007/s00330-010-2044-8
109. Klünder M, Will S, Sievert K-D, Amend B, Feuer R, Sawodny O, Kramer U, Stenzl A, Ederer M (2015) Proof-of-Concept for Data Fusion of Urethral Pressure Data and MRI. *The Journal of Urology* 193 (4):e486. doi:10.1016/j.juro.2015.02.1456

## **Erklärung zum Eigenanteil**

Die Arbeit wurde am Universitätsklinikum Tübingen, Sektion für experimentelle Radiologie, unter der Betreuung von Prof. Dr. Dr. Fritz Schick durchgeführt.

Im Rahmen der Originalarbeit „*Viability and MR detectability of iron labelled mesenchymal stem cells used for endoscopic injection into the porcine urethral sphincter*“ ergab sich folgender Beitrag der Erstautorin/ Bewerberin der Promotion:

### **Will Susanne**

- Vorversuche: Schweinekadaver, externe Blase, in vitro Versuche (Zellmarkierungstest)
- Anteilige Sequenzoptimierung & Protokollerstellung
- Projektplanung: Zeitmanagement der Messungen, Transport der Tiere, Vorbereitung der Auswertetechniken
- Versuchsdurchführung: Vorbereitung und Messungen der Tiere
- Auswertungen: Visuelle Auswertung der MRT-Daten und Fusionierung mit Histologie-Daten
- Verfassung der Veröffentlichung MRT-Anteil und Erstellung der Grafiken und Abbildungen

Im Rahmen der Originalarbeit „*Automated segmentation and volumetric analysis of renal cortex, medulla, and pelvis based on non-contrast-enhanced T1- and T2-weighted MR images*“ ergab sich folgende Verteilung der Eigenleistungen der Erstautorin/Bewerberin der Promotion:

### **Will Susanne**

- Projektplanung + Studienkonzipierung
- Anteilige Sequenzoptimierung & Protokollerstellung
- Durchführung der Studie: Probandenerhebung, Aufklärung, Datenerhebung
- Erstellung und Implementierung des Segmentierungsalgorithmus
- Auswertung der Datensätze und Etablierung des Auswertealgorithmus
- Literaturrecherche
- Verfassung der Veröffentlichung und Erstellung der Grafiken und Abbildungen

Ich versichere, die Manuskripte selbständig, unter Zuhilfenahme der Beiträge der Koautoren, verfasst zu haben und keine weiteren als die von mir angegebenen Quellen verwendet zu haben.

---

*Susanne Will*

## List of Publications

**Will S**, Martirosian P, Würslin C, Schick F. *Automated segmentation and volumetric analysis of renal cortex, medulla, and pelvis based on non-contrast-enhanced T1- and T2-weighted MR images*. MAGMA. 2014;27(5):445-54. doi: 10.1007/s10334-014-0429-4.

Vaegler M, Maerz JK, Amend B, da Silva LA, Mannheim JG, Fuchs K, **Will S**, Sievert KD, Stenzl A, Hart ML, Aicher WK. *Labelling and tracking of human mesenchymal stromal cells in preclinical studies and large animal models of degenerative diseases*. Curr Stem Cell Res Ther. 2014;9(5):444-50.

Amend B, Vaegler M, Fuchs K, Mannheim JG, **Will S**, Kramer U, Hart ML, Feitz W, Chapple C, Stenzl A, Aicher WK. *Regeneration of Degenerated Urinary Sphincter Muscles: Improved Stem Cell-based Therapies and Novel Imaging Technologies*. Cell Transplant. 2015; 24(11):2171-83. doi: 10.3727/096368915X686229.

**Will S**, Martirosian P, Eibofner F, Schick F, Bantleon R, Vaegler M, Grözinger G, Claussen CD, Kramer U, Schmehl J. *Viability and MR detectability of iron labeled mesenchymal stem cells used for endoscopic injection into the porcine urethral sphincter*. NMR Biomed. 2015;28(8):1049-58. doi: 10.1002/nbm.3339.

## Conference Contribution

**Will S**, Martirosian P, Würslin C, Schick F. *Semi-automated renal segmentation in-vivo based on non contrast-enhanced T1 and T2 weighted images to separate renal cortex, medulla, and pelvis* (568). 29<sup>th</sup> Annual Meeting of ESMRMB, Lissabon, Portugal, 2012.

**Will S**, Martirosian P, Würslin C, Schick F. *In-vivo volumetry of the entire kidneys and their internal structures using non contrast-enhanced MR images: Comparison of automated and manual segmentation*". 30<sup>th</sup> Annual Meeting of ESMRMB, Toulouse, France, 2013.

**Will S**, Martirosian P, Fuchs K, Mannheim J.G, Schmehl J, Grözinger G, Bantleon R, Vaegler M, **Sievert K-D**, Schick F, Claussen CD, Pichler BJ, Kramer U. *Establishment of in vivo small animal models to determine cell mobility and viability and imaging of injected mesenchymal stem cells in the pig sphincter*. The Journal of Urology, Volume 191, Issue 4, Supplement, 2014, e68.

**Will S**, Martirosian P, Schraml C, Kardatzki B, Erb M, Steidle G, Schick F. *Correction of susceptibility induced distortions in native EPI MR images in healthy human kidneys*. ISMRM, Milan, Spain, 2014.

**Martirosian P**, Erb M, **Will S**, Schick F, Gatidis S, Schmidt H, Schwenzer N.F, Schraml C. *Multiband-Accelerated Diffusion-Weighted MR Imaging of the Abdominal Organs: Initial Experiences (2269)*. ISMRM, Milan, Spain, 2014.

Schraml C, **Will S**, Schwenzer NF, Steidle G, Claussen CD, Schick F, **Martirosian P**. *Assessment of inner volume imaging technique for renal tissue characterization by IVIM and DTI at 3 T*. ISMRM, Milan, Spain, 2014.

**Will S**, Martirosian P, Eibofner F, Schmehl J, Grözinger G, Bantleon R, Vaegler M, Sievert K-D, Schick F, Nikolaou K, Kramer U. *Assessment of iron labeled mesenchymal stem cells for endoscopic injection into the porcine urethral sphincter using MRI*. European Urology Supplements, Volume 14, Issue 2, 2015, e1008-e1008a.

**Klunder M**, **Will S**, Amend B, Vaegler M, Sawodny O, Feuer R, Kramer U, Stenzl A, Sievert K-D, Ederer M. *Proof-of-Concept for Data Fusion of MRI and Urethral Pressure Data*. European Urology Supplements, Volume 14 Issue 2, 2015, e386-e386a.

**Will S**, **Sievert K-D**, Vaegler M, Eibofner F, Martirosian P, Schick F, Schmehl J, Grözinger G, Bantleon R, Nikolaou K, Kramer U. *Magnetic resonance visibility of iron labeled mesenchymal stem cells for endoscopic injection into the porcine urethral sphincter*. The Journal of Urology. 2015. Vol. 193, Issue 4, e126–e127.

**Klunder M**, **Will S**, Sievert K-D, Amend B, Feuer R, Sawodny O, Kramer U, Stenzl A, Ederer M. *Proof-of-Concept for Data Fusion of Urethral Pressure Data and MRI*. The Journal of Urology. 2015. Vol. 193, Issue 4, e486.

**Will S**, Martirosian P, Kardatzki B, Steidle G, Schick F. *Time-saved and accurate diffusion tensor imaging of renal structures using multiband technique*. 31<sup>th</sup> Annual Meeting of ESMRMB, Edinburgh, Scotland, 2015.

## **Danksagung**

Diese Arbeit wurde im Zeitraum von 2012 bis 2016 an der Eberhard-Karls-Universität Tübingen in der Abteilung für experimentelle Radiologie durchgeführt. Zuerst möchte ich mich bei meinem betreuenden Professor Prof. Dr. med. Dr. rer. nat. Fritz Schick bedanken, dass er mir die Möglichkeit gegeben hat, diese Dissertation anzufertigen.

Die Betreuung dieser Arbeit erfolgte durch Herrn Dr. sc hum Petros Martirosian. Ihm gilt mein besonderer Dank, da er mir immer mit Rat und Tat zur Seite stand. Für seine Hilfe bin ich ihm dankbar und werde die zahlreichen Diskussionen nie vergessen.

Sehr dankbar bin ich den eifrigen Korrekturlesern dieser Arbeit, die viel Zeit und Arbeit in die Verbesserung gesteckt haben.

Für die hilfreiche Unterstützung bei der Erstellung des Segmentierungsalgorithmus möchte ich mich bei Christian Würslin herzlich bedanken. Für weitere Hilfestellungen bei der Behebung von MatLab-Problemen möchte ich mich bei Thomas Küstner, Martin Schwartz und Michael Erb bedanken.

Mein Dank gilt ebenfalls allen Mitglieder der Sektion Petros Martirosian, Frank Eibofner, Hansjörg Graf, Jürgen Machann, Günter Steidle, Karin Waneck, Thomas Küstner, Martin Schwartz, Andreas Zimmermann, Holger Schmidt, Tina Schraml, Nina Schwenzer, Christoph Schabel, Gerd Grözinger und Roland Syha. Ein weiterer Dank gilt auch den jeweiligen guten Seelen des Hauses Michaela Singer und Karin Werz.

Herzlich bedanken möchte ich mich für die sehr gute Zusammenarbeit während der KFO273 bei Mario Klünder, Ulrich Kramer, Alexandra Kelp und Martin Vaegler.

Zu guter Letzt gilt mein Dank von ganzen Herzen meiner wunderbaren Familie, besonders meiner Mutter Franziska und meinem Ehemann Steffen, die mich während der gesamten Durchführung und Verfassung dieser Arbeit in all den Monaten/Jahren unterstützt haben.